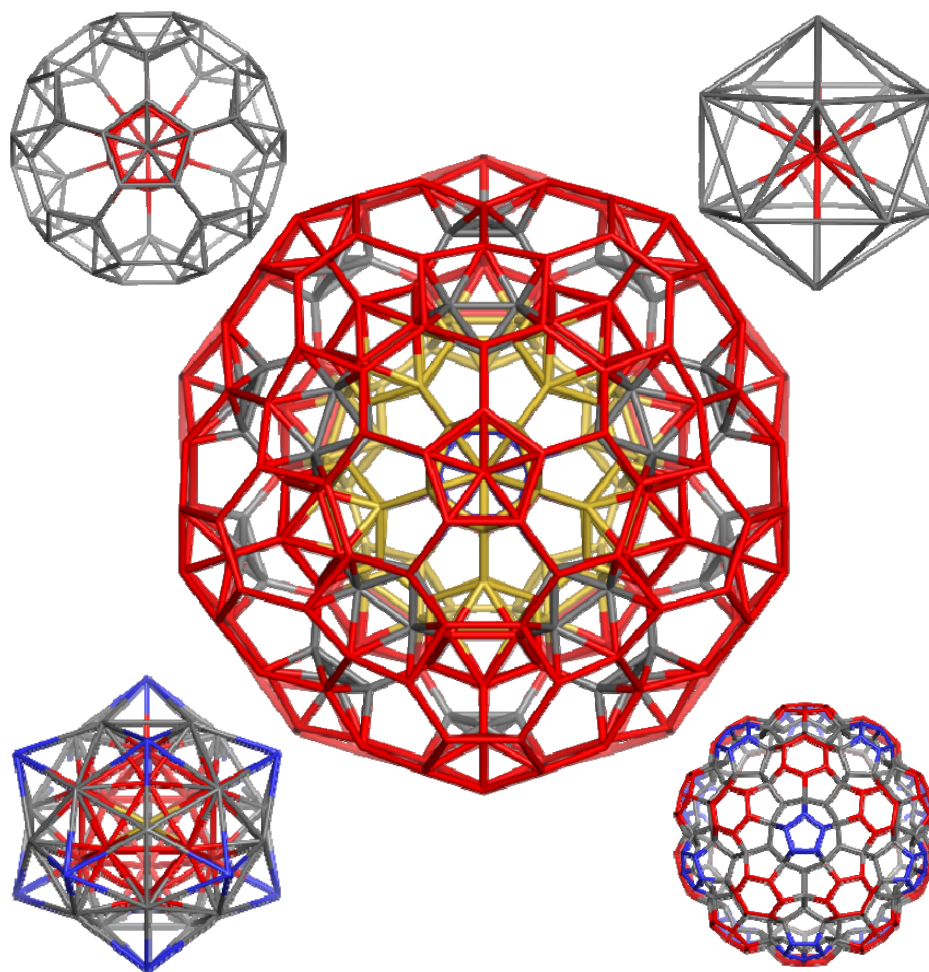




STUDIA UNIVERSITATIS  
BABEŞ-BOLYAI



# CHEMIA

---

3/2014

**STUDIA  
UNIVERSITATIS BABEȘ-BOLYAI  
CHEMIA**

**3/2014**

**EDITORIAL BOARD**  
**STUDIA UNIVERSITATIS BABEȘ-BOLYAI**  
**CHEMIA**

**ONORARY EDITOR:**

IONEL HAIDUC - Member of the Romanian Academy

**EDITOR-IN-CHIEF:**

LUMINIȚA SILAGHI-DUMITRESCU

**EXECUTIVE EDITOR:**

CASTELIA CRISTEA

**EDITORIAL BOARD:**

PAUL ȘERBAN AGACHI, Babeș-Bolyai University, Cluj-Napoca, Romania

LIVAIN BREAU, UQAM University of Quebec, Montreal, Canada

HANS JOACHIM BREUNIG, Institute of Inorganic and Physical Chemistry,  
University of Bremen, Bremen, Germany

MIRCEA DIUDEA, Babes-Bolyai University, Cluj-Napoca, Romania

JEAN ESCUDIE, HFA, Paul Sabatier University, Toulouse, France

ION GROSU, Babeș-Bolyai University, Cluj-Napoca, Romania

EVAMARIE HEY-HAWKINS, University of Leipzig, Leipzig, Germany

FLORIN DAN IRIMIE, Babeș-Bolyai University, Cluj-Napoca, Romania

FERENC KILAR, University of Pecs, Pecs, Hungary

BRUCE KING, University of Georgia, Athens, Georgia, USA

ANTONIO LAGUNA, Department of Inorganic Chemistry, ICMA, University of  
Zaragoza, Zaragoza, Spain

JURGEN LIEBSCHER, Humboldt University, Berlin, Germany

KIERAN MOLLOY, University of Bath, Bath, UK

IONEL CĂTĂLIN POPESCU, Babeș-Bolyai University, Cluj-Napoca, Romania

CRISTIAN SILVESTRU, Babeș-Bolyai University, Cluj-Napoca, Romania

<http://chem.ubbcluj.ro/~studiachemia/>; [studiachemia@chem.ubbcluj.ro](mailto:studiachemia@chem.ubbcluj.ro)  
[http://www.studia.ubbcluj.ro/serii/chemia/index\\_en.html](http://www.studia.ubbcluj.ro/serii/chemia/index_en.html)

**YEAR**  
**MONTH**  
**ISSUE**

**Volume 59 (LIX) 2014**  
**SEPTEMBER**  
**3**

**S T U D I A**  
**UNIVERSITATIS BABEŞ-BOLYAI**  
**CHEMIA**

**3**

---

**STUDIA UBB EDITORIAL OFFICE:** B.P. Hasdeu no. 51, 400371 Cluj-Napoca, Romania,  
Phone + 40 264 405352

---

**CUPRINS – CONTENT – SOMMAIRE – INHALT**

SLAĐANA MEDIĆ-PAP, STEVAN MAŠIREVIĆ, DEJAN PRVULOVIĆ, Phenolic Compounds and Antioxidant Activity of Sunflower Hybrids Inoculated with Broomrape.....	7
ANCA ŐIPOŐ, ÁRPÁD IMRE-LUCACI, Statistical Processing and Dynamic Modeling of an Alcoholic Fermentation Process.....	17
MIRELA MURESAN, CALIN-CRISTIAN CORMOS, PAUL-SERBAN AGACHI, Biomass Gasification – Based Hydrogen Production Supply Chain Analysis under Demand Variability .....	29
MIRELA MICLEAN, LĂCRIMIOARA ŐENILĂ, OANA CADAR, MARIUS ROMAN, ERIKA LEVEI, CLAUDIU TĂNĂSELIA, ANNAMĂRIA TÖRÖK, CORNELIA MAJDIK, Determination of Chlorpyrifos in Surface Water using SPE-DI-SPME/GC-ECD.....	43
SHAHRAM NEKOUEI, FARZIN NEKOUEI, Application of Multiwalled Carbon Nanotubes Modified by Diethyl Dithiophosphate Ammonium for Selective Solid Phase Extraction of Ultra Traces Ni(II) and Co(II) in River Water Samples .....	49

EHAB ALSHAMAILEH, MOHAMMAD H. KAILANI, SHARIF ARAR, AIMAN E. AL-RAWAJFEH, Corrosion Inhibition of Aluminium by Cyclohexylamine Dithiocarbamate in Acidic Solution .....	61
MARIA DANIELA STELESCU, Studies on Obtaining Ionic Thermoplastic Elastomers Based on Maleinized Styrene-Butadiene Block- Copolymers .....	71
M. SAKI, A. IRANMANESH O. KHORMALI, Edge Geometric-Arithmetic Index of Some Graphs.....	83
JULIETA DANIELA CHELARU, LIANA MARIA MURESAN, 2-Mercapto-5- Acetylamino-1,3,4-Thiadiazole as Corrosion Inhibitor for a Naturally Patinated Monumental Bronze Artifact .....	91
ATENA PARVAN-MOLDOVAN, FATEMEH KOOREPAZAN-MOFTAKHAR, MIRCEA V. DIUDEA, Topological Symmetry of Multi-Shell Icosahedral Clusters.....	103
ALPARSLAN KADİR DEVRİM, ALİ ARSLANTAS, MERT SUDAGIDAN, DURSUN ALİ KÖSE, BİRGÜL KARAN, Investigation of DNA Binding and Cleavage Activities of Boron Complexes in the Presence of Hydrogen Peroxide.....	109
MIHAELA ALEXANDRA POP, TUDOR CATALIN DRUGAN, ADRIANA GROZAV, BIANCA DOMOKOS, ANDRADA URDA, CARMEN MONICA POP, C Reactive Protein Level as a Diagnose Test for Sleep Apnea-Hypopnea Syndrome.....	119
MODJTABA GHORBANI, Some New Results on the Nullity of Molecular Graphs.....	127
BARBU-RADU-HORATIU MISCA, DORIN-IOSIF MANCIULA, An Inter- pretation of Solid-Liquid Extraction Using the General Dimensional Method.....	139

Studia Universitatis Babes-Bolyai Chemia has been selected for coverage in Thomson Reuters products and custom information services. Beginning with V. 53 (1) 2008, this publication is indexed and abstracted in the following:

- Science Citation Index Expanded (also known as SciSearch®)
- Chemistry Citation Index®
- Journal Citation Reports/Science Edition



## PHENOLIC COMPOUNDS AND ANTIOXIDANT ACTIVITY OF SUNFLOWER HYBRIDS INOCULATED WITH BROOMRAPE

SLAĐANA MEDIĆ-PAP<sup>a\*</sup>, STEVAN MAŠIREVIĆ<sup>b</sup>,  
DEJAN PRVULOVIĆ<sup>b</sup>

**ABSTRACT.** Phenolic compounds such as polyphenols, tannins and flavonoids as well as antioxidant activity, play an important role in the plant defense mechanisms. The above mentioned parameters were measured in four sunflower hybrids (NORH-34, HOB-2, IMI-3-911 and NS-H-111) inoculated with broomrape (sunflower root parasitic plant). The synthesis and accumulation of these compounds depended on genotype and broomrape inoculation. Total phenolic content in healthy sunflower root tissue ranged from 2.87 up to 10.53 mg, while in infected root tissue this parameter ranged from 6.06 to 12.66 mg gallic acid equivalents/g dry root weight. Total tannins content in healthy root ranged from 2.01 to 6.74 and in infected root from 4.30 to 8.17 mg gallic acid equivalents/g dry root weight. Total flavonoids in healthy root tissue were within the range 3.36-44.94 and in infected root tissue 35.35-83.89 mg of rutin equivalents/g dry root weight. Antioxidant activity in sunflower roots correlated with the total phenolic and total tannins and flavonoids content.

**Keywords:** *broomrape, sunflower, polyphenol compounds, antioxidant activity*

### INTRODUCTION

Plants encounter parasitic attacks by pathogenic microorganisms, herbivores and insects. Parasites have developed different strategies for colonizing plants, since they need regulation mechanisms to effectively adapt to changes in their environment. Plants have developed effective defense mechanisms against pathogenic infections. Following penetration by pathogens induced structural and chemical barriers are activated in order to prevent the pathogen's progression [1]. Under the stress conditions plants produce higher content of reactive oxygen species (hydroxyl and superoxide radicals). Plant

---

<sup>a</sup> *Institute of Field and Vegetable Crops, Maksima Gorkog 30, Novi Sad, Serbia*

\* *Corresponding author: sladjana.medicpap@nsseme.com*

<sup>b</sup> *University of Novi Sad, Faculty of Agriculture, Trg Dositeja Obradovica 8, Serbia*

defense mechanism includes activation of enzymatic and non-enzymatic system. Enzymatic mechanism is activation of different enzymes such as catalase, superoxide dismutase and different types of peroxidases. Non-enzymatic defense system includes higher synthesis of some biomolecules such as glutathione, vitamins C and E, and other scavengers of free radicals [2].

Plant phenolics are secondary metabolites that encompass several structurally diverse classes of natural products. The phenolic composition varies considerably both qualitatively and quantitatively between species and between individuals of the same species. Secondary metabolites have specific significance in plants ecology and their adaptation to different biotic and abiotic factors. Phenolic compounds involved in plant defense are either constitutive or synthesized *de novo* (postinfectious). Phenolic compounds synthesized *de novo* accumulate in response to plant infection by a pathogen [3]. These compounds have significant scavenging activity of reactive oxygen species [4].

Broomrapes (*Orobancha* spp.) belong to the family of obligate parasitic flowering plants-*Orobanchaceae*. Broomrapes are native primarily to the Mediterranean region (i.e. North Africa, the Middle East, and southern Europe), and western Asia [5]. With anticipated climatic changes *Orobancha* species could pose greater threats to agriculture by expanding their ranges farther north in Europe [6]. *O. cumana* (Wallr.) is the cause of many economic losses in sunflower production on a worldwide scale [7]. In addition to this pest's huge infectious potential, another great problem is caused by the heterogeneity of its population i.e. by the existence of multiple physiological races.

Definition of phenolic compounds defense role and the control of their synthesis could be important in the crop protection primarily through breeding programs [8]. Several authors indicated the involvement of lignification and cell wall phenolics deposition in the sunflower tissue as a defense response to broomrape penetration [9, 10, 11]. Resistant or tolerant sunflower hybrids are the most efficient way of suppression of this parasitic plant [7].

The objectives of the present study were to investigate the content of phenolic compounds and antioxidant response in root tissue of different sunflower hybrids infected by broomrape.

## RESULTS AND DISCUSSION

The evaluation of broomrape attack on sunflower plants was done in the period of full flowering (Table 1). The highest attack was observed on hybrid NS-H-111 and on high-oleic hybrid HOB-2. Other two hybrids IMI-3-911 and NORH-34 had lower attack, below 10 broomrape plants per sunflower plant. These data showed the differences between hybrids in the resistance

to broomrape in the conditions of field infection. The reaction of the tested hybrids was expected and similar to the results obtained in our previous investigations [12].

**Table 1.** Broomrape attack on sunflower plants

Hybrid	Number of broomrape plants per sunflower plant
NORH-34	8
HOB-2	27
IMI-3-911	7
NS-H-111	29

The content of total phenolics (TP) and total tannins (TT) in the root of four tested sunflower hybrids in the period of full flowering are given in the Table 2. Sunflower hybrid, broomrape attack and interaction of these factors had effect on production of TP and TT in root. TP and TT contents were highest in hybrid NORH-34 (12.66 and 8.15 mg gallic acid equivalents (GAE)/g dry weight (DW) respectively). Production of these compounds in NORH-34 was approximately four times higher in infected sunflower roots at the contact point with broomrape (CP) than in healthy sunflower roots (HSR). Besides the resistance based on physical barriers; resistance could be based on the chemical response such as the production and secretion of the toxic phenolic compounds [13]. Resistant vetch defense mechanism involves elevated induction of the phenyl propanoid pathway upon *Orobanche* infection, conferring mechanical and chemical barriers confronting the invading parasite [14]. Reaction in the sunflower-broomrape pathosystem is in the correlation with increasing of phenolic level, peroxidase activity [15] and accumulation of substances on the inner part of host-plant xylem vessels [16]. Sunflower roots after the treatment with 1,2,3-benzothiadiazole-7-carbothioic acid S-methyl-ester (BTH) resistance-inducing agents (had higher bound phenolic content in cell walls and that might indicated that the plant formed structural barriers as defense to broomrape [17]. Accumulation of phenolic compounds could help in order to test resistance to broomrape in different selection phase [18]. Coumarins such as scopoletin, scopolin and ajapin (phenolic compounds) in sunflower inhibit germination and attaching of broomrape [19]. Hybrid IMI-3-911 also had high synthesis of TP and TT (11.74 and 8.17mg GAE/g DW respectively) and lower level of infestation. However there is no significant difference in this hybrid in content of TP and TT related to infection. In root of hybrids NS-H-111 and HBO-2 content of TP and TT was significantly lower in comparison to NORH-34 and IMI-3-911. However significant differences in the content of TP, in NS-H-111 and HBO-2

between HSR and CP indicate that these hybrids responded to infection by synthesis of phenolic compounds, but it was not enough to suppress the high intensity of broomrape attack in the period of full flowering. Production of secondary metabolites is caused by stress and they are produced in damaged tissue [20].

**Table 2.** Total polyphenols and tannins content in different sunflower hybrids

Hybrid	Infection	Total polyphenols <sup>1</sup>	Total tannins <sup>1</sup>
NORH-34	CP	12.66 ± 0.23 <sup>a</sup>	8.15 ± 0.05 <sup>a</sup>
	INF+	4.59 ± 0.18 <sup>g</sup>	2.89 ± 0.59 <sup>de</sup>
	HSR	2.87 ± 0.18 <sup>i</sup>	2.01 ± 0.25 <sup>e</sup>
HOB-2	CP	7.25 ± 0.22 <sup>d</sup>	5.38 ± 0.06 <sup>bc</sup>
	INF+	6.80 ± 0.18 <sup>de</sup>	5.22 ± 0.20 <sup>bc</sup>
	HSR	6.54 ± 0.25 <sup>ef</sup>	4.95 ± 0.09 <sup>c</sup>
IMI-3-911	CP	11.74 ± 0.21 <sup>b</sup>	8.17 ± 0.18 <sup>a</sup>
	INF+	10.66 ± 0.49 <sup>c</sup>	7.33 ± 0.04 <sup>a</sup>
	HSR	10.53 ± 0.09 <sup>c</sup>	6.74 ± 1.71 <sup>ab</sup>
NS-H-111	CP	6.06 ± 0.20 <sup>f</sup>	4.30 ± 0.04 <sup>cd</sup>
	INF+	6.16 ± 0.13 <sup>ef</sup>	4.14 ± 0.09 <sup>cd</sup>
	HSR	3.93 ± 0.09 <sup>h</sup>	2.94 ± 0.13 <sup>de</sup>
p		Hybrid 0,00** Infection 0,00** Infection x Hybrid 0,00**	Hybrid 0,00** Infection 0,00** Infection x Hybrid 0,00**
Data are mean ± SE values <sup>1</sup> Expressed as mg of gallic acid equivalents/g of dry root. <sup>a-i</sup> the values without the same superscript within each column differ significantly ( $p < 0.05$ ). ** - significant at probability level ( $p < 0.01$ ). CP - at the contact point of broomrape tubercle and sunflower root. INF+ - outside of contact point from the parasite and host plant. HSR - healthy sunflower roots.			

There are strong evidences for a role of flavonoids in plant resistance and their induced formation after injury by pathogens or pests [21]. Total flavonoids content (TF) in sunflower root was influenced by hybrid, intensity of infection and interaction of these two factors. The highest TF content had been measured in hybrid IMI-3-911 at CP and it was about two times higher than in HSR as well as in hybrid NS-H-111. Hybrid NORH-34 had 20 times higher TF content in attacked roots than in healthy ones. Accumulation of phenolic compounds, such as flavonoids, in the sunflower-broomrape resistance

mechanisms is well-known phenomenon [22, 23]. Recent investigations also showed increased levels of phenolics and flavonoids in the broomrape infected tomato roots [24]. Level of flavonoids and tannins and DPPH values was relatively high in high-oleic hybrid HOB-2 compared to other tested hybrids, but there are no significant differences between healthy and infected tissues (Table 3). According to these results it could be concluded that the broomrape infection did not trigger the synthesis of TT, TF and antioxidant activity in the root of HOB-2. However antioxidant activity in HOB-2 had the highest value in healthy root tissue. High values of these compounds in healthy tissue could be explained by genetic characteristics of this hybrid.

**Table 3.** Total flavonoids content and DPPH-values in different sunflower hybrids

Hybrid	Infection	Total flavonoids <sup>1</sup>	DPPH-values
NORH-34	CP	68.67 ± 2.34 <sup>b</sup>	63.40 ± 1.58 <sup>a</sup>
	INF+	27.32 ± 0.75 <sup>e</sup>	30.44 ± 0.97 <sup>d</sup>
	HSR	3.36 ± 0.48 <sup>g</sup>	17.14 ± 1.75 <sup>f</sup>
HOB-2	CP	35.35 ± 1.02 <sup>d</sup>	53.61 ± 0.41 <sup>b</sup>
	INF+	32.84 ± 0.31 <sup>d</sup>	52.54 ± 3.10 <sup>bc</sup>
	HSR	33.91 ± 0.78 <sup>d</sup>	62.74 ± 0.26 <sup>a</sup>
IMI-3-911	CP	83.89 ± 2.29 <sup>a</sup>	66.25 ± 0.71 <sup>a</sup>
	INF+	64.47 ± 1.86 <sup>b</sup>	65.43 ± 0.82 <sup>a</sup>
	HSR	44.94 ± 0.75 <sup>c</sup>	67.57 ± 0.66 <sup>a</sup>
NS-H-111	CP	41.58 ± 1.02 <sup>c</sup>	50.81 ± 1.02 <sup>bc</sup>
	INF+	32.48 ± 2.67 <sup>d</sup>	47.62 ± 1.50 <sup>c</sup>
	HSR	19.89 ± 0.67 <sup>f</sup>	24.58 ± 0.94 <sup>e</sup>
p		Hybrid 0,00** Infection 0,00** Infection x Hybrid 0,00**	Hybrid 0,00** Infection 0,00** Infection x Hybrid 0,00**
Data are mean ± SE values <sup>1</sup> Expressed as mg of rutin/g of dry plant material. <sup>2</sup> Expressed as % neutralized free DPPH radicals. a-g the values without the same superscript within each column differ significantly ( $p < 0.05$ ). **- significant at probability level ( $p < 0.01$ ). CP - at the contact point of broomrape tubercle and sunflower root. INF+ - outside of contact point from the parasite and host plant. HSR - healthy sunflower roots.			

DPPH values showed the differences between hybrids and level of infection. The  $IC_{50}$  DPPH-values for tested extracts varied from 17.14 to 67.57. The highest differences in this parameter between infected and healthy root were noticed in NORH-34. Antioxidant activity was also high in IMI-3-911, but with no significant difference depending on intensity of infection (Table 3).

Beside the antioxidant enzymes in the plants there are defense systems which are involved in eliminating of reactive oxygen species (ROS) or prevention of their production. ROS plays an important role in plant response to pathogen attack, but they are also extremely reactive. Production and accumulation of ROS at the point of infection has an important role in sunflower and broomrape relation [25, 26]. The correlation between the content of all phenolic compounds and DPPH activity was significant in NORH-34 and in NS-H-111 (Table 4). These results indicate that increase of all measured phenolic compounds leads to enhancement of antioxidant activity in roots. Higher level of antioxidant activity indicates that sunflower plants were defending from the broomrape attack by biosynthesis of phenolic compounds. The hybrid NORH-34 belongs to the group of resistant hybrids, while NS-H-111 is known as one of the widespread hybrids in the agroecological conditions of Serbia and Southeastern Europe.

**Table 4.** Correlation between DPPH-assay and investigated phenolic compounds in sunflower roots

	Correlation coefficient (r)			Coefficient of determination ( $r^2$ )		
	TP	TT	TF	TP	TT	TF
DPPH						
NORH-34	0.98*	0.96*	0.98*	0.97*	0.92*	0.97*
HOB-2	-0.61	-0.82*	0.10	0.37	0.68	0.01
IMI-3-911	-0.27	0.12	-0.34	0.07	0.01	0.11
NS-H-111	0.94*	0.97*	0.91	0.88*	0.94*	0.83*

\* Values marked with astray are statistically significant ( $p>0.05$ )

## CONCLUSION

To conclude, this investigation showed variability between sunflower genotypes in measured chemical attributes in the healthy as well as in the broomrape infected tissue. Significantly higher production of polyphenols, tannins and flavonoids and antioxidant activity was observed in roots of hybrid NORH-34 at the contact point between host plant and broomrape, compared to the healthy roots. Hybrid IMI-3-911 showed also high levels of the measured compounds apart from inoculation. These two hybrids had the lowest level of

broomrape infection in the flowering period. In other tested hybrids there were no significant changes in measured parameters related to the infestation of broomrape.

Results of this study showed that the content of TP, TT, TF and DPPH value could be used as additional parameters in the evaluation of sunflower resistance to broomrape. However, genotypes with significantly higher production of TP, TT, TF and DPPH activity should be further evaluated in the inoculation tests.

## EXPERIMENTAL SECTION

### *Plant material (Sunflower plants)*

Resistance of sunflower hybrids to broomrape in the conditions of artificial infection was evaluated in the field trial in Svetozar Miletic locality (Northern part of Serbia). Broomrape seeds were put in seedbed together with sunflower seeds during the sowing. Four sunflower hybrids from different groups: resistant to broomrape NORH-34; high-oleic HOB-2; resistant to imidazolinone herbicides IMI-3-911 and standard hybrid NS-H-111 were included in the study of biochemical parameters. Four plants of the each hybrid were inoculated in three replicates.

The first broomrape attack on sunflower plants was observed in the full flowering. Infested sunflower plants were uprooted and taken to the laboratory where their roots were washed and the number of broomrape plants was counted.

Two types of sunflower root tissue samples were taken from the infected roots: 1. at the contact point of broomrape tubercle and sunflower root (CP); 2. outside of contact point from the parasite and host plant (INF+). Healthy sunflower roots (HSR) of the same hybrids were used as a control. Sunflower roots were dried in dark place at room-temperature to the constant weight.

### *Extraction and determination of total polyphenols, and tannins*

Plant material (200 mg) was extracted with 70% aqueous acetone solution (50 mL) by sonication for 20 minutes in an ultrasonic bath at ambient temperature. The extracts were rapidly vacuum-filtered through a sintered glass funnel and kept refrigerated before assay. All extractions were done in triplicate.

Total polyphenols in the acetone extracts were determined colorimetrically (Jenway 6505, UK) at 720 nm using Folin-Ciocalteu reagent [27]. Gallic acid (GAE) was used as a standard (covering the concentration range between 0.1 and 1.0 mg/mL) and results were expressed as milligrams of GAE per gram of dry root (DW).

Total tannins content was determined by the Folin-Ciocalteu procedure, after removal of tannins by their adsorption on insoluble matrix (polyvinylpyrrolidone) [28]. Calculated values were subtracted from total polyphenol contents, and total tannin contents were expressed as milligrams of GAE per gram of DW.

#### *Extraction and determination of flavonoids*

Total flavonoids were determined after extraction of 1 g of dry plant material with 20 mL of extracting solvent methanol water-acetic acid (140:50:10 by volume), for 60 minutes, according to the procedure of [29]. The amount of flavonoids was calculated as a rutin equivalent from the calibration curve of rutin standard solutions and expressed as milligrams of rutin per gram of DW.

#### *Measurement of antioxidant activity*

The potential antioxidant activity of the test samples have been assessed based on scavenging activity of the 10% aqueous acetone sunflower root extracts of the stable DPPH free radicals [30]. DPPH-radical scavenging activity was expressed as percentage of neutralized free radicals, assuming that the sample with the higher percentage has higher scavenging capacity. All measurements were done in triplicate.

#### *Statistical analysis*

Results were expressed as mean of determinations of three independent samples made in triplicates. Statistical significance was tested by analysis of variance followed by comparison of means by Duncan's multiple range test ( $P < 0.05$ ) calculated using STATISTICA (StatSoft, 9.0). Stepwise multiple regression analyses were used to determine correlation among variables.

## **ACKNOWLEDGMENT**

This paper was realized as a part of the project "Studying climate change and its influence on the environment: impacts, adaptation and mitigation" (43007) financed by the Ministry of Education and Science of the Republic of Serbia within the framework of integrated and interdisciplinary research for the period 2011-2014.

## REFERENCES

- [1]. V. Lattanzio, V.M.T. Lattanzio, A. Cardinali, "Role of phenolics in the resistance mechanisms of plants against fungal pathogens and insects", *Phytochemistry, Advances in Research*, India, **2006**, 23.
- [2]. M. Mazid, T.A. Khan, F. Mohammad, *Biology and Medicine*, **2011**, 3, 232.
- [3]. C.A. Ewané, P. Lepoivre, L.L. de Bellaire, L. Lassois, *Biotechnology, Agronomy, Society and Environment*, **2012**, 16, 393.
- [4]. J. Witzell, J.A. Martín, *Canadian Journal of Forest Research*, **2008**, 38, 2711.
- [5]. C. Parker, C.R. Riches, "Parasitic Weeds of the World: Biology and Control", Wallingford, UK: CAB International **1993**, 332.
- [6]. K.I. Mohamed, M. Papes, R. Williams, B.W. Benz, A.T. Peterson, *A Journal of the Human Environment*, **2006**, 35, 281.
- [7]. D. Škorić, G. Seiler, Z. Liu, Ch. Jan, J. Miller, C. Laurence, "Sunflower genetics and breeding", Serbian Academy of Sciences and Arts, Branch in Novi Sad, **2012**, 520.
- [8]. J. Jorrín, K. Serghini, A. Pérez de Luque, F.A. Macías, J.C. García Galindo, L. García-Torres, M. Castejón-Muñoz, "Current problems of *Orobanche* research", The 4<sup>th</sup> *International Workshop on Orobanche*, Albena, **1999**, 43.
- [9]. T.S. Antonova, "Biochemical aspects of the development of new virulent forms in the Moldavian population (race C) of *Orobanche cumana* Wallr. against the background of resistant sunflower cultivars", The 3<sup>rd</sup> *International Workshop on Orobanche and Related Striga Research*, Amsterdam, **1994**, 290.
- [10]. N. Ish-Shalom-Gordon, R. Jacobsohn, Y. Cohen, "Several fluctuations in sunflower's resistance to *Orobanche cumana*", The 3<sup>rd</sup> *International Workshop on Orobanche and Related Striga Research*, Amsterdam, **1994**, 351.
- [11]. J. Jorin, E. De Ruck, K. Serghini, A. Perez de Luque, J. Munoz-Garcia. J. Cubero, D. Berner, D. Joel, L. Mussleman, C. Parker, "Biochemical aspects of the parasitism of sunflower by *Orobanche*", *The 6<sup>th</sup> International Parasitic Weed Symposium*, Cordoba, **1996**, 551.
- [12]. S. Maširević, S. Medić-Pap, D. Škorić, D. Živanov, "Susceptibility of some experimental sunflower hybrids to white rot (*Sclerotinia sclerotiorum*) and broomrape (*Orobanche cumana*)", *The 22<sup>nd</sup> International Symposium "Food safety and production"*, Trebinje, **2011**, 318.
- [13]. S. Echevarría-Zomeño, A. Pérez-de-Luque, J. Jorrín, A.M. Maldonado, *Journal of Experimental Botany*, **2006**, 57, 4189.
- [14]. Y. Goldwasser, J. Hershenhorn, D. Plakhine, Y. Kleifeld, B. Rubin, *Physiological and Molecular Plant Pathology*, **1999**, 54, 87.
- [15]. T.S. Antonova, S.J. Ter Borg, *Weed Research*, **1996**, 36, 113.
- [16]. I. Dörr, A. Staack, R. Kollmann, "Resistance of *Helianthus* to *Orobanche*-histological and cytological studies", *The 3rd International Workshop on Orobanche and Related Striga Research*, Amsterdam, **1994**, 276.
- [17]. Z.W. Fan, H. Buschmann, J. Sauerborn, *Deutscher Tropentag*, **2003**, 1.

- [18]. A. Pérez-de-Luque, M.T. Moreno, D. Rubiales, *Annals of Applied Biology*, **2008**, 152, 131.
- [19]. K. Serghini, A. Pérez de Luque, M. Castejón–Muñoz, L. García–Torres, J. Jorrín, *Journal of Experimental Botany*, **2001**, 52, 2227.
- [20]. J. Jorrín, E. Prats, "Recent advances on allelopathy", *A science for the future*, Cádiz: **1999**, 179.
- [21]. D. Treutter Significance of flavonoids in plant resistance: a review, *Environmental Chemistry Letters*, **2006**, 4, 147.
- [22]. M. Jacobs, P.H. Rubery, *Science*, **1988**, 241, 346.
- [23]. P. Labrousse, M.C. Arnaud, H. Serieys, A. Bervillé, P. Thalouarn, *Annals of Botany*, **2001**, 88, 859.
- [24]. S. Al-Wakeel, H. Moubasher, M. Gabr, Maday, M. *IUFS Journal of Biology*, **2013**, 72, 137.
- [25]. A. Pérez-de-Luque, C.I. González-Verdejo, M.D. Lozano, M.A Dita, J.I. Cubero, P. González-Melendi, M.C. Risueño, D. Rubiales, *Journal of Experimental Botany*, **2006**, 57, 1461.
- [26]. J. Sauerborn, H. Buschmann, K. Ghiasvand Ghiasi, K.H. Kogel, *Phytopathology*, **2002**, 92, 59.
- [27]. G.T. Kroyer, *Inovative Food Science and Emerging Technologies*, **2004**, 5, 101.
- [28]. A. Hagermann, I. Harvey-Mueller, H.P.S. Makkar, Quantification of Tannins in Tree Foliage – A Laboratory Manual FAO/IAEA Working Document, **2000**, 4.
- [29]. K.R. Marckam, "Methods in Plant Biochemistry", Academic Press, London, **1989**, 16.
- [30]. N. Abe, T. Murata, A. Hirota, *Bioscience, Biotechnology, Biochemistry*, **1998**, 62, 661.

## STATISTICAL PROCESSING AND DYNAMIC MODELING OF AN ALCOHOLIC FERMENTATION PROCESS

ANCA ȘIPOȘ<sup>a</sup> AND ÁRPÁD IMRE-LUCACI<sup>b,\*</sup>

**ABSTRACT.** The experimental data obtained in this research work were used in combination with the response surface planning method, modeling and simulation to determinate the variables with major influence on the length of an alcoholic fermentation process. Then, based on the periods according to yeast cells physiological phases a non-linear, dynamic mathematical model for the same process was developed. This model involves equations corresponding to physiological phases of yeast cells, heat transfer equations and the dependence of kinetic parameters on temperature.

**Keywords:** *alcoholic fermentation process, response surface method, dynamic model*

### INTRODUCTION

The alcoholic fermentation of white wine process is characterized for its complex dynamic response. The alcoholic fermentation in food industry have particular characteristics include the following: batch fermentation on natural complex media, anaerobic conditions due to CO<sub>2</sub> production, the composition of the grape juice, the, low media pH, the levels of the sulphur dioxide, the inoculation with selected yeasts and the interaction with other microorganisms. The models developed for this process consequently include the substrate inhibition of: microbial growth, substrate sugars and ethanol concentrations [1, 2, 3]. Many of these models offered good prediction of the important process variables, but most deviate significantly from the final ethanol concentration [4, 5]. The dead time, time delay in the instrument measurements, presence of variables that vary with time and high

---

<sup>a</sup> *Lucian Blaga University, Faculty of Agricultural Sciences, Food Industry and Environmental Protection, 5-7 Ion Rațiu Str., RO-550012, Sibiu, Romania*

<sup>b</sup> *Babeș-Bolyai University, Faculty of Chemistry and Chemical Engineering, 11 Arany Janos Str., RO-400028, Cluj-Napoca, Romania*

\* *Corresponding author: aimre@chem.ubbcluj.ro*

nonlinearities involving the variables are some examples that confirm the below affirmation [1]. For these reasons, modeling, simulation, and control of this system is still not a totally resolved problem.

In this article the author presents data base obtained on an alcoholic fermentation process that was made using different initial concentrations in yeast and sugar and also different temperatures in process control. All these data were processing by statistical models.

Statistical models are obtained by correlating experimental data [6]. Designing an empirical model does not require detailed representation of the mechanism of the real process; this also gives empirical models simplicity and consequently great versatility which sometimes is desirable.

In general, in designing a statistical model there must be taken the following steps [7]: determine the model structure; organizing and conducting experiments in the real process; interpreting and processing the results; deduction of the final form of the model equations and the calculation of the model coefficients and finally check of the validity of the model by analyzing the dispersion.

All these steps were made using the response surface planning method. The response surface design was used in a simulation study to determine the variables with major influence on the length of fermentation process. The variables selected to be observed in this study were: temperature, substrate concentration and yeast concentration.

The study was continued with a non-linear, dynamic mathematical model developed in periods, according to yeast cells physiological phases. The model presented, besides the detailed kinetic model, involves equations corresponding to physiological phases of yeast cells, heat transfer equations and the dependence of kinetic parameters on temperature. As a distinct modeling principle of each phase, the evolution curve of biomass in time, afferent to viable cells was used. The model was validated with the experimental obtained data.

This proposed mathematical model is taking part from an author's study concerning the estimation of state and parameters of fermentation process and the process control by expert system.

## RESULTS AND DISCUSSION

### ***Results for statistical model simulation***

Using functions included in *Statistics Toolbox* from MATLAB computational software different second-degree polynomial empirical models were tested. The best fitted model was of the form:

$$t = c_0 + c_1 T^0 + c_2 X + c_3 T^0 S + c_4 X^2 \quad (1)$$

The coefficients  $c_0, \dots, c_4$  of the polynomial model (1) were calculated using MATLAB function *regress* and the obtained equation is:

$$t = 1066.864 - 2.6196 T^0 + 13.3294 X - 0.0036 T^0 S - 0.6452 X^2 \quad (2)$$

The residual values calculated weren't high. The difference between experimental and estimated by the model presented in eq. (2) values was less than 3 % as it can be seen in Table 1.

**Table 1.** Comparison between experimental and model data

Experiment	Duration of the fermentation process, $t$			
	Measured, [h]	Calculated, [h]	Difference	
			[h]	[%]
1	76	76.67	0.67	0.87
2	49	49.67	0.67	1.34
3	95	95.67	0.67	0.70
4	76	74.00	-2	-2.70
5	101	101.00	0	0
6	59	59.00	0	0

The response surface modelling window (opened by the *rstool* function from MATLAB) constructed on the statistical equation is presented in Figure 1. This interactive interface is part of the *Statistics Toolbox* included in the MATLAB computing software environment where a sequence of plots are displayed, each showing a contour of the response surface against a single parameter, with all other parameters held fixed.

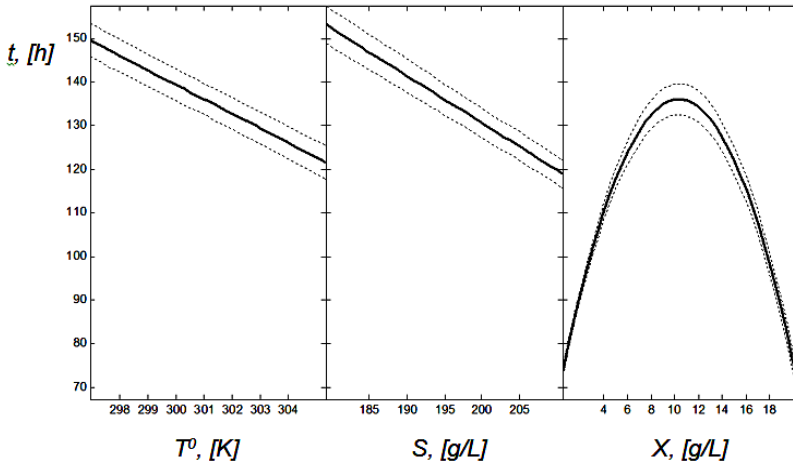


**Figure 1.** The *rstool* window of the statistical model where with solid lines are representing the response of the model and with dotted lines the interval for a global confidence of 0.95

From these graphical representations it can be observed the form of the response surface model obtained.

Studying this statistical equation it can be observed the followings:

1. The high value of free term shows that other factors also exist that influence the fermentation process. These factors can be: nutrients content, vitamins content of the grapes must etc.
2. The temperature influence on the fermentation process is emphasized by the high value of its coefficient that corresponds to the reality.
3. The value of  $X$  coefficient demonstrates that the strain of selected yeast used in fermentation is very important. The sort of yeast can influence the fermentation rate, the duration of the process and so the final alcohol and aroma concentrations.
4. The combined action of the temperature and substrate concentration (the sugars fermentescible content) is weak but in negative sense. This observation confirms the fact that a great content in substrate leads to a slow fermentation (a high concentration in substrate can be an inhibitor for the yeast development). Also, a weaker content in sugar can lead to a very short fermentation with a low concentration in alcohol at the end, without aromas and with a high rate of  $\text{CO}_2$  production for a short period.

### ***Results for dynamic mathematical model simulation***

Batch fermentation nonlinear mathematical model has the following aspects: an equation for latent phase of fermentation that describes the phase period of the dependence with temperature; the Aiba model for exponential growing phase and Bovée-Strehaiano model for decay phase with two equations: one for substrate consumption and the other for alcohol formation; an equation that describes the biomass behavior along the fermentation, different for the Phase 2 and for the Phase 3, respectively; and an energy balance model in which the rate of change of mass of reaction temperature ( $dT^0/dt$ ) is a result of the balance between the rate of heat generation due to fermentation and the rate of heat transfer to the cooling medium from the bioreactor jacket. The Aiba model was chosen because it introduces the ethanol inhibitory effect and Bovée-Strehaiano model has accurately describes for the substrate consumption and the evolution of the alcohol concentration in the decay phase.

For latent phase a linear equation was obtained, describing the dependence of the phase period on temperature. The equation is valid for a period between 0–100 h, a period confirmed by the data in the literature [8].

Figure 2 presents the fitting curve calculated by the polynomial regression method.

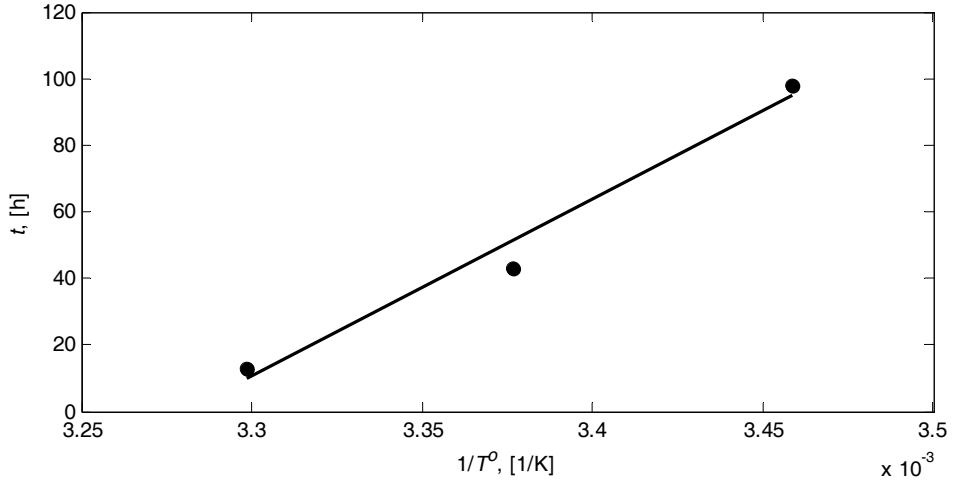


**Figure 2.** The tendency curve for latent phase, calculated based on experimental data

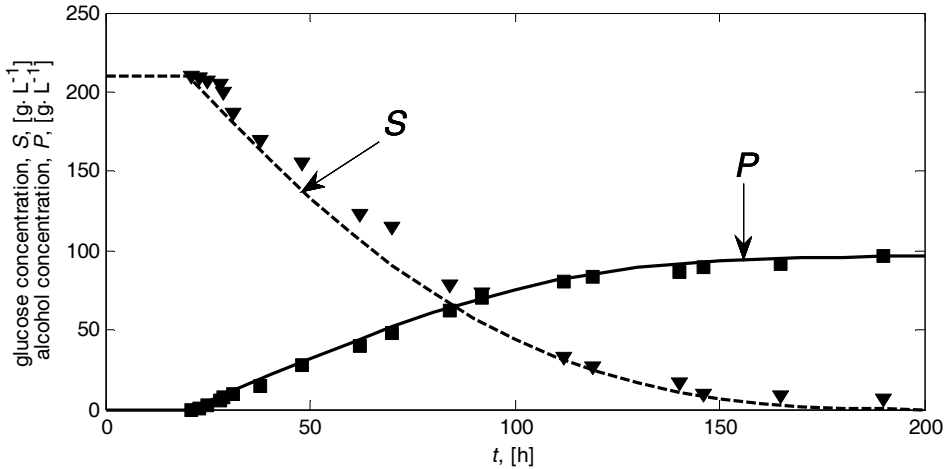


**Figure 3.** Authors' model: The evolution of glucose and alcohol versus time, comparison between experimental values ( $\blacktriangledown$  glucose,  $\blacksquare$  alcohol) and simulation results (lines)

The simulation results considering this model are presented in Figures 3, 4 and 5, for  $210 \text{ g} \cdot \text{L}^{-1}$  substrate initial concentration and 301 K fermentation temperature.

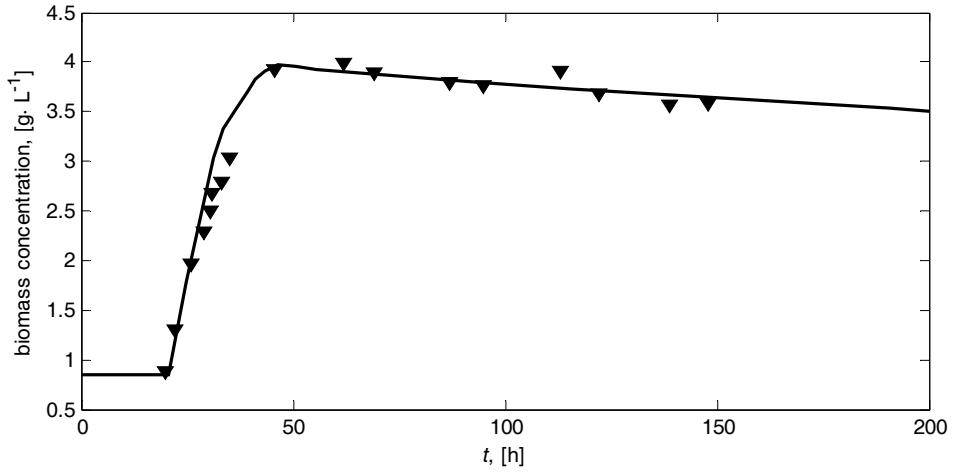


**Figure 4.** Authors' model: Comparison of biomass simulation results (line) with experimental ones (▼)

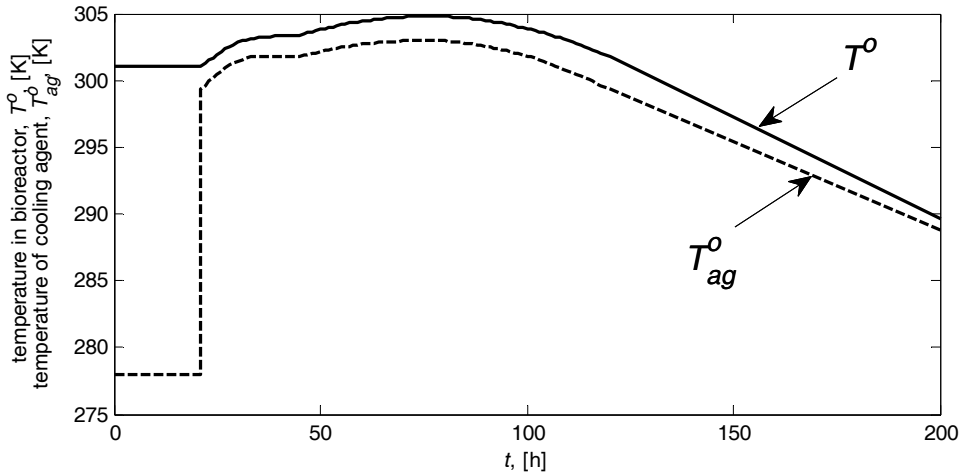


**Figure 5.** The temperatures of fermentation medium and cooling agent simulation

The maximal difference between experimental and simulation results are less than 10 %. The model has been tested for a grape must with an initial concentration in substrate varying between 180 and 210 g·L<sup>-1</sup>, a fermentation temperature between 299 and 303 K and without aeration.

## CONCLUSIONS

In the present article the authors proposed a statistical model for the classic alcoholic fermentation process of the white wine by correlating the experimental data. This model emphasizes the influence of some variables to the fermentation process length (temperature, initial substrate concentration and initial biomass concentration). The interpretation of the simulation results was made by using the response surface planning method. Then, based on these observations a dynamic mathematical model was developed and validated. The system is described by a set of non-linear equations corresponding to the physiological phases of yeast cells: substrate, biomass and alcohol dynamic behaviour, heat transfer equations and the dependence of kinetic parameters on temperature. The results obtained in this research work permitted to the authors to continue with the estimation of the singular and in group influences of input variables – substrate and biomass – on the fermentation process and to design the suitable control technique.

## EXPERIMENTAL

The alcoholic fermentation process of the white wines has been studied in the research laboratory of Modeling, simulation and advanced control of the technological processes and bio-processes from food industry, "Lucian Blaga" University of Sibiu, the Faculty of Agricultural Sciences, Food Industry and Environmental Protection.

In the first part, the research experiments have been focused on the influence of some variables to the fermentation process length,  $t$ . The selected variables were: temperature,  $T^0$ ; substrate concentration,  $S$  and biomass concentration,  $X$ . The medium used for inoculums and culture contained: *Saccharomyces cerevisiae* yeast wine YEPD,  $5 \text{ g}\cdot\text{L}^{-1}$   $\text{KH}_2\text{PO}_4$ ,  $2 \text{ g}\cdot\text{L}^{-1}$   $(\text{NH}_4)_2\text{SO}_4$ ,  $0.4 \text{ g}\cdot\text{L}^{-1}$   $(\text{MgSO}_4) \times 7\text{H}_2\text{O}$  and fermentation medium formed by malt extract. The content in sugar of malt extract was matched with saccharose, if was necessary. A EVO continuously stirred bioreactor equipped with pH, temperature, level and stirred speed control, dissolved  $\text{O}_2$ , emitted  $\text{CO}_2$  and  $\text{O}_2$  sensors and analysers was used [9].

### ***Fermentation parameters measurements***

The cells concentration has been calculated on the base of three different parameters: optical density, dry substance and total cells number (Thoma room method). The glucose has been measured by DNS method and the alcohol by high performance liquid chromatography (HPLC).

The operating values of the variables are presented in Table 2.

**Table 2.** The operating values of the considering variables and the periods of fermentation processes

Experiment' number	Temperature, $T^0$ [K]	Initial substrate concentration, $S_0$ [g·L <sup>-1</sup> ]	Initial biomass concentration, $X_0$ [g·L <sup>-1</sup> ]	Duration of fermentation process, $t$ [h]
1	297	210	1	76
2	305	210	1	49
3	301	180	1	95
4	301	200	1	76
5	301	210	5	101
6	301	210	20	59

These experimental data were used by the response surface methodology to obtain an empirical model of the process to correlate the response of the system, the duration of the fermentation process with the considered parameters of the process: temperature; initial substrate concentration and initial biomass concentration. Necessary calculation were performed using MATLAB computing software.

In the second part, the research work was continued with the experiments necessary to develop a non-linear, dynamic mathematical model for the alcoholic fermentation process.

The operating variables and parameters for the experimental plant were as follows: working volume 8 L; temperature: 291 K and 301 K; stirring speed 150 rpm.; pH 3.8 and influent glucose concentrations: 180 g·L<sup>-1</sup> and 210 g·L<sup>-1</sup>.

Without aeration, the necessary oxygen was that dissolved in malt extract.

In the dynamic mathematical model, as a distinct modeling principle of each phase, the evolution curve of biomass over the time for the viable cells has been used. The evolution of yeast population curve has been divided in correlation with phenomenological aspects of the development of microorganisms as follows: latent phase, growing phase and decay phase.

The equations of this model are presented in Table 3.

The parameters of the model were adjusted by means of non-linear programming methods, which compare model predictions with experimental data and minimize the errors. The variables and parameters of the model are presented in Tables 4 and 5.

Also, in MATLAB simulation system the numerical simultaneous integration of the model equations has been done.

**Table 3.** The equations of the proposed model

Phase	Equations
<b><i>Kinetic model</i></b>	
Latent phase [10]	$t_{lat} = \frac{a}{T^0} + b; a = 558,002 \text{ and } b = 1,833.2$
- biomass:	$\frac{dX}{dt} = \mu_{max} \cdot \left( \frac{S}{K_S + S} \right) \cdot e^{-K_p \cdot P} \cdot X$
Exponential growing phase [11]	$\mu_{max} = A_1 \cdot e^{-\frac{E_{a1}}{R \cdot T^0}} - A_2 \cdot e^{-\frac{E_{a2}}{R \cdot T^0}}$
- alcohol:	$\frac{dP}{dt} = q_{pmax} \cdot \left( \frac{S}{K_{SP} + S} \right) \cdot e^{-K_{pp} \cdot P} \cdot X$
- substrate:	$\frac{dS}{dt} = - \left( \frac{1}{Y_{XS}} \cdot \frac{dX}{dt} \right) - \left( \frac{1}{Y_{PS}} \cdot \frac{dP}{dt} \right)$
Decay phase [10,12]	- biomass: $\frac{dX}{dt} = f \cdot X \cdot k; k = A \cdot e^{-\frac{E_a}{R \cdot T^0}}$
- alcohol:	$P = P_0 + \eta \cdot (S_0 - S)$
- substrate:	$\frac{dS}{dt} = -k \cdot S^\alpha \cdot P^\beta$
<b><i>Energetic model</i></b>	
- for bioreactor:	$\frac{\Delta Hr \cdot \frac{dS}{dt}}{\rho \cdot c_p} - \frac{K_T \cdot A_T}{V \cdot \rho \cdot c_p} (T^0 - T_{ag}^0) = \frac{dT^0}{dt}$
All phases [10] - for bioreactor's jacket:	$\frac{F_{ag}}{V_{ag}} (T_{agi}^0 - T_{ag}^0) + \frac{K_T A_T}{V_{ag} \cdot \rho_{ag} \cdot c_{pag}} (T^0 - T_{ag}^0) = \frac{dT_{ag}^0}{dt}$

**Table 4.** Variables and parameters of the kinetic model

$X$	Biomass concentration		$\text{g}\cdot\text{L}^{-1}$
$S$	Substrate concentration		$\text{g}\cdot\text{L}^{-1}$
$P$	Alcohol concentration		$\text{g}\cdot\text{L}^{-1}$
$k$	Kinetic constant		$\text{h}^{-1}$
$A$	Pre-exponential factor in Arrhenius' equation	148 (calculated using experimental data)	$\text{h}^{-1}$
$E_a$	Activation energy	21,424 (calculated using experimental data)	$\text{J}\cdot\text{mol}^{-1}$
$A_1$	Pre-exponential factor in Arrhenius' equation	$9.5\cdot 10^{8\text{a}}$	$\text{h}^{-1}$
$E_{a1}$	Activation energy	55,000 <sup>a</sup>	$\text{J}\cdot\text{mol}^{-1}$
$A_2$	Pre-exponential factor in Arrhenius' equation	$2.55\cdot 10^{33}$	$\text{h}^{-1}$
$E_{a2}$	Activation energy	220,000 <sup>a</sup>	$\text{J}\cdot\text{mol}^{-1}$
$R$	Universal gas constant	8.31	$\text{J}\cdot\text{mol}^{-1}\text{K}^{-1}$
$T^0$	Temperature in bioreactor	291 and 301	K
$K_s$	Substrate limitation constant	0.2 <sup>a</sup>	$\text{g}\cdot\text{L}^{-1}$
$d$	Pseudo-constant of the biomass	1.67 (calculated using experimental data)	
$f$	Pseudo-constant of the biomass	0.34	
$\alpha$	Pseudo-order of the substrate	0.69 <sup>b</sup>	
$\beta$	Pseudo-order of the alcohol	0.32 <sup>b</sup>	
$\eta$	Efficiency in alcohol of fermentation reaction	48 <sup>b</sup>	%
$S_0$	Steady-state operation point of substrate	180	$\text{g}\cdot\text{L}^{-1}$
$P_0$	Steady-state operation point of alcohol	0	$\text{g}\cdot\text{L}^{-1}$
$t$	Time		h
$\mu_{max}$	Maximum specific growth rate		$\text{h}^{-1}$
$K_P$	Alcohol limitation constant	0.14 <sup>c</sup>	$\text{g}\cdot\text{L}^{-1}$
$q_{pmax}$	Maximum specific alcohol production rate	1.02 <sup>c</sup>	$\text{g}\cdot\text{g cells}^{-1}\text{h}^{-1}$
$K_{SP}$	Constant in the substrate term for ethanol production	1.68 <sup>c</sup>	$\text{g}\cdot\text{L}^{-1}$
$K_{PP}$	Constant of fermentation inhibition by ethanol	0.07 <sup>d</sup>	$\text{g}\cdot\text{L}^{-1}$
$Y_{XS}$	Ratio of cell produced per glucose consumed for growth	0.607 <sup>d</sup>	$\text{g}\cdot\text{g}^{-1}$
$Y_{PS}$	Ratio of ethanol produced per glucose consumed for fermentation	0.435 <sup>c</sup>	$\text{g}\cdot\text{g}^{-1}$

<sup>a</sup>[4, 13, 14];<sup>b</sup>[12]; <sup>c</sup>[15];<sup>d</sup>[16]

**Table 5.** Parameters of the kinetic model

$K_T$	Heat transfer coefficient	$3.6 \cdot 10^5$ <sup>a</sup>	$\text{J} \cdot \text{m}^{-2} \cdot \text{K}^{-1} \cdot \text{h}^{-1}$
$A_T$	Heat transfer area	$0.8$ <sup>b</sup>	$\text{m}^2$
$F_{aq}$	Flow of cooling agent	$0.01$ <sup>b</sup>	$\text{m}^3 \cdot \text{h}^{-1}$
$V_{aq}$	Volume of the jacket	$0.002$ <sup>b</sup>	L
$V$	Volume of the mass of reaction	$1$ <sup>b</sup>	L
$T_{aqi}^0$	Temperature of cooling agent at jacket inlet	$278$ <sup>b</sup>	K
$\Delta H_r$	Reaction heat of fermentation	$-98,465$ <sup>c</sup>	$\text{J} \cdot \text{mol}^{-1}$
$\rho$	Density of the mass of reaction	$1,100$ <sup>b</sup>	$\text{kg} \cdot \text{m}^{-3}$
$\rho_{aq}$	Density of cooling agent	$999.8$ <sup>a</sup>	$\text{kg} \cdot \text{m}^{-3}$
$c_p$	Heat capacity of mass of reaction	$3,391$ <sup>b</sup>	$\text{J} \cdot \text{kg}^{-1} \cdot \text{K}^{-1}$
$c_{p, aq}$	Heat capacity of cooling agent	$4,217$ <sup>a</sup>	$\text{J} \cdot \text{kg}^{-1} \cdot \text{K}^{-1}$
$T_{aq}^0$	Temperature of cooling agent in the jacket		K

<sup>a</sup>[17]; <sup>b</sup>experimental data; <sup>c</sup>[18]

## REFERENCES

- [1]. L.A.C. Meleiro, R. Maciel Filho, *Computers & Chemical Engineering*, **2000**, *24*, 925.
- [2]. Y. Zhang, M.A. Henson, Y.G. Kevrekidis, *Chemical Engineering Science*, **2003**, *58*, 429.
- [3]. M. Remedios, *American Journal of Enology and Viticulture*, **1999**, *50*, 166.
- [4]. F. Lei, M. Rotboll, S.B. Jorgensen, S.B., *Journal of Biotechnologies*, **2001**, *88*, 205.
- [5]. G. Martinez, A. Lopez, A. Esnoz, P. Virseda, J. Ibarrola, *Fd. Control*, **1999**, *10*, 175.
- [6]. D.M. Himmelblau, K.B. Bischoff, "Process analysis and simulation", John Wiley & Sons Inc., New York, **2001**.
- [7]. V. Mărinoiu, C. Strătuță, A. Petcu, "Metode numerice aplicate în ingineria chimică (Numerical methods applied in chemical engineering)", Editura Tehnică, Bucharest, **1986**.
- [8]. J. Blouin, É. Peynaud, "Connaissance et travail du vin", Dunod, Paris, **2001**.
- [9]. <http://www.dci-bio.com/products/bioreactors/biocell-evo-series-bioreactors/>, accessed in September 16, 2014.
- [10]. A. Șipoș, X.M. Meyer, P. Strehaiano, *Acta Alimentaria*, **2007**, *36*, 429.

- [11]. S. Caraman, E. Ceangă, L. Frangu, G. Mencinicopschi, "Modelarea și conducerea proceselor biotehnologice (Modeling and control of biotechnological processes)", Editura Didactică și Pedagogică, Bucharest, **2002**.
- [12]. J.P. Bovée, P. Strehaiano, G. Goma, Y. Sevely, *Biotechnology and Bioengineering*, **1984**, 26, 328.
- [13]. M. Krothapally, S. Palanki, *ISA Transactions*, **1999**, 38, 383.
- [14]. S. Valentinotti, B. Srinivasan, U. Holmberg, D. Bonvin, C. Cannizzaro, M. Rhiel, U. von Stockar, *Control Engineering Practice*, **2003**, 11, 665.
- [15]. C. Karakuzu, M. Turker, S. Ozturk, *Control Engineering Practice*, **2006**, 14 (8), 959.
- [16]. L.S. Ferreira, M.B. De Souza Jr., R.O.M. Folly, *Sensors and Actuators B*, **2001**, 75, 166.
- [17]. M.A.J. Torija, N. Rozès, M. Poblet, J.M. Guillamón, A. Mas, *International Journal of Food Microbiology*, **2003**, 80, 47.
- [18]. A.C. Costa, D.I.P. Atala, F. Maugeri, R. Maciel, *Process Biochemistry*, **2001**, 37, 125.

## BIOMASS GASIFICATION – BASED HYDROGEN PRODUCTION SUPPLY CHAIN ANALYSIS UNDER DEMAND VARIABILITY

MIRELA MURESAN<sup>a</sup>, CALIN-CRISTIAN CORMOS<sup>a,\*</sup>,  
PAUL-SERBAN AGACHI<sup>a</sup>

**ABSTRACT.** In this paper, a discrete event model is developed in order to address biomass gasification based hydrogen production supply chain analysis under demand variability, with Arena software. Hydrogen production supply chain system is evaluated in terms of: hydrogen amount sold and hydrogen amount stored (MW-h), hydrogen lost sales amount (MW-h), partial sales per cent and gasification plant profit (MM Euros). Hydrogen production supply chain assessment under demand variability provide a “what if” analysis and help foresee how hydrogen demand variability, hydrogen delivery distance variation and hydrogen production cost variation would affect the entire biomass gasification based hydrogen production supply chain, especially the gasification plant, during one year time frame (8000 working hours). In order to reduce the wood chips quality degradation and dry matter losses risks over the storage period and to meet the gasification reactor requirements in terms of raw material properties a stock optimization is performed in Arena OptQuest resulting in a decrease of wood chips stock at the gasification plant and at the biomass warehouse. Hydrogen demand variation result is a decrease of gasification plant profit. Also, hydrogen delivery distance influence on gasification plant profit is more pronounced when hydrogen demand variation is higher.

**Keywords:** *Biomass, Gasification, Supply chain, Hydrogen production.*

### INTRODUCTION

Due to outgrowing competitiveness on the market, supply chain analysis and optimization become a matter of great importance in maximizing global system revenue [1]. Supply chain analysis through discrete event simulation techniques can be applied to various types of processes from the pharmaceutical industry, food industry, chemical processes, energy conversion systems, etc. resulting in increased profit, increased service levels, better process understanding [1].

---

<sup>a</sup> Faculty of Chemistry and Chemical Engineering, Babes-Bolyai University, 11 Arany Janos, RO-400028, Cluj-Napoca, Romania

\* Corresponding author: cormos@chem.ubbcluj.ro

Given the continued growth in the world's population and demands for higher standards of living and better air quality as well as the progressive industrialization of developing nations, the global demand for energy is expected to continue to escalate in the coming decades [2, 3]. Currently, the world energy production systems are mostly based on fossil fuels exploitation (oil for transportation, coal and natural gas for heating and electricity generation), resulting in large amounts of carbon dioxide emissions, main responsible for climate change and global warming [4]. The current fossil fuel systems must be changed gradually to clean and reliable energy systems, enabling to reach the sustainable vision of future energy systems [5].

Hydrogen is an energy carrier that has the potential to become a significant source of energy generation in the future, both in the transportation sector as well as for power generation [6], but in order to achieve the vision of a sustainable hydrogen based economy the entire hydrogen supply chain system must be considered, from the raw materials production, preparation and storage stages to the hydrogen production and delivery stages [7].

In this paper, a discrete event model is developed in order to address biomass gasification based hydrogen production supply chain analysis under demand variability, with Arena software. Hydrogen production supply chain system is evaluated in terms of: hydrogen amount sold and hydrogen amount stored (MW-h), hydrogen lost sales amount (MW-h), partial sales per cent and gasification plant profit (MM Euros).

This paper focuses on assessing the biomass gasification based hydrogen production supply chain, from the raw material supply, preparation and storage stages to the hydrogen production stage, from which hydrogen is delivered to consumers by pipeline transportation, as depicted in Figure 1.

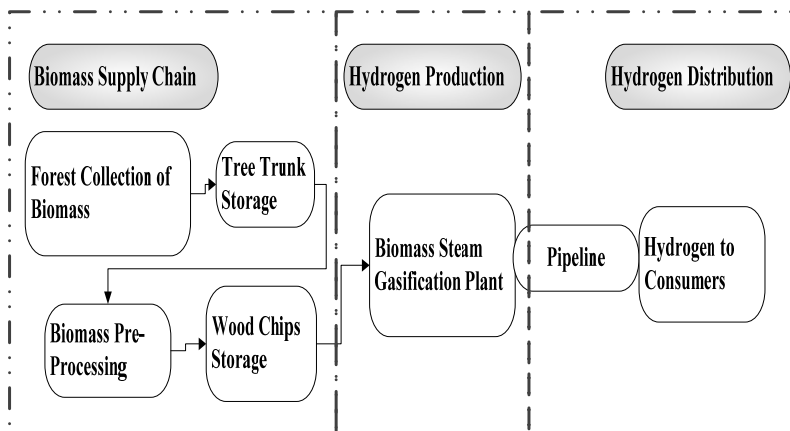


**Figure 1.** Hydrogen production supply chain (adapted from [7])

## PROCESS DESCRIPTION

### A. Biomass supply chain

Biomass represents a renewable resource that is CO<sub>2</sub> neutral, making it suitable for hydrogen production as the concern of global warming increases [8]. Biomass characteristics are determined by two type of analysis: ultimate and proximate analysis. The information provided by those analysis and also the calorific determination (high heating values and lower heating values) are used for evaluating the suitability for given application (hydrogen production by gasification in this case) [9]. The characteristics of biomass used as feedstock to the gasifier are given in the Table 1 [10].

**Table 1.** Biomass characteristics

Parameter	Units	Dry basis
Ash content	[wt.%]	0.29
Volatiles	[wt.%]	86.45
Fixed carbon	[wt.%]	13.26
Carbon	[wt.%]	50.23
Hydrogen	[wt.%]	6.04
Nitrogen	[wt.%]	0.05
Oxygen	[wt.%]	43.382
Sulphur	[wt.%]	0.005
Chlorine	[wt.%]	0.003
LHV	[MJ/kg]	13.61

The following activities are required to supply biomass from its production point to the gasification plant in order to be used as raw material for hydrogen production: collection of biomass in the forest, loading and unloading operations, transportation through the supply chain nodes, storage and pre-processing operations [11]. For the present study it is assumed that the wood is supplied from the surrounding area of hydrogen production plant, from within a radius of 25 kilometers and the wood trunks are dried naturally by open air storage for about 1-2 years [12], then they are pre-processed at the biomass pre-processing plant. Biomass pre-processing in this case involves chipping operations.

Storage throughout the biomass chain is necessary to adequately match biomass supply and hydrogen production plant demand [13]. Storage options depend on the climate, storage period, biomass processing stage and may vary from open air, roof covered and air fan [13]. Wood chips storage type for the present case is assumed to be roof covered.

## **B. Biomass gasification plant**

There are different technologies for biomass conversion to hydrogen based either on bio-chemical or thermo-chemical processes, but main focus is the gasification of woody biomass for which various process concepts and reactor designs have been developed [14]. The hydrogen production process chosen for this study is based on biomass steam gasification in dual fluidized bed reactor system, process developed at the Institute of Chemical Engineering, Vienna University of Technology. Detailed description of the DFB system can be found in [10,15-17].

The results of an Aspen Plus<sup>®</sup> simulation model [18] for the hydrogen production process based on biomass steam gasification in dual fluidized bed reactor system are used as inputs for developing the Arena discrete event simulation model of the hydrogen production supply chain system. The main overall gasification plant performance parameters resulted from Aspen Plus<sup>®</sup> simulation and used as inputs for the Arena model are given in Table 2 [18].

**Table 2.** Main plant performance parameters

Parameter	Units	Value
Biomass input (40% wet, wf)	t/h	18.76
Biomass (LHV)	MJ/kg	9.59
Biomass input	MW	50
Hydrogen output	Nm <sup>3</sup> /h	11807
Hydrogen (LHV)	MJ/Nm <sup>3</sup>	10.79
Hydrogen output	MW	35.39
$\eta_{\text{hydrogen}}$	%	70.78

## **C. Hydrogen distribution and storage**

Hydrogen can be stored as liquid hydrogen, main advantage being its high density at low pressure, making it efficient for truck delivery [19] or as compressed gas in high pressure vessels, method preferred for fuel cell vehicle use, because of the affordable cost and the possibility of indefinite time storage [20,21].

There are several ways of hydrogen delivery: compressed gas truck delivery, cryogenic liquid truck delivery and delivery by pipeline, the latter being the cheapest option with the highest capacity of hydrogen delivery [21]. For the present study it is assumed that hydrogen is delivered to consumers by pipeline transportation. High pressure is needed to ensure the transportation from production sites to end-users with low energy consumption (pressure drop along pipes network).

**METHODOLOGY AND MODELING ASSUMPTIONS**

A discrete event model is developed in order to address hydrogen production supply chain analysis under demand variability, during one year time period (8000 working hours). The model is developed using Arena software and it is based on the methodology described by Tayfur and Melamed [22]. The biomass gasification-based hydrogen production supply chain consist of the following stages: biomass supplier, biomass pre-processing plant, wood chips warehouse, biomass gasification plant where the hydrogen demand arrives, as depicted schematically in Figure 2.

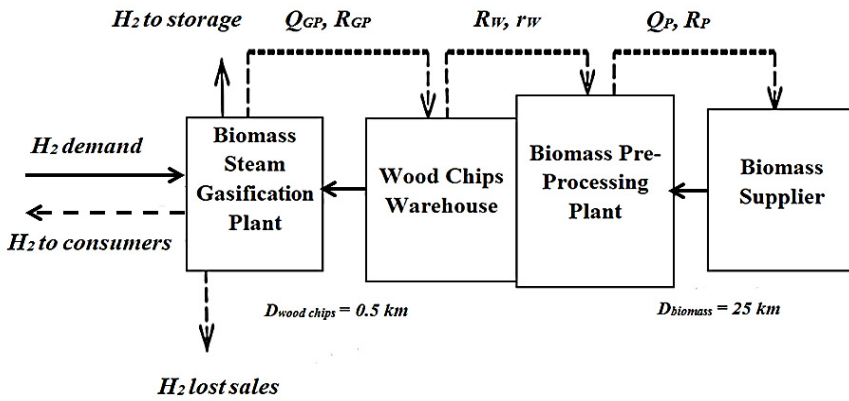


**Figure 2.** Gasification based hydrogen production supply chain structure (adapted from [7])

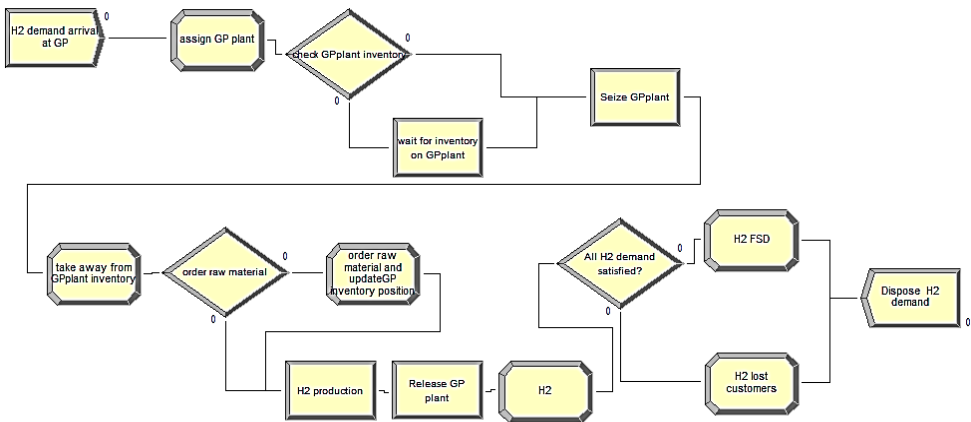
Whenever the gasification plant biomass inventory down-crosses level  $R_{GP}(i)$ , a replenishment of quantity  $Q_{GP}(i)$  is ordered from the wood chips warehouse. The unsatisfied demand quantity is backordered from the warehouse [7]. The wood chips warehouse also uses a continuous review ( $r_w(i), R_w(i)$ ) policy [22]. The biomass at the pre-processing plant is ordered from the supplier. The biomass pre-processing plant orders assumed to be always fully satisfied, and the inventory control policy is a continuous review ( $Q_P(i), R_P(i)$ ) policy [22]. The inventory control parameters are given in Table 3.

**Table 3.** Inventory control parameters (tonnes)

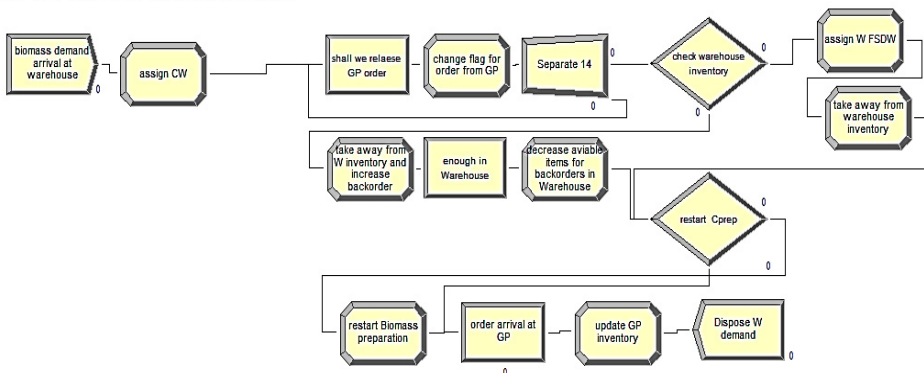
Biomass Gasification Plant	Wood Chips Warehouse	Biomass Pre-Processing Plant
$R_{GP} = 450.24$	$R_W = 1350.72$	$R_P = 706400$
$Q_{GP} = 112.56$	$r_W = 900.48$	$Q_P = 529.68$

Each of the biomass gasification-based hydrogen production supply chain stage is modeled in Arena using a series of blocks as depicted in Figure 3. The gasification plant stage is subjected to the following events: hydrogen *demand arrival*, wood chips *inventory check*, *order more raw material from the wood chips warehouse* if necessary, hydrogen production, wood chips *inventory updating*, hydrogen *delivery to customers*, hydrogen *inventory update* and *gasification plant profit calculation*. The other stages are subjected to similar events (biomass *order arrival*, *inventory check* and *updating*, *order shipment*).

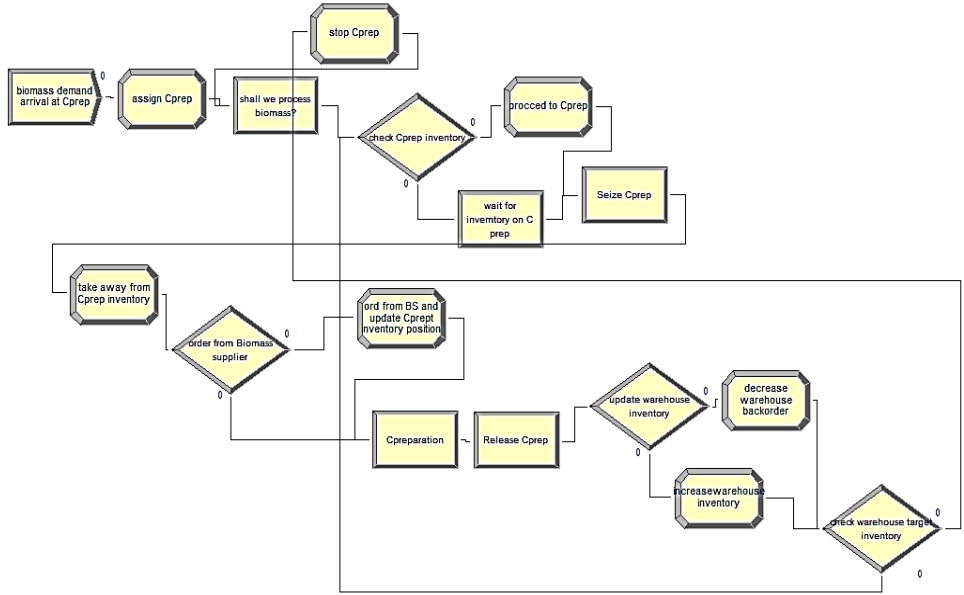
**BIOMASS GASIFICATION PLANT**



**WOOD CHIPS WAREHOUSE**



**BIOMASS PREPARATION PLANT**



**BIOMASS SUPPLIER**

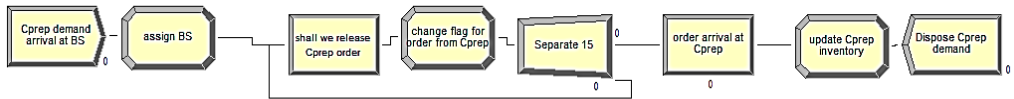


**Figure 3.** Arena model block diagram

The main Arena model input data are presented in Table 4. Hydrogen production cost is estimated from [23], hydrogen storage and delivery cost derived from [21]. Hydrogen is considered to be stored as compressed gas, for short term and delivered to consumers by pipeline transportation. Gasification plant profit is calculated at each discretization step, with Equation 1 and the value obtained is added to the profit value obtained from the previous step.

$$\text{Profit}_{\text{GP}} = (H_{2\text{MP}} - H_{2\text{DC}} \times D_{\text{distance}}) \times H_{2\text{ASold}} - H_{2\text{PC}} \times H_{2\text{AProduced}} - H_{2\text{SC}} \times H_{2\text{AStored}} \quad (1)$$

**Table 4.** Arena model input data

Tree trunk quantity	22.07 t/h
Chipping efficiency	85%
Wood chips input	18.76 t/h
Wood chips input (LHV)	50 MW
Moisture content	40%
Hydrogen output (LHV)	35.39 MW
Hydrogen production cost <sup>a</sup>	120 €/MW
Hydrogen storage cost <sup>b</sup>	5.3 €/MW
Hydrogen delivery cost <sup>c</sup>	12.21 €/MW/100 km
Hydrogen market price <sup>d</sup>	145 €/MW

<sup>a, b, c</sup> based on LHV, 1 € = 1.35 US \$ [24], <sup>d</sup> ( $\sum a, b, c$ ) + 5% mark-up

In order to assess the biomass gasification based hydrogen supply chain the following cases are considered: hydrogen demand at the gasification plant is considered to: i) be equal to hydrogen production rate and hydrogen delivery distance is 50 km (Base case), ii) follow a TRIA (min, mlv, max) distribution of  $\pm 5\%$  of hydrogen production rate and hydrogen delivery distance is 50 km (Case 1), iii) follow a TRIA (min, mlv, max) distribution of  $\pm 10\%$  of hydrogen production rate and hydrogen delivery distance is 50 km (Case 2). Also for each of the cases considered hydrogen delivery distance is varied according to: i) UNIF (min, max) distribution between 10-50 km, ii) UNIF (min, max) distribution between 50-100 km. For the “Base case” hydrogen production cost is varied: i) between 100 and 120 €/MW (Optimistic Case - OC) and ii) between 120 and 140 €/MW (Pessimistic Case - PC). If the available hydrogen amount is smaller than the hydrogen demand, the current hydrogen demand is partially satisfied, or if it is bigger than the hydrogen demand, the remaining hydrogen amount is stored.

Also the following assumptions are made: the biomass transportation delays (which include transportation time, loading and unloading operations duration) distribution is also UNIF (min, max); no partial orders are delivered (the shipment is delayed until full order becomes available); the wood chips warehouse is located in close vicinity of the pre-processing plant therefore the transportations delays are neglected. Biomass is supplied from the surrounding area of hydrogen production plant, from within a radius of 25 kilometers and the distance between the wood chips warehouse and the biomass steam gasification plant is around 0.5 km.

## RESULTS AND DISCUSSIONS

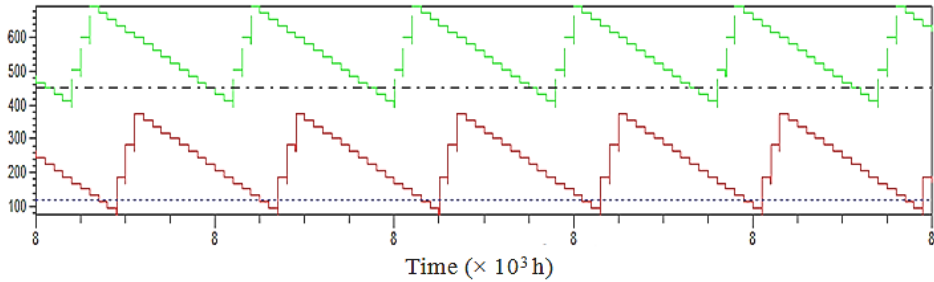
As mentioned above, the following assumptions are made for the Base case (BC): hydrogen demand variation is equal to hydrogen production rate, hydrogen delivery distance is 50 km and hydrogen production cost is 120 €/MW. 100 replications with 8000 hours length and 240 hours warm-up period are simulated. The results for the Base case are illustrated in Table 5.

**Table 5.** Base case simulation results

Time Persistent	Average value
Biomass pre-processing plant stock (t)	706458.31
Wood chips warehouse stock (t)	914.97
Gasification plant wood chips stock (t)	552.98
Output	Average value
Hydrogen amount sold (MW-h $\times 10^4$ )	28.31
Hydrogen amount stored (MW-h)	0.00
Hydrogen lost sales amount (MW-h)	0.00
Partial sales percent $\times 10^{-2}$ (%)	0.00
Profit (MM Euros)	5.35

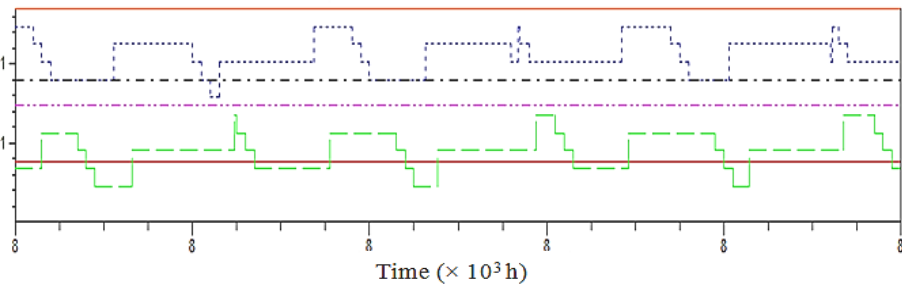
The profit registered by the biomass steam gasification plant is 5.35 MM euros for the Base case. In order to reduce the wood chips quality degradation and dry matter losses risks over the storage period and to meet the gasification reactor requirements in terms of raw material properties a stock optimization is performed in Arena OptQuest for the gasification plant and the warehouse. The gasification plant and warehouse wood chips stocks variations are illustrated in Figure 4 for simulation time between 7900 and 8000 working hours. As can be seen in Table 4 and Figure 4 the gasification plant and warehouse wood chips stocks are quite high (gasification plant: 552.98 tonnes of wood chips – average value, warehouse: 914.97 tonnes of wood chips – average value) and also the wood chips stocks are most of the time above the reordering points. The wood chips stored amount is decreased after the optimization is performed. The control variable for the gasification plant wood chips stock is  $R_{GP}$  (reordering point – if the wood chips stock at the gasification plant decreases below the reordering point a new reshipment of material is ordered from the warehouse). The control variable is varied between 20 and 460 tons of wood chips (with a step size of 20) and the objective function is the minimization of gasification plant wood chips stock. Similar optimization is performed for the warehouse wood chips stock. The control variables are  $r_w$  and  $R_w$ , and they are varied between 80 and 900 tons (step size 20), respectively between 240 and 1360 (step size 20).

Wood chips (tonnes)



- - -  $R_{GP}$  before optimisation      — Gasification plant stock before optimisation  
 - - -  $R_{GP}$  after optimisation      — Gasification plant stock after optimisation

Wood chips ( $\times 10^3$  tonnes)



—  $R_W$  before optimisation      ..... Warehouse stock before optimisation  
 - - -  $R_W$  after optimisation      - - - Warehouse stock after optimisation  
 - - -  $r_W$  before optimisation  
 —  $r_W$  after optimisation

**Figure 4.** Wood chips stock variation

For each optimization, 100 simulations are made with 100 replications each. The optimum value found for  $R_{GP}$  is 120 tonnes which corresponds to the objective function value of 234 tonnes (wood chips – average value for wood chips stock at the gasification plant). The best values found for  $R_w$  and  $r_w$  are 740 tonnes, respectively 380 tonnes and the objective function is 367.33 tons of wood chips (average value for the warehouse stock). After the optimization step, the gasification plant and warehouse wood chips stocks are decreased by 58%, respectively by 60%.

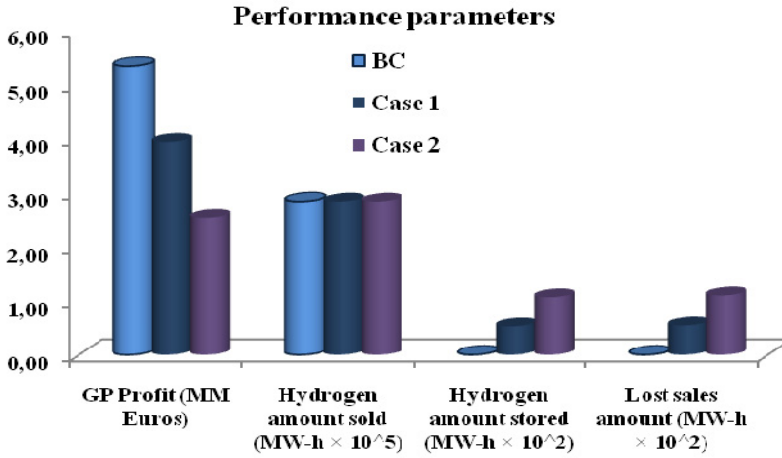


**Figure 5.** Hydrogen demand variation  
 ( $D_{\text{hydrogen delivery}} = 50 \text{ km}$ ,  $H_{2\text{production cost}} = 120 \text{ €/MW}$ )

Figure 5 illustrates the performance parameters considered for biomass steam gasification based hydrogen production supply chain analysis under demand variation. The gasification plant profit decreases by 26.3% for Case 1, respectively by 52.6% for Case 2, compared with the Base case. As hydrogen demand increases, hydrogen amount stored and hydrogen lost sales amount increase from zero at Base case to 53 MW-h and 55 MW-h for Case 1 and 106 MW-h and 110 MW-h for Case 2.

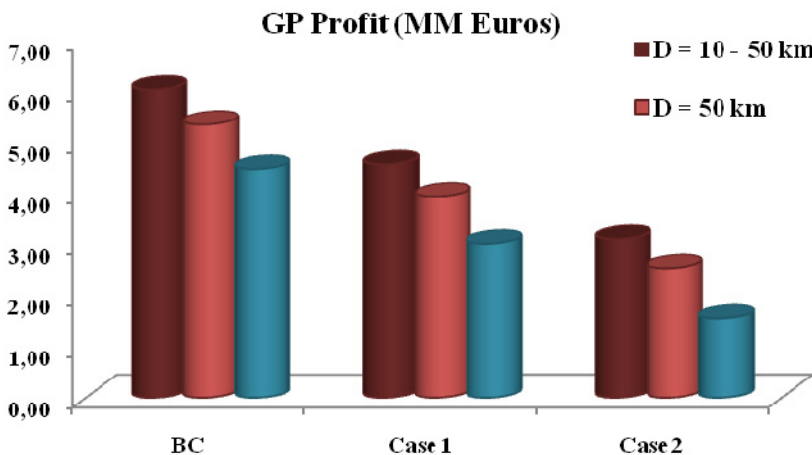


**Figure 6.** Hydrogen delivery distance variation  
 ( $H_{2\text{production cost}} = 120 \text{ €/MW}$ )

For each of the three cases considered, hydrogen delivery distance is varied from 50 km to 10- 50 km and 50-100 km. The gasification plant profit variation with hydrogen delivery distance is represented in Figure 6. For the base case hydrogen production plant profit increases by 13% if hydrogen delivery distance is varied from 50 km to an interval of 10-50 km and decreases by 16% if hydrogen delivery distance is varied from 50 km to an interval of 50-100 km.

For Case 1 hydrogen production plant profit increases by 16% if hydrogen delivery distance is varied from 50 km to an interval of 10-50 km and decreases by 23% if hydrogen delivery distance is varied from 50 km to an interval of 50-100 km and for Case 2 the profit increases by 23% if hydrogen delivery distance is varied from 50 km to an interval of 10-50 km and decreases by 39% if hydrogen delivery distance is varied from 50 km to an interval of 50-100 km. Hydrogen delivery distance influence on gasification plant profit is more pronounced when hydrogen demand variation is higher.

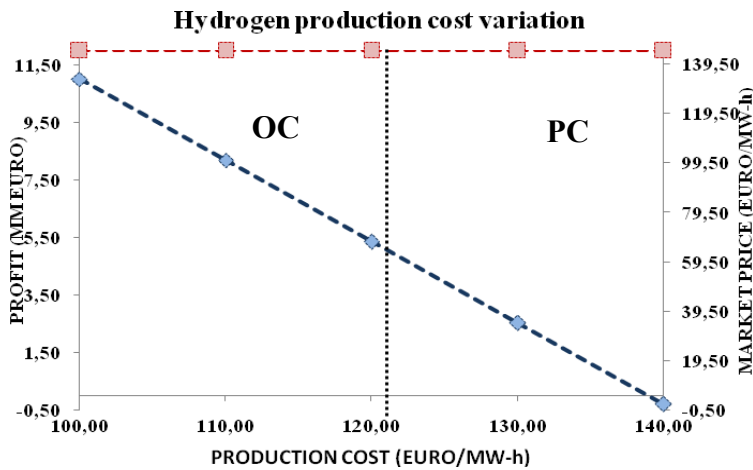


**Figure 7.** Hydrogen production cost variation  
( $H_2$  demand =  $H_2$  production rate,  $D_{hydrogen\ delivery} = 50$  km)

Figure 7 illustrates hydrogen production cost influence on gasification plant profit, for the Base case. In the Optimistic case (OC) it is assumed that hydrogen production cost decreases from 120 €/MW to 110 €/MW and 100 €/MW. In this case, the hydrogen production plant profit increases by 53%, respectively by 103%. In the Pessimistic case (PC) it is assumed that hydrogen production cost increases from 120 €/MW to 130 €/MW and 140 €/MW. Gasification plant profit decreases from 5.35 MM Euros to 2.5 MM Euros and to -0.3 MM Euros. Hydrogen market price it is assumed to be constant (145 €/MW).

## CONCLUSIONS

Hydrogen production supply chain assessment under demand variability provide a “what if” analysis and help foresee how hydrogen demand variability, hydrogen delivery distance variation and hydrogen production cost variation would affect the entire biomass gasification based hydrogen production supply chain, especially the gasification plant, during one year time frame (8000 working hours).

In order to reduce the wood chips quality degradation and dry matter losses risks over the storage period and to meet the gasification reactor requirements in terms of raw material properties a stock optimization is performed in Arena OptQuest resulting in a decrease of wood chips stock at the gasification plant and at the warehouse.

Biomass gasification based hydrogen production supply chain system is evaluated in terms of: hydrogen amount sold and hydrogen amount stored (MW-h), hydrogen lost sales amount (MW-h), partial sales per cent and gasification plant profit (MM Euros). Hydrogen demand variation result is a decrease of gasification plant profit. Also, hydrogen delivery distance influence on gasification plant profit is more pronounced when hydrogen demand variation is higher.

## ACKNOWLEDGEMENTS

The authors are thankful for the financial support provided from programs: Sectorial Operational Programme for Human Resources Development 2007-2013, co-financed by the European Social Fund, under the project number POSDRU/107/1.5/S/76841 with the title „*Modern Doctoral Studies: Internationalization and Interdisciplinarity*” and by Romanian National Authority for Scientific Research, CNCS – UEFISCDI, project number PN-II-ID-PCE-2011-3-0028: “*Innovative methods for chemical looping carbon dioxide capture applied to energy conversion processes for decarbonized energy vectors poly-generation*”.

## REFERENCES

- [1]. M. Muresan, C.C. Cormos, P.S. Agachi, *Proceedings of the 22<sup>nd</sup> European Symposium on Computer Aided Process Engineering (ESCAPE 22, London, UK, 17 - 20 June 2012), Computer Aided Chemical Engineering*, **2012**, 30, 462-466.
- [2]. M. Ball, M. Wietschel, *International Journal of Hydrogen Energy*, **2009**, 34, 615-627.

- [3]. K.K. Pant, R.B. Gupta, Hydrogen fuel: production, transport and storage, Fundamentals and Use of Hydrogen as a Fuel, *CRC Press*, Taylor & Francis Group, 6000 Broken Sound Parkway NW, Suite 300, Boca Raton, FL 33487-2742, **2009**.
- [4]. K.E. Zanganeh, A. Shafeen, *International Journal of Greenhouse Gas Control*, **2007**, 1, 47-54.
- [5]. H.Dagdougui, *International Journal of Hydrogen Energy*, **2012**, 37, 5318-5327.
- [6]. A. Bhattacharya, A.Bhattacharya, A. Datta, *International Journal of Hydrogen Energy*, **2012**, 37, 18782-18790.
- [7]. M. Muresan, C.C. Cormos, P.S. Agachi, *Chemical Engineering Research and Design*, **2013**, 91, 8, 1527-1541.
- [8]. M.B. Nikoo, N. Mahinpey, *Biomass and Bioenergy*, **2008**, 32, 1245-1254.
- [9]. J. Rezaian, N.P. Cheremisinoff, Gasification technologies, *CRC Press*, Taylor & Francis Group, 6000 Broken Sound Parkway NW, Suite 300 Boca Raton, FL 33487-2742, **2005**.
- [10]. S. Koppatz, C. Pfeifer, H. Hofbauer, *Chemical Engineering Journal*, **2011**, 175, 468-483.
- [11]. A.A. Rentizelas, A.J. Tolis, I.P. Tatsiopoulos, *Renewable and Sustainable Energy Reviews*, **2009**, 13, 887-894.
- [12]. WP 2.1 - 2.2 Case Report: Biomass CHP Plant in Güssing, Austria <http://www.biomob.eu>, April, **2013**.
- [13]. S. Gold, S. Seuring, *Journal of Cleaner Production*, **2011**, 19, 32-42.
- [14]. S. Koppatz, C. Pfeifer, R. Rauch, H. Hofbauer, T. Marquard-Moellenstedt, M.Specht, *Fuel Processing Technology*, **2009**, 90, 914-921.
- [15]. H. Hofbauer, G. Veronik, T. Fleck, R.Rauch, The FICFB gasification process, in: D.B.e.A.V. Bridgewater (Ed.), *Developments in Thermochemical Biomass conversion*, Banff, Canada, vol. 2, Blackie, Glasgow, UK, **1997**.
- [16]. H. Hofbauer, R. Rauch, G. Loeffler, S. Kaiser, E.Fercher, H.Tremmel, *12th European Conference on Biomass and Bioenergy*, Eigenverlag, Amsterdam, **2002**.
- [17]. S. Muller, J. Kotik, T. Proll, R. Rauch, H. Hofbauer, *Proceedings on Polygeneration Strategies (ICPS 11)*, **2011**, Wien, Austria.
- [18]. M. Muresan, R. Rauch, H. Hofbauer, C.C. Cormos, P.S. Agachi, *ICPS 13 - International Conference on Polygeneration Strategies*; Vienna University of Technology, Vienna, Austria; September, 3<sup>rd</sup> - 5<sup>th</sup>, **2013**.
- [19]. S.M. Aceves, G.D. Berry, J. Martinez-Frias, F.Espinosa-Loza, *International Journal of Hydrogen Energy*, **2006**, 31, 2274-2283.
- [20]. V. Ananthachar, J.J.Duffy, *Solar Energy*, **2005**, 78, 686-694.
- [21]. M. Balat, *International Journal of Hydrogen Energy*, **2008**, 33, 4013-4029.
- [22]. A. Tayfur, B. Melamed, Modelling supply chain systems. Simulation modelling and analysis with Arena, *Academic Press, Elsevier*, **2007**.
- [23]. R.G. Lemus, J.M. Martinez Duart, *International Journal of Hydrogen Energy*, **2010**, 35, 3929-3936.
- [24]. Curs BNR, <http://www.cursbnr.ro>, February, **2013**.

## DETERMINATION OF CHLORPYRIFOS IN SURFACE WATER USING SPE-DI-SPME/GC-ECD

MIRELA MICLEAN<sup>a</sup>, LĂCRIMIOARA ȘENILĂ<sup>a</sup>, OANA CADAR<sup>a</sup>,  
MARIUS ROMAN<sup>a</sup>, ERIKA LEVEI<sup>a</sup>, CLAUDIU TĂNĂSELIA<sup>a</sup>,  
ANNAMÁRIA TÖRÖK<sup>b</sup>, CORNELIA MAJDIK<sup>b</sup>

**ABSTRACT.** In this study a combined extraction method was performed for analysis of chlorpyrifos in surface water samples (Somes and Aries rivers and Tarnita Lake) collected in Cluj County, Romania, namely: solid phase extraction (SPE) and solid-phase microextraction (SPME) with direct immersion of the fiber, followed by gas chromatography – electron capture detection (GC-ECD). The target compound was detected in water samples collected from Somes and Aries rivers in concentrations exceeding the maximum admitted concentration (MAC) set by Romanian legislation, but lower than the MAC set by USEPA water quality criteria. The used method represents a very sensitive, simple and fast technique, easy to use, allowing the simultaneous sample extraction and analyte enrichment.

**Keywords:** *chlorpyrifos, SPE, SPME, GC-ECD, surface water*

### INTRODUCTION

High levels of pesticides are used every year in the production and post-production treatments of agricultural commodities. Chlorpyrifos (CPF) is one of the most frequently used organophosphorus pesticides (OPPs) in agriculture and in households. OPPs are mostly sprayed over crops or applied to soils, leading to their direct transfer from drainage of agricultural lands to other parts of surrounding environments, including ground and surface waters. Therefore, there is an increasing concern with regard to the determination of these compound [1, 2].

---

<sup>a</sup> INCDO-INOE 2000, Research Institute for Analytical Instrumentation, 67 Donath Str., 400293 Cluj-Napoca, Romania

<sup>b</sup> Babeş-Bolyai University Cluj-Napoca, Faculty of Chemistry and Chemical Engineering, Arany János 11, 400028-Cluj-Napoca, Romania

\* Corresponding author: mirela.miclean@icia.ro

Chlorpyrifos is moderately toxic and classified in Toxicity Category II for all exposure routes. According to the United States Environmental Protection Agency, exposure to CPF could result in neurotoxicity in animals and humans, decreased birth weight of babies and increased risk of lung cancer. The maximum permissible level for CPF in fresh water is 0.041 µg/L, according to the USEPA water quality criteria [3].

Due to the low concentration of chlorpyrifos in the aquatic environment, sensitive and reliable methods are required for determination. Sample preparation remains one of the main bottlenecks in chromatographic analysis [4]. Previously reported extraction / preconcentration methods included: liquid-liquid extraction [5, 6], solid-phase extraction (SPE), solid-phase microextraction (SPME), cloud point extraction (CPE), single drop microextraction (SDME), ultrasound-assisted emulsification microextraction (USAEME), vortex-assisted liquid-liquid microextraction (VALLME), dispersive liquid-liquid microextraction (DLLME) and SPE-DLLME, followed by gas chromatography-nitrogen phosphorus detection (GC-NPD), gas chromatography-mass spectrometry (GC-MS), gas chromatography-flame photometric detection (GC-FPD) and high-performance liquid chromatography (HPLC) [7]. Bonansea reported a combined extraction method: SPE with SPME, followed by GC-MS [6].

The aim of this study was to determine the content of chlorpyrifos in surface water samples (two rivers and one lake) in Cluj County, Romania using GC-ECD, subsequent to SPE/SPME combined extraction method.

## RESULTS AND DISCUSSION

The standard solutions were prepared by successive dilutions of chlorpyrifos, in methanol. External calibration was performed using 5 different concentration levels of CPF, using the same method presented before in the SPE-SPME combined extraction procedure, for the extraction of standard solutions. The linearity of calibration curve was assessed in the range of 1.0 - 20 ng/L, with 0.99904 correlation coefficient. The calibration curve is presented in Figure 1.

The detection (LOD) and quantification (LOQ) limits were evaluated according to the signal-to-noise ratio of 3 and 10 respectively, and were 0.32 ng/L and 0.95 ng/L, respectively. It is worth mentioning that the limit of quantification reported for water was 50 ng/L for water, after liquid-liquid extraction, followed by Gas Chromatography with Nitrogen-Phosphorous Detector [8], more than 50 times higher than in the method used in the present study.

DETERMINATION OF CHLORPYRIFOS IN SURFACE WATER USING SPE-DI-SPME/GC-ECD

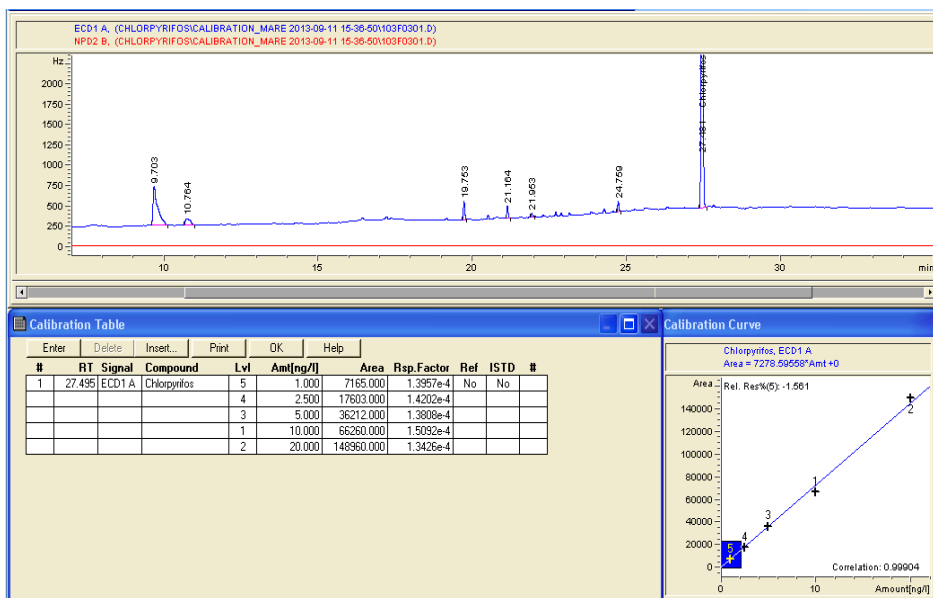


Figure 1. Calibration curve for CPF in water

The collected water samples were analysed using the above mentioned method and the obtained results are shown in Table 1. The SPE-DI-SPME/GC-ECD chromatogram of Somes river water sample is presented in Figure 2.

The presence of CPF was detected in both river water samples, with a higher value in Somes than in Aries river, possibly reflecting a combined sources of pollution for Somes water: urban and agricultural, in accordance with the findings reported by Bonansea et al. (2013) in Suquia River (Argentina), collecting the wastewater of Córdoba city [6].

Table 1. Concentration of chlorpyrifos in surface water samples

Sampling point	Chlorpyrifos
Somes River	7.2 ng/L
Aries River	4.5 ng/L
Tarnita Lake	<LOQ

The obtained concentrations of CPF exceeded the MAC value set by Romanian legislation (0.46 ng/L) [9] and also the Canadian Water Quality Guidelines established for the protection of the aquatic biota in freshwaters (3.5 ng/L) [6], for the both river water samples. These obtained concentrations

of CPF in river water samples were lower than the MAC set by USEPA water quality criteria (41 ng/L) [3] and were comparable with those reported by Bonansea et al. (2013) in Suquía River (Argentina) [6]. The concentration of CPF was lower than quantification limit in the lake water sample, indicating no use of CPF in the adjacent area.

## CONCLUSIONS

This study report the concentrations of chlorpyrifos in surface water samples: Somes River, Aries River and Tarnita Lake, collected in Cluj County, Romania. In river samples, the target compound was detected in concentrations exceeding the MAC set by Romanian legislation, but lower than the MAC set by USEPA water quality criteria. In the lake water sample, chlorpyrifos was not detected.

For the analysis of chlorpyrifos, a combined extraction method was used: SPE followed by SPME, and then GC-ECD quantitative analysis. Because the analyte is concentrated on the cartridge and then on the fiber and is rapidly delivered to the column, minimum detection limits were achieved. SPME technique is an advanced methodology for rapid determination of aroma compounds and is “environmentally friendly” due to the absence of any organic solvents involved in the analysis. The method represents a very sensitive, simple and fast technique, easy to use and permit simultaneous sample extraction and analyte enrichment.

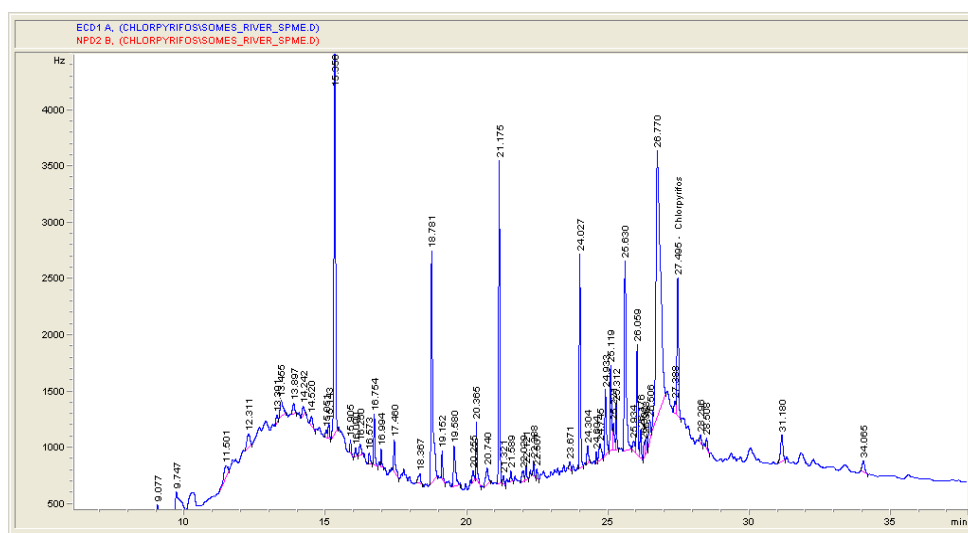


**Figure 2.** The SPE-DI-SPME/GC-ECD chromatogram of Somes river water sample

## EXPERIMENTAL SECTION

### *Study area and sampling*

In September 2013, water samples were collected from Somes River (sampling point 1), Aries River (sampling point 2) and Tarnita Lake (sampling point 3) in Cluj-County, Romania. The sample 1 was collected about 4 km downstream the municipal sewage treatment plant, which collect and filter the urban residues of Cluj-Napoca, a city with approximate 400000 inhabitants. The sample 2 was collected near Turda town and sample 3, about 30 km away of Cluj-Napoca city. The geographic coordinates of sampling points are shown in Table 2. Water samples were collected manually, by immersing the bucket under the surface of water and then by filling the precleaned amber-glass bottles. Samples were stored at 4°C until filtration and extraction.

**Table 2.** Geographic coordinates of sampling points

Sampling point	Latitude, N	Longitude, E
1	46°45'54.01"N	23°32'59.81"E
2	46°33'58.98"N	23°47'7.02"E
3	46°43'7.27"N	23°16'51.34"E

### *Materials and reagents*

All chemicals were analytical reagent grade. Chlorpyrifos (98.0%) was purchased from Sigma-Aldrich (St. Louis, MO, USA). Methanol HPLC-grade, acetone, dichloromethane and sodium chloride (NaCl, 99%) were purchased from Merck (Darmstad, Germany). Sodium chloride was used to decrease the solubility of CFP and increase the adsorption of analyte by SPME technique. Ultrapure water (18.2 MΩ cm) was prepared by a Direct Q UV 3 Millipore system (Bedford, MA, USA).

For solid phase extraction, SPE Lichrolut RP-18 (40-63 μm) cartridges were used and were purchased from Merck (Darmstad, Germany). SPE extractions were performed with the Visiprep DL Vacuum Manifold for 12 samples from Supelco Inc. (Bellefonte, PA, USA). For the SPME extraction, a manual fiber holder Supelco Inc. (Bellefonte, PA, USA) with an 85 μm polyacrylate (PA) fiber from Supelco Inc. (Bellefonte, PA, USA) were used. Before use, the fiber was conditioned in the gas chromatograph inlet for 2 h at 300°C, according to the instructions of supplier.

### *Instrumentation*

The samples were analyzed by GC (Agilent 6890, USA) equipped with electron capture detector (ECD). The column was HP-5 (0.25 mm film thickness, 30 m length, 0.25 mm i.d., J&W Scientific, USA) for chlorpyrifos determination. Helium was used as carrier gas.

### **SPE and SPME combined extraction procedure**

SPE and SPME combined extraction was performed according to the extraction reported by Bonansea et al. (2013). In short, prior to SPE extractions, the cartridges were treated with 10 mL dichloromethane, followed by 10 mL methanol and 10 mL water. Aqueous samples (1 L) were passed through cartridges, after that the cartridges were dried by vacuum, and the elution was carried out with 5 mL methanol. The eluent was evaporated to dryness under nitrogen in 10 mL SPME glass vials.

After SPE extraction, SPME extraction was carried out using the SPE extract dissolved in 7 mL water and 0.1 mL acetone and sealed with a PTFE/Silicone septum and then, it was placed in a water bath. An amount of 3 g NaCl and a magnetic stirrer bar for samples were put in a vial sealed. The extractions were performed with the immersion of the PA (Supelco) fiber in the sample for 30 min at 70°C, under constant stirrer (100 rpm). After extraction, the fiber was removed from the sample and introduced in the GC injector for 5 min at 250°C for thermal desorption.

### **ACKNOWLEDGMENTS**

This work was supported by Romanian financing authority CNCS – UEFISCDI, Capacities, Romania-China bilateral cooperation project, project number 630/01.01.2013.

### **REFERENCES**

- [1]. J. Chen, C. Duan, Y. Guan, *Journal of Chromatography B*, **2010**, 878, 1216-1225.
- [2]. X. Zhang, Y. Shen, X.Y. Yu, X.J. Liu, *Ecotoxicology and Environmental Safety*, **2012**, 78, 276-280.
- [3]. A.M.W. Menike, R. Shanthini, C.S. Kalpage, D.G.G.P. Karunaratne, A. Kankanamge, *Journal of the National Science Foundation of Sri Lanka*, **2012**, 40(4), 333-344.
- [4]. Vuckovic D., *Trends in Analytical Chemistry*, **2013**, 45, 136-153.
- [5]. A.M. Rodrigues, V. Ferreira, V.V. Cardoso, E. Ferreira, M.J. Benoliel, *Journal of Chromatography A*, **2007**, 1150, 267-278.
- [6]. R.I. Bonansea, M.V. Amé, D.A. Wunderlin, *Chemosphere*, **2013**, 90, 1860–1869.
- [7]. S. Samadi, H. Seresht, Y. Assadi, *Journal of Chromatography A*, **2012**, 1219, 61-65.
- [8]. L. Padovani, E. Capri, *Chemosphere*, **2005**, 58, 1219-1229.
- [9]. Order 161/2006. Order of Public Administration no. 161/2006, published in Official Gazzete no. 511/2006.

# APPLICATION OF MULTIWALLED CARBON NANOTUBES MODIFIED BY DIETHYL DITHIOPHOSPHATE AMMONIUM FOR SELECTIVE SOLID PHASE EXTRACTION OF ULTRA TRACES Ni(II) AND Co(II) IN RIVER WATER SAMPLES

SHAHRAM NEKOU EI<sup>a</sup>, FARZIN NEKOU EI<sup>a\*</sup>

**ABSTRACT.** In the present study, preconcentration followed by solid phase extraction of heavy metal ions, Ni(II) and Co(II) using the multiwalled carbon nanotubes (MWCNTs) and complexing reagent diethyl dithiophosphate ammonium (DDPA) were investigated and characterized by flame atomic absorption spectroscopy (FAAS). A series of experimental parameters, including sample pH, concentration of diethyldithiophosphate ammonium (DDPA), sample flow rate, eluting solution and the effect of interfering ions have been investigated systematically. The calibration graph was linear in the range of 0.4-100  $\mu\text{g L}^{-1}$  and 0.7-120 for Ni(II) and Co(II), respectively. Under optimized conditions, the limit of detections (LOD) were 0.1 and 0.2  $\mu\text{g L}^{-1}$  for Ni(II) and Co(II), respectively. The method was successfully applied to the preconcentration and separation of Ni(II) and Co(II) in some water samples from rivers located in industrial and nonindustrial areas.

**Keywords:** *Solid phase extraction; diethyl dithiophosphate ammonium (DDPA); Multiwalled carbon nanotubes; river water samples; Flame atomic absorption spectrometry, Ni(II) and Co(II)*

## 1. INTRODUCTION

Heavy metals at trace levels in environment are generally problem for human living. Industry and traffic are the main sources of traces metal ions in environment.<sup>1</sup>

The high consumption of nickel and cobalt-containing products in industry inevitably leads to environmental pollution at all stages of production, recycling and disposal. Thus, the determination of trace amounts of nickel and cobalt in biological and environmental samples is important in the fields of

---

<sup>a</sup> *Young Researchers and Elite Club, Gachsaran Branch, Islamic Azad University, Gachsaran, Iran*

\* *Corresponding author: f.nekouei@hotmail.com*

environmental analysis, process control and medicine. Toxicological effects of large amounts of cobalt include vasodilatation, flushing and cardiomyopathy in human and animals.<sup>2</sup> Nickel can cause allergic reactions and that certain nickel compounds maybe carcinogenic. The determination of cobalt and nickel in natural water samples of environmental interest in which it is found at very low concentrations requires the use of preconcentration methods coupled to atomic spectrometric methods.<sup>3</sup>

Solid-phase extraction (SPE) is one of the most employed preconcentration methods that can be applied in off-line or online systems, with the advantage of possible automatization. SPE consists of the retention of metal species (or its derivatives) on the appropriate solid sorbent packed in a column or microcolumn and the later desorption with the adequate solvent. Thus, the concentration and separation of the analyte from the rest of sample matrix is achieved.<sup>4</sup> Solid-phase extraction (SPE), owing to its flexibility, absence of emulsion, simplicity, sampling in the field, safety, and ease of automation, is a preferred method for separation and enrichment of the target. SPE requires that the adsorbent possess a stronger selective adsorption ability.<sup>5</sup>

Carbon nanotubes (CNTs) are one of the most commonly used building blocks of nanotechnology. With one hundred times the tensile strength of steel, thermal conductivity better than all but the purest diamond, and electrical conductivity similar to copper, but with the ability to carry much higher currents, they seem to be a very interesting material. CNTs have been proposed as a novel solid phase extractor for various inorganic and organic materials at trace levels.<sup>6</sup>

CNTs have become attractive materials, since its discovery in 1991, because of their novel structure characteristics.<sup>7-16</sup> Recently, Carbon nanotubes as an adsorbent for the preconcentration of traces heavy metals have become very popular.<sup>17-31</sup>

In the presented work, the analytical potential of MWCNTs as an adsorbent for the preconcentration of traces heavy metals cobalt and nickel ions using DDPA as chelating agent was investigated. The procedure, using a solid phase extraction column loaded with MWCNTs as sorbent, for the preconcentration of traces of understudy metals in water samples prior to their determination by flame atomic absorption spectrometry (FAAS).

## 2. RESULTS AND DISCUSSION

To achieve a sufficiently high efficiency of a solid phase extraction procedure, it is essential to optimize various factors containing, pH, amounts of DDPA and adsorbent, sample volume, elution conditions such as volume and concentration of eluent, flow rate of solution and matrix ions.

### 2.1. Effect of pH

The pH value plays an important role with respect to the adsorption of different ions on CNTs.<sup>32</sup> To evaluate the effect of pH on the extraction efficiency of Ni(II) and Co(II) as DDPA chelates adsorb on multiwalled carbon nanotubes, the pH of the sample solutions, were adjusted to fit in the range of 1–8. It is observable in Fig. 1, quantitative recoveries (>95%) were obtained for all studied ions at the pH range of 3.5–5.0. So, the pH 4 was selected for all subsequent studies.

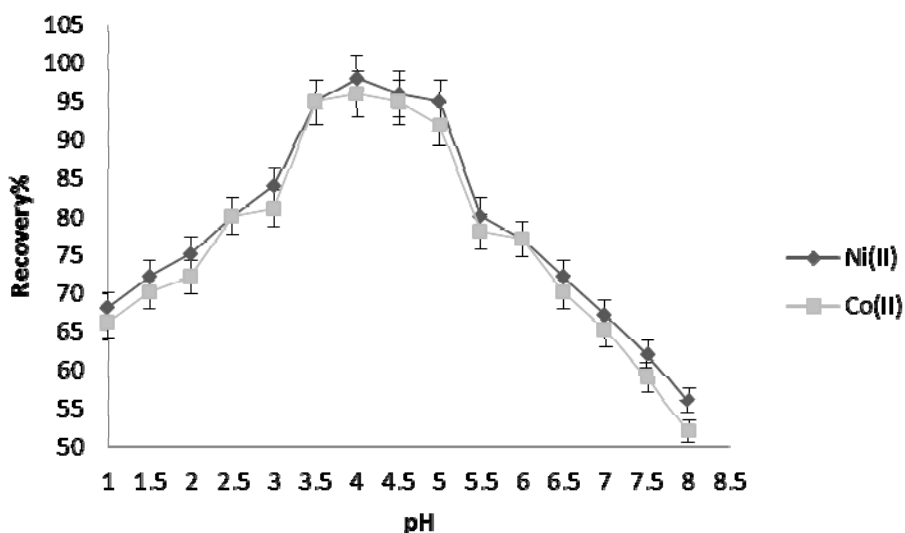


**Figure 1.** The effect of pH on the recoveries of  $1.0 \mu\text{g L}^{-1}$  Ni(II) and Co(II) ( $N=3.0$ .)

### 2.2. Effect of eluent type

The elution of the absorbed analytes could be achieved by using an appropriate eluent solution capable of effectively stripping them from the MWCNTs and bring them into the solution.<sup>33</sup> Thus, the effects of various eluents (nitric acid, hydrochloric acid and acetic acid) on the recoveries of Ni(II) and Co(II) ions from multiwalled carbon nanotubes modified with DDPA were also investigated. The results are shown in Table 1.

**Table 1.** Effect of different eluting solutions on the Recoveries of  $1\mu\text{g L}^{-1}$  Ni(II) and Co(II). (N=3)

Eluent	Recovery %	
	Ni(II)	Co(II)
1 mol L <sup>-1</sup> HNO <sub>3</sub>	86±1	84±1
1.5 mol L <sup>-1</sup> HNO <sub>3</sub>	89±3	86±2
2 mol L <sup>-1</sup> HNO <sub>3</sub>	96±2	95±4
1 mol L <sup>-1</sup> HCl	79±5	81±4
1.5 mol L <sup>-1</sup> HCl	80±2	71±1
2 mol L <sup>-1</sup> HCl	75±4	75±5
1 mol L <sup>-1</sup> CH <sub>3</sub> COOH	61±3	72±4
1.5 mol L <sup>-1</sup> CH <sub>3</sub> COOH	80±2	78±3
2 mol L <sup>-1</sup> CH <sub>3</sub> COOH	76±3	71±1

The results indicated that 2 mol L<sup>-1</sup> HNO<sub>3</sub> was sufficient for quantitative elution (>95%). Furthermore, the influence of eluent volume (2.0–10 mL) on the recoveries was studied by using 2 mol L<sup>-1</sup> HNO<sub>3</sub>. By adding 4.5 mL of 2 mol L<sup>-1</sup> HNO<sub>3</sub>, quantitative recoveries were obtained for all analyte ions. The recoveries were not quantitative for the other eluents listed in Table 1. Therefore, 4.5 mL of 2 mol L<sup>-1</sup> HNO<sub>3</sub> was used as eluent for further work.

### 2.3. Effect of amount of chelating agent

To evaluate the effect of ligand on the recovery of metal ions, different amounts of DDPA solution ( $5\times 10^{-4}$  mol L<sup>-1</sup>) in the range of 0-5 mL was investigated. As presented in Fig. 2, the recoveries of analyte ions increased with increasing amounts of DDPA added and reached a constant value over 95% with at least 2.5 mL. The recovery values of analytes were quantitative at the amounts of ligand range of 2.5- 5. Hence, 2.5 mL of ligand was selected for subsequent studies. At lower concentrations, the amount of ligand is insufficient to extract all the analyte in the solution. But at higher concentrations, all the analyte species were used, thus, Process of complex formation was stop and the percentage of recoveries remained nearly constant, in other words, the Limiting factor is analyte concentration.

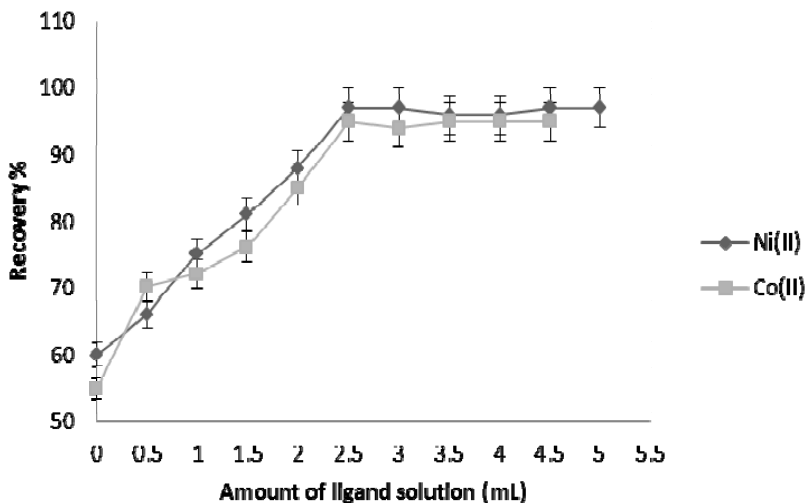


**Figure 2.** Effect of amount of ligand solution on the recoveries of analytes.

#### 2.4. Effect of amounts of adsorbent (MWCNTs)

To estimate the impact of adsorbent mass on the recovery of metal ions, different amounts of adsorbent (50–400), packed into an SPE column, were investigated, following the preconcentration procedure. The recoveries of metal ions increased with increasing amounts of adsorbent. In the less amounts than 150 mg, the resultant recoveries were low because of bypassing of the liquid in the SPE column.<sup>29</sup> Quantitative recoveries of target ions were obtained in the range of 150–300 mg. Therefore, 150 mg of MWCNTs was the amount selected for further studies.

#### 2.5. Effect of the sample volume

A higher preconcentration factor is obtainable by increasing the sample to eluent volume ratio by either decreasing the eluent volume or increasing the sample volume. Therefore, the maximum volume of sample solution was investigated by increasing the volume of metal ion solution by passing 50–600 mL of sample solutions. The effects of sample volumes on the recoveries of the two analytes are shown in Fig. 3. The results showed that the maximum sample volume could be up to 500 mL with the recovery >95%. Therefore, 500 mL of sample solution was adopted for the preconcentration of analytes from sample solutions. The preconcentration factor (PF) is calculated by the ratio of the highest sample volume (500 mL) and the lowest eluent volume (4.5 mL). The preconcentration factor was calculated as 111.0

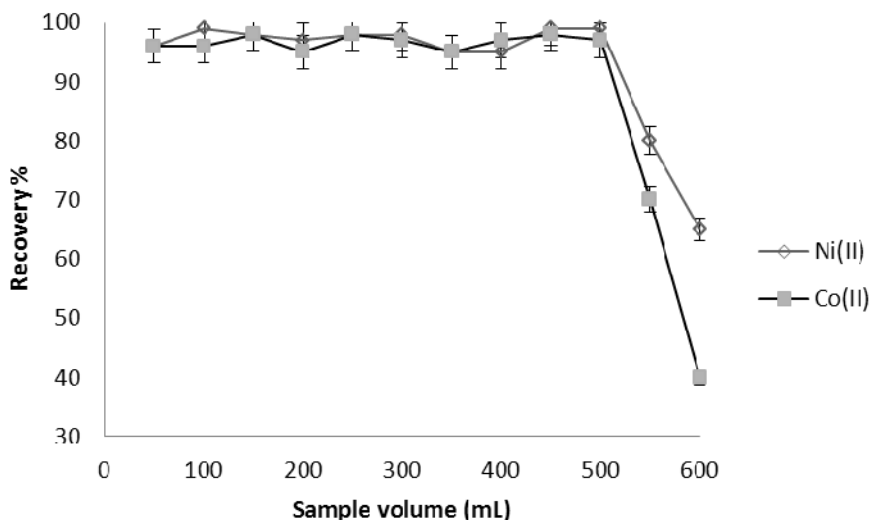


**Figure 3.** Effect of sample volume on the recoveries of  $1.0 \mu\text{g L}^{-1}$  Ni(II) and Co(II) ( $N=3.0$ )

### 2.6. Flow rates of sample and eluent solutions

The impact of flow rates of sample and eluent solutions are very important in solid phase extraction studies due to retention of analyte ions on column system. Low flow rates can be time consuming. The flow rates were investigated in the range of  $1\text{--}10 \text{ mL min}^{-1}$  and under the optimum conditions (pH and eluent type). It was found when the flow rates of the sample and eluent solutions were at the range of  $1.0\text{--}6.0$  and  $1.0\text{--}7.0 \text{ mL min}^{-1}$ , the recoveries of analytes were quantitative. At higher flow rates, there was a decrease in the recovery in that there was not sufficient contact time between MWCNTs and sample solution. Therefore, a flow rate of six milliliters per minute was chosen as the optimum flow rates of the sample and eluent solutions.

### 2.7. Effect of foreign ions

The effects of common coexisting ions on the adsorption of the analytes on MWCNTs were investigated. The obtained results were presented in Table 2. The tolerance limit is defined as the ions had no significant interferences in the preconcentration and determination of the analyses. This is due to the low adsorbing capacity or rates for interfering ions. It can be seen that the presence of major coexisting ions has no obvious influences on the determination of the analytes under the selected conditions.

**Table 2.** Effect of interfering ions on determination of  $1.0 \mu\text{g L}^{-1}$  Ni(II), and Co(II) (N= 3).

Ion	Concentration ( $\text{mg L}^{-1}$ )	Recovery (%) <sup>a</sup>	
		Ni(II)	Co(II)
Na <sup>+</sup> , Cl <sup>-</sup> , Li <sup>+</sup> I <sup>-</sup> , K <sup>+</sup> , Ca <sup>2+</sup>	10000	97±1	96±2
Mg <sup>2+</sup> , Ag <sup>+</sup> Br <sup>-</sup> , C <sub>2</sub> O <sub>4</sub> <sup>2-</sup>	8000	99±2	96±3
SO <sub>4</sub> <sup>2-</sup> , CO <sub>3</sub> <sup>2-</sup> , F <sup>-</sup>	6000	97±1	99±3
NO <sub>3</sub> <sup>-</sup> , PO <sub>4</sub> <sup>3-</sup>	3000	96±1	98±2
HCO <sub>3</sub> <sup>2-</sup> , CH <sub>3</sub> COO <sup>-</sup>	1500	99±1	97±3
Pb <sup>2+</sup> , Hg <sup>2+</sup>	500	95±3	96±3
Mo <sup>5+</sup>	250	97±1	97±2
Mn <sup>2+</sup> , Sn <sup>4+</sup>	100	99±3	97±1
Cr <sup>3+</sup> , Al <sup>3+</sup> , Cd <sup>2+</sup>	10	95±1	97±2

<sup>a</sup> Mean ± standard deviations.

## 2.8. Adsorption capacity

For investigation of the adsorption capacity of multiwalled carbon nanotubes, 0.1 g MWCNTs was added to 50 ml of solution containing 1.0 mg of metal ions at pH 4.0. After shaking for 30 min, the mixture was filtered. Ten milliliters of the supernatant solution was diluted to 100 ml and determined by flame atomic absorption spectrometry. This procedure was repeated for each analyte ions separately. The capacity of modified MWCNTs for Ni(II), and Co(II) were found to be 76.1 and 70.5  $\text{mg g}^{-1}$ , respectively.

## 2.9. Analytical performance

Using the optimized experimental conditions, calibration curves of enrichment process were linear in the range of  $0.4\text{--}100 \mu\text{g L}^{-1}$  and  $0.7\text{--}120$  for Ni(II), and Co(II), respectively. The detection limits, based on three times of the standard deviation of 10 runs of blank solution, were found to be 0.1 and 0.2  $\mu\text{g L}^{-1}$  for Ni(II), and Co(II), respectively. The relative standard deviation (RSD), twelve determinations of  $1.0 \mu\text{g L}^{-1}$  of Ni(II), and Co(II) were 4.0 and 2.6%, respectively (N=12). The correlation coefficients for Ni(II), and Co(II) were 0.9997, 0.9995, respectively. The preconcentration factor for the proposed method was 111.0.

### 2.10. Analytical applications

The solid phase extraction procedure was also applied to the determination of Ni(II), and Co(II) in water samples from rivers located in industrial and nonindustrial areas. Various amounts of analytes were also spiked to these water samples. The results are given in Table 3. A good agreement was obtained between the added and measured Ni(II), and Co(II) amounts. The accuracy of the method was verified by the analysis of samples spiked with known amounts of the analytes.

**Table 3.** The results for determination of Ni(II) and Co(II) in various river water samples.

Sample	Added ( $\mu\text{g L}^{-1}$ )		Found <sup>a</sup> ( $\mu\text{g L}^{-1}$ )		Recovery (%)	
	Ni(II)	Co(II)	Ni(II)	Co(II)	Ni(II)	Co(II)
River	-	-	80.14	43.12	-	-
Water <sup>b</sup>	100	100	181.4	140.40	100.7	98.1
	200	200	280.4	238.30	100.09	98.02
River	-	-	78.45	36.12	-	-
Water <sup>c</sup>	100	100	172.15	140.30	96.47	103.07
	200	200	273.74	235.63	98.30	99.8
River	-	-	65.8	31.57	-	-
Water <sup>d</sup>	100	100	167.11	127.74	100.79	97.08
	200	200	261.8	239.13	98.50	103.26
River	-	-	8.85	3.97	-	-
Water <sup>e</sup>	100	100	108.99	107.16	100.13	103.06
	200	200	201.01	203.24	96.25	99.64

<sup>a</sup>  $\bar{x} \pm ts\sqrt{\frac{s}{n}}$  at 95% confidence (N = 5)

<sup>b</sup> From karoon river, located in an industrial area

<sup>c</sup> From zayande rood river, located in an industrial area

<sup>d</sup> From khour musa, located in an industrial area

<sup>e</sup> From pole zohre located in an nonindustrial area

## 4. CONCLUSIONS

In this work, MWCNTs were successfully modified with DDPA and applied as enrichment material for SPE coupled with FAAS for determination of Ni(II) and Co(II). High sensitivity and selectivity, and also the good detection limits and high preconcentration factor (PF=111.0) are from the advantages of the work. The proposed method was proved to be simple, rapid and reliable and could be used for studied metal ions determination in environmental

samples. The high accuracy of the proposed method was confirmed by recovery test with standard addition method. The possible interference of some important ions was investigated and no important interference was encountered. The MWCNTs has great potential as an adsorbent for the preconcentration and determination of trace/ultra-trace metal ions in complex samples.

### 3. EXPERIMENTAL

#### 3.1. Apparatus

A Metrohm pH-meter (model 691, Switzerland) was used in order to adjust the pH at desirable values. A Chemtech Analytical Instrument model CTA-3000 atomic absorption spectrometer (Bedford, England) equipped with a flame burner was used for analysis of the understudy metals, including lamp currents and wavelength were those recommended by the manufacturer. All metals were measured under optimized operating conditions by FAAS with an air-acetylene flame.

#### 3.2. Standard solutions and reagents

Ultrapure water was used throughout the work. All chemicals were of analytical reagent grade. All the plastic and glassware were cleaned by soaking in 10% HNO<sub>3</sub> solution and then rinsed with distilled water prior to use. Standard solutions (1000 mg l<sup>-1</sup>) of Co(II) and Ni(II) ions were prepared from high purity compounds, supplied by E. Merck (Darmstadt, Germany). The working standard solutions were prepared by diluting stock standard solution. A 5×10<sup>-4</sup> mol l<sup>-1</sup> solution of DDPA reagent was prepared by dissolving an appropriate amount of DDPA in 10 mL ethanol and diluting to 100 mL in a volumetric flask. McIlvaine's buffer solution in the pH range of 1-8 was used to adjust pH values and made by mixing 0.2 mol l<sup>-1</sup> phosphoric acid and 0.1 mol l<sup>-1</sup> Acetic acid. Multiwalled carbon nanotube was purchased from Aldrich, (Germany). The BET (Brunauer-Emmett-Teller) surface area and density of nanotubes were 300 m<sup>2</sup> g<sup>-1</sup> and 2.1 g mL<sup>-1</sup>, respectively.

#### 3.3. Preparation of the column

150 mg of Multiwalled nanotube was packed into a glass column, 120 mm in length and 20 mm in diameter, and blocked by small portion of glass wool at the both ends to prevent loss of the adsorbent. In order to clean the column, prior to use, 1.5 mol l<sup>-1</sup> HNO<sub>3</sub> solution and water were passed through the column to clean it. Then, the column was conditioned to the desired pH values with McIlvaine's buffer solution. The column was conditioned with distilled water during the passing time for the next experiments.

### 3.4. Recommended procedure

A standard solution containing 0.4-100  $\mu\text{g L}^{-1}$  of Ni(II) and 0.7-120  $\mu\text{g L}^{-1}$  of Co(II) and the pH value was adjusted to the desired value with McIlvaine's buffer solution. Then DDPA was added to form the metal DDPA chelates and the solutions were passed through the column gravitationally. The metal ions retained on the column were eluted with desired volume and concentration of nitric acid solution and determined by FAAS.

### 3.5. Sample preparations

The river water samples were collected from the rivers located in industrial and nonindustrial areas. The water samples were filtered through a 0.45  $\mu\text{m}$  PTFE Millipore filter. After adjusting to the desired pH values, the solutions were passed through the column gravitationally.

## ACKNOWLEDGEMENT

The authors state their gratitude to Young Researchers and Elite Club, Gachsaran Branch, Islamic Azad University, Gachsaran, Iran, for financial support of this work (Grant 1392).

## REFERENCES

- [1]. M. Soylak, Y.M. Unsal, *Food. Chem. Toxicol.*, **2010**, *48*, 1511-1515.
- [2]. A. Safavi, B.H. Abdollahi, M.R. Hormozi Nezhad, R. Kamali, *Spectrochim. Acta. A*, **2004**, *60*, 2897.
- [3]. J. Chen, Kh. Ch.Teo, *Anal. Chim. Acta*, **2001**, *434*, 325.
- [4]. C.H. Latorre, J.A. Méndez, J.B. García, S.G. Martín, R.M.P. Crecente, *Anal. Chim. Acta*, **2012**, *749*, 16.
- [5]. L. Xi, Zh. Zhao-Hui, Zh. Hua-Bin, H. Yu-Fang, Y. Xiao, N. Li-Hua, *Chin. J. Anal. Chem.*, **2011**, *39*, 839.
- [6]. M. Tuzen, K.O. Saygi, C. Usta, M. Soylak, *Biores. Technol.*, **2008**, *99*, 1563.
- [7]. S. Iijama, *Nature*, **1991**, *354*, 56.
- [8]. S. Iijama, T. Ichihashi, *Nature*, **1993**, *363*, 603.
- [9]. C. Pan, S. Xu, H. Zou, Zh. Guo, Y. Zhang, B. Guo, *J. Am. Soc. Mass. Spectrom.*, **2005**, *16*, 263.
- [10]. N. Pourreza, K. Sheikhnajdi, *Talanta*, **2012**, *99*, 507.
- [11]. Y. Liu, Y. Li, Zh. Q. Wu, X. P. Yan, *Talanta*, **2009**, *79*, 1464.
- [12]. N. Rastkari, R. Ahmadkhaniha, *J. Chromatogr. A*, **2013**, *1286*, 22.
- [13]. A. Duran, M. Tuzen, M. Soylak, *J. Hazard. Mater.*, **2009**, *169*, 466.

- [14]. J. Li, Q. Su, K.Y. Li, Ch.F. Sun, W.B. Zhang, *Food. Chem.*, **2013**, *141*, 3714.
- [15]. E. Zakharchenko, O. Mokhodoeva, D. Malikov, N. Molochnikova, Y. Kulyako, G. Myasoedova, *Proc. Chem.*, **2012**, *7*, 268.
- [16]. L. Guo, H.K. Lee, *J. Chromatogr. A*, **2011**, *1218*, 9321.
- [17]. Zh. Zang, Zh. Hu, Zh. Li, Q. He, X. Chang, *J. Hazard. Mater.*, **2009**, *172*, 958.
- [18]. X.Y. Song, Y.P. Shi, J. Chen, *Talanta*, **2013**, *116*, 188.
- [19]. Y.S. Al-Degs, M.A. Al-Ghouti, A.H. El-Sheikh, *J. Hazard. Mater.*, **2009**, *169*, 128.
- [20]. M.A. Ghanem, I. Kocak, A. Al-Mayouf, Ph. N. Bartlett, *Electrochem. Commun.*, **2013**, *34*, 258.
- [21]. Y. Liu, Sh. Yang, W. Niu, *Colloids. Surf. B. Biointer*, **2013**, *108*, 266.
- [22]. X.Y. Song, Y.P. Shi, J. Chen, *Food. Chem.*, **2013**, *139*, 246.
- [23]. Y. Wang, J. Xie, Y. Wu, X. Hu, C. Yang, Q. Xu, *Talanta*, **2013**, *112*, 123.
- [24]. M. Moazzen, R. Ahmadkhaniha, M. Es'haghi Gorji, M. Yunesian, N. Rastkari, *Talanta*, **2013**, *115*, 957.
- [25]. Sh.K. Wadhwa, M. Tuzen, K. Gul Kazi, M. Soylak, *Talanta*, **2013**, *116*, 205.
- [26]. P. Kueseng, J. Pawliszyn, *J. Chromatogr. A*, **2013**, *1317*, 199.
- [27]. B. Dai, M. Cao, G. Fang, B. Liu, X. Dong, M. Pan, Sh. Wang, *J. Hazard. Mater.*, **2012**, *219-220*, 103.
- [28]. X. Liu, X. Wang, F. Tan, H. Zhao, X. Quan, J. Chen, L. Li, *Anal. Chim. Acta*, **2012**, *727*, 26.
- [29]. X. Chen, Zh. Zhang, X. Yang, J. Li, Y. Liu, H. Chen, W. Rao, Sh. Yao, *Talanta*, **2012**, *99*, 959.
- [30]. M. Savio, B. Parodi, L.D. Martinez, P. Smichowski, R.A. Gil, *Talanta*, **2011**, *85*, 245.
- [31]. M. Tuzen, K.O. Saygi, M. Soylak, *J. Hazard. Mater.*, **2008**, *152*, 632.
- [32]. H.D. Liang, D.M. Han, *Anal. Lett.*, **2006**, *39*, 2285.
- [33]. A.H. El-Sheikh, J.A. Sweileh, Y.S. Al-Degs, *Anal. Chim. Acta*, **2007**, *604*, 119.



## CORROSION INHIBITION OF ALUMINIUM BY CYCLOHEXYLAMINE DITHIOCARBAMATE IN ACIDIC SOLUTION

EHAB ALSHAMAILEH<sup>a,\*</sup>, MOHAMMAD H. KAILANI<sup>a</sup>,  
SHARIF ARAR<sup>a</sup>, AIMAN E. AL-RAWAJFEH<sup>b</sup>

**ABSTRACT.** The role of cyclohexylamine dithiocarbamate (CHDTC) in the corrosion inhibition of aluminium in 1 M HCl solution is investigated by weight loss, potentiodynamic polarization, electrochemical impedance spectroscopy, and scanning electron microscopy techniques. The results suggest that CHDTC is a good inhibitor with mixed-type character for aluminium in acidic solution. Both anodic and cathodic processes on the metal surface are hindered and there is a direct relationship between the concentration of CHDTC and the inhibition efficiency. The inhibition mechanism involves the adsorption of CHDTC on the metal surface as seen from the equivalent circuit analysis of the EIS results. Weight loss experiments are carried out with aluminium samples in 1 M HCl solution at room temperature and the same trend of inhibition is produced. Scanning electron microscopy (SEM) is used to image the surface at the different stages of the corrosion inhibition processes. Adsorption of CHDTC molecules onto the aluminium surface can be concluded as a function of concentration.

**Keywords:** Aluminium, corrosion inhibition, cyclohexylamine dithiocarbamate, acidic solution, weight loss, polarization, EIS, SEM

### INTRODUCTION

Among non-ferrous metals, aluminium is the most widely used metal with the largest total production. It enters a large number of applications as a pure metal or alloyed [1]. Aluminium has valuable electrical industrial applications due to its negative value of standard electrode potential [2].

---

<sup>a</sup> Department of Chemistry, Faculty of Science, The University of Jordan, Amman 11942, Jordan

<sup>b</sup> Department of Chemical Engineering, Tafila Technical University, Tafila, Jordan

\* Corresponding author: ehab@ju.edu.jo; ehabju2@gmail.com

The literature is abundant with research studies on the corrosion behavior of aluminium and its alloys in aqueous acidic solutions [3-11]. The corrosion inhibition of aluminium involves the strong adsorption of inhibitor molecules on the metal surface and ultimately suppressing the cathodic and anodic processes.

Dithiocarbamate derivatives have been extensively studied due to their antimicrobial activity and the various applications in industrial and chemical processes, such as vulcanization accelerators, flotation agents, fungicides, pesticides, and corrosion inhibitors. One of the most interesting properties of dithiocarbamates is their strong metal-binding ability and the ease to form self-assembled monolayers (SAMs) on metallic surfaces making them useful to many applications including corrosion inhibitors [12].

There has been a good number of research articles employing green or biocompatible corrosion inhibitors as a safe alternative [13,14]. Dithiocarbamates are considered as safe biocompatible compounds.

In this paper, the synthesized compound cyclohexylamine dithiocarbamate (CHDTC) is tested as a corrosion inhibitor for aluminium in 1 M HCl aqueous solution using weight loss, polarization, electrochemical impedance spectroscopy (EIS), and scanning electron microscopy (SEM) techniques. The obtained results showed that dithiocarbamate could serve as an effective corrosion inhibitor. For organic compounds, it is well established that corrosion inhibition occurs via adsorption of their molecules on the metal surface. The efficiency of inhibition depends on multiple factors including the chemical characteristics of the adsorbed layers.

## RESULTS AND DISCUSSION

### Weight loss measurements

Table 1 shows the results of the weight loss experiments. It is evident that CHDTC inhibits the corrosion rate of aluminum in 1 M HCl and the inhibition efficiency increases with increasing the inhibitor concentration. We can see that the optimum inhibition efficiency was achieved around  $2 \times 10^{-3}$  M and a further increase in the inhibitor concentration did not improve the inhibition efficiency. This may be attributed to adsorption saturation of the inhibitor on the metal surface. The effect of varying the immersion time in the inhibitor and temperature of solution on the inhibition efficiency was studied for selected concentrations but no apparent effect was noticed. However, all experiments were carried out at 25 °C using a water bath.

**Table 1.** Percent inhibition of CHDTC from weight loss experiments of Al in 1 M HCl. Time of immersion is 24 h. for all samples. The surface area was approximately  $9.6 \text{ cm}^2$

Sample no.	CHDTC concentration M	Mass before g	Mass after g	Mass change g	Corrosion Rate ( $\text{mg/h.cm}^2$ )	Inhibition Efficiency %
0	0	2.1063	1.9906	0.1157	0.50217	
1	$2.0 \times 10^{-6}$	2.1245	2.0584	0.0661	0.28689	42.9
2	$8.0 \times 10^{-6}$	2.1220	2.0620	0.0600	0.26042	48.1
3	$3.0 \times 10^{-5}$	2.1038	2.0532	0.0506	0.21962	56.3
4	$1.0 \times 10^{-4}$	2.1271	2.0779	0.0492	0.21354	57.5
5	$2.0 \times 10^{-3}$	2.1130	2.0720	0.0410	0.17795	64.6
6	$8.0 \times 10^{-3}$	2.1183	2.0755	0.0428	0.18576	63.0

### Polarization measurements

Potentiodynamic polarization curves of aluminium in 1 M HCl solution without and with different concentrations of the inhibitor CHDTC are shown in Figure 1. It is observed that both the cathodic and anodic processes are hindered upon the addition of CHDTC. The polarization curves were recorded for inhibitor concentrations ranging between  $2 \times 10^{-6}$  and  $8 \times 10^{-3}$  M at around  $25 \text{ }^\circ\text{C}$ . The electrochemical parameters such as corrosion current density ( $I_{\text{corr}}$ ), corrosion potential ( $E_{\text{corr}}$ ), Tafel constants,  $b_a$  and  $b_c$ , and % inhibition efficiency were calculated from Tafel plots (Table 2). It is observed that the presence of the inhibitor lowers the corrosion current density and reaches a minimum value at the highest inhibitor concentration. It is also observed that  $E_{\text{corr}}$  values and the Tafel constants  $b_a$  and  $b_c$  do not change significantly as a function of the inhibitor concentration indicating that CHDTC behaves as a mixed type inhibitor.

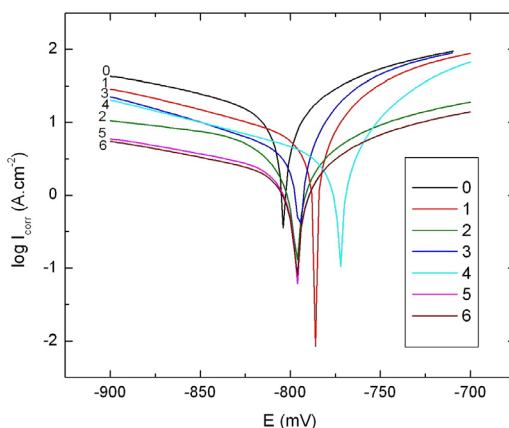


**Figure 1.** Polarization curves for the corrosion of aluminium in 1 M HCl in the absence and presence of different concentrations of CHDTC in M as listed in Table 1 (first two columns). Scan rate: 10 mV/s.

**Table 2.** Electrochemical corrosion parameters of Al in 1M HCl without and with different concentrations of CHDTC

Curve no. (Figure 1)	CHDTC Concentration M	$i_{corr}$ $\mu\text{A cm}^{-2}$	Corrosion Rate mm/Year	Inhibition Efficiency % (using $i_{corr}$ )	Inhibition Efficiency % (using Corrosion Rate)
0	0	14.3	167.0		
1	$2.0 \times 10^{-6}$	6.2	72.7	56.6	56.5
2	$8.0 \times 10^{-6}$	5.4	63.7	62.0	61.9
3	$3.0 \times 10^{-5}$	4.1	48.4	71.4	71.0
4	$1.0 \times 10^{-4}$	3.3	39.0	76.9	76.7
5	$2.0 \times 10^{-3}$	2.1	25.1	85.0	84.9
6	$8.0 \times 10^{-3}$	1.9	21.8	86.9	86.9

### Electrochemical impedance spectroscopy

The Electrochemical impedance measurements (Nyquist plots) were obtained for the different aluminium samples at the open-circuit potential after immersion in various concentrations of the inhibitor for 30 minutes. The impedance diagrams were then recorded for aluminium in 1 M HCl and are shown in Figure 2. The experimental data were fitted using the equivalent circuit shown in Figure 3 from which the circuit parameters were evaluated.

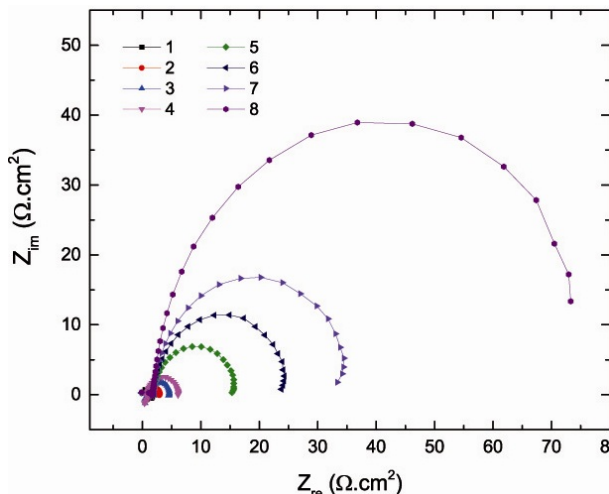


**Figure 2.** Nyquist plots of the EIS measurements for pure aluminium in 1.0 M HCl solution after immersion of the aluminium samples in different molar concentrations of the inhibitor 1) 0, 2)  $2.0 \times 10^{-6}$ , 3)  $8.0 \times 10^{-6}$ , 4)  $3.0 \times 10^{-5}$ , 5)  $1.0 \times 10^{-4}$ , 6)  $5.0 \times 10^{-4}$ , 7)  $2.0 \times 10^{-3}$  and 8)  $8.0 \times 10^{-3}$ .

The values of the electrochemical parameters:  $R_s$ ,  $C_{DL}$ ,  $R_{CT}$  and the calculated percent inhibition efficiency (%IE) are listed in Table 3. We noticed that the values of  $R_{CT}$  and the IE% increase with increasing the inhibitor concentration. However, the values of  $C_{DL}$  decreased upon increasing the inhibitor concentration. The decreasing trend in  $C_{DL}$  is due to the adsorption of the inhibitor on the surface of aluminium. The impedance curves consist of one single capacitive loop indicating that the corrosion of aluminium is primarily dominated by charge transfer. The shapes of the impedance curves are similar indicating that the corrosion mechanism is similar in all the samples. The diameter of the capacitive loop in the presence of inhibitor are always larger than that in blank solution, and extends as a function of the inhibitor concentration. This indicates that the impedance of inhibited metal is directly proportional to the inhibitor concentration.

**Table 3.** Electrochemical impedance parameters evaluated for the aluminium electrode in 1 M HCl after immersion in various inhibitor concentrations using the equivalent circuit in Figure 3

Concentration of inhibitor (M)	$R_s$ Ohm.cm <sup>2</sup>	$C_{DL}$ mF/cm <sup>2</sup>	$R_{CT}$ Ohm.cm <sup>2</sup>	IE%
0	1.31	131	0.97	
$2.0 \times 10^{-6}$	1.11	89	1.91	49.2
$8.0 \times 10^{-6}$	1.17	92	2.19	55.7
$3.0 \times 10^{-5}$	0.871	48	5.26	81.6
$1.0 \times 10^{-4}$	1.87	56	14.2	93.2
$5.0 \times 10^{-4}$	1.92	44	22.9	95.8
$2.0 \times 10^{-3}$	1.94	48	33.5	97.1
$8.0 \times 10^{-3}$	2.16	34	75.0	98.7

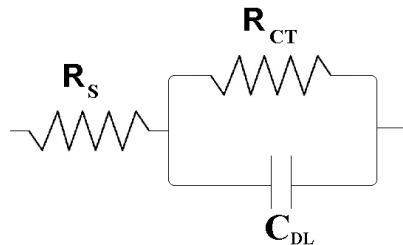


**Figure 3.** The equivalent circuit for the metal-solution interface used to model the EIS data for Al in 1 M HCl solution.

### Scanning Electron Microscopy (SEM) surface analysis

To provide a closer look at the surface modifications and hence establish a link between the surface morphology and the corrosion mechanism, scanning electron micrographs were taken for aluminium samples immersed in 0.1 M HCl for 60 minutes. Prior to that the samples were immersed in different concentrations of the inhibitor CHDTC for 30 minutes. The longer immersion times were needed to cause noticeable difference in the SEM images. The image in Figure 4a is for aluminium in the corrosive medium without the inhibitor (HCl only). Figure 4(b-d) are for aluminium in the corrosive medium pretreated with an inhibitor concentration of  $2.0 \times 10^{-6}$ ,  $1.0 \times 10^{-4}$ , and  $8.0 \times 10^{-3}$ , respectively. It is clear that the absence of the inhibitor increases the roughness of the surface of aluminium upon immersion in HCl solution (Figure 4a). The molecules of CHDTC adsorb to the surface as a function of concentration making a protective layer that decreases the rate of corrosion of aluminium (Figure 4b-4d).

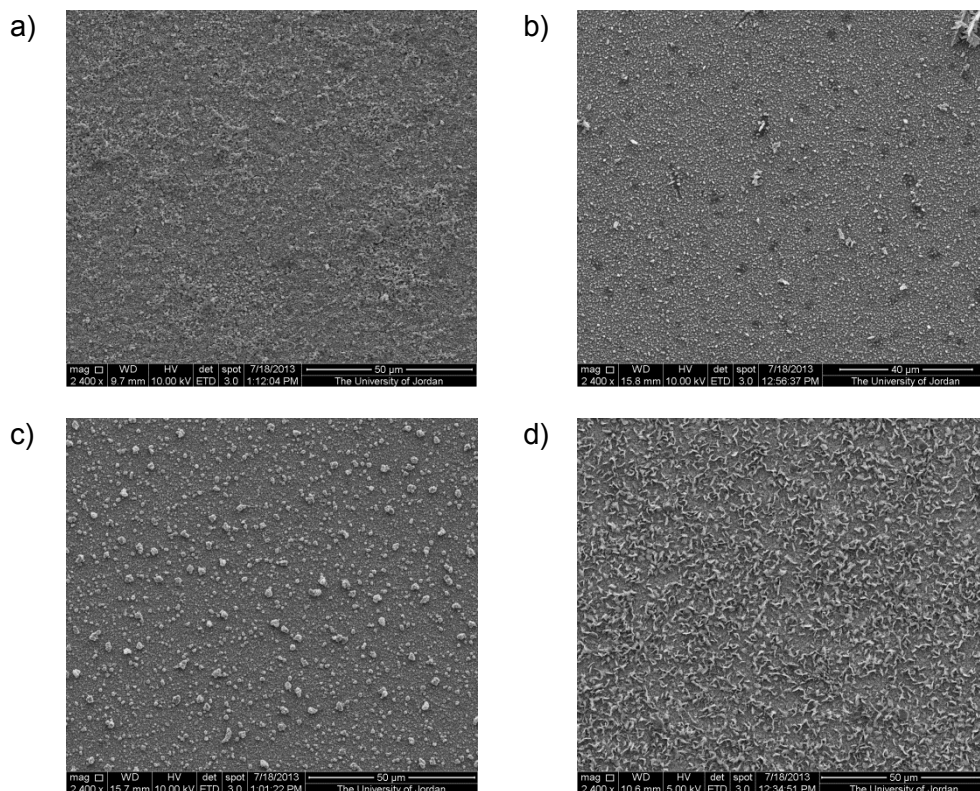


**Figure 4.** SEM images (x2400) of aluminium surface after immersion in 0.1 M HCl for 60 minutes pretreated (for 30 minutes) with CHDTC of concentrations (M): a) 0, b)  $2.0 \times 10^{-6}$ , c)  $1.0 \times 10^{-4}$  and d)  $8.0 \times 10^{-3}$ .

## CONCLUSIONS

Cyclohexylamine dithiocarbamate, CHDTC, showed reasonable corrosion inhibiting behavior for aluminium in 1 M HCl. In weight loss studies, the %IE of the CHDTC increases with increasing the inhibitor concentration. Polarization measurements suggest that CHDTC behave as a mixed-type inhibitor for aluminium in 1 M HCl. The electrochemical impedance study shows that the application of CHDTC as an inhibitor increases  $R_{CT}$  values and decreases  $C_{DL}$  values in 1 M HCl, suggesting that corrosion inhibition is governed by surface adsorption. This finding is also supported by SEM images. The different techniques used to in this study showed the same trend in corrosion inhibition with differences in %IE absolute values due to the individual technique parameters and sensitivity.

## EXPERIMENTAL SECTION

Cyclohexylamine was purchased from Aldrich (99%), sodium hydroxide, NaOH (Aldrich), carbon disulfide,  $CS_2$  (97%) and ethanol, absolute (99%), sulfuric acid,  $H_2SO_4$  (98%), potassium ferrocyanide,  $K_3Fe(CN)_6$  (99.0%), potassium chloride, KCl (99.9%), Hydrochloric acid, HCl (98%) and ammonium peroxydisulfate,  $(NH_4)_2S_2O_8$  (99%) were all of analytical grade and used as received. The sodium salt of cyclohexyl dithiocarbamate (CHDTC) was synthesized as reported in the literature with modification [3].

Aluminium samples of size 2 cm x 2 cm x 0.2 cm were cut to be used for weight loss measurements. For potentiodynamic polarization studies, the exposed area of the aluminium surface was adjusted to be 1 cm<sup>2</sup>. Electrodes were polished with emery papers of fine grade and degreased with acetone and rinsed with distilled water. Distilled water was used to prepare all solutions of 1 M HCl.

For the weight loss measurements, aluminium samples were polished, cleaned and dried in a stream of nitrogen then weighed accurately. Each of the samples was then fully immersed in a 50 mL beaker containing 1 M HCl and a different concentration of the inhibitor, CHDTC. The solutions were kept in a water bath set at room temperature. The aluminium samples were removed after 6 hours of immersion, washed with distilled water, dried, and weighed. At least three aluminium samples were used to produce an average value for the weight loss.

Electrochemical experiments were carried out with a VoltaLab PGZ 100 potentiostat in a double-wall three-electrode glass cell. Prior to measurements, the surface of the working electrode (Al) was carefully polished with alumina slurry, rinsed several times with distilled water, and then sonicated for about 1 minute. All reported potential values are versus the saturated calomel

electrode (SCE) as a reference electrode and all measurements were carried out at room temperature. A platinum wire was used as the auxiliary electrode. Solutions' pH values were measured with a Hanna calibrated digital pH meter (Switzerland). All glassware for electrochemical experiments were carefully cleaned by immersion in a solution of concentrated sulfuric acid containing ammonium peroxydisulfate  $(\text{NH}_4)_2\text{S}_2\text{O}_8$  for overnight followed by copious rinsing with distilled water.

Aluminium samples were immersed in the test solution for a few minutes until a steady open-circuit potential (OCP) was attained. The polarization curves were measured from a cathodic potential of -100 mV to an anodic potential of +100 mV with respect to the open circuit potential (OCP) at a scan rate of 10 mV/s. The generated Tafel plots were analyzed by extrapolation to evaluate the corrosion potential ( $E_{\text{corr}}$ ) and the corrosion current densities ( $I_{\text{corr}}$ ). Several measurements were carried out for each experiment to ensure the reproducibility of data. EIS measurements were carried out in the 10 Hz - 100 kHz frequency range at OCP for the aluminium electrode at different CHDTC concentrations in a thermostated cell set at room temperature. There was 10 points per decade in all measurements and the AC sine wave amplitude was 10 mV. The surface of the aluminium samples immersed in 0.1 M HCl solution with and without the adsorption of CHDTC were analyzed using Inspect F50/FEG scanning electron microscope (FEI, The Netherlands) at an accelerating voltage of 5–10 kV.

## ACKNOWLEDGMENTS

The authors thank the Faculty of Scientific Research at the University of Jordan for their financial support (Project No. 1365). Mr Waddah F. Mahmoud from the department of geology at the University of Jordan is acknowledged for taking the SEM micrographs.

## REFERENCES

- [1]. W.B. Frank, W.E. Haupin, H. Vogt, M. Bruno, J. Thonstad, R.K. Dawless, H. Kvande, O.A. Taiwo, "Aluminum. Ullmann's Encyclopedia of Industrial Chemistry", Wiley-VCH, Germany, **2009**.
- [2]. Y. Hamona, et al., *Journal of Power Sources*, **2001**, 97, 185.
- [3]. A.Y. Musa, A.A.H. Kadhum, A.B. Mohamad, M.S. Takrif, and E.P. Chee, *Current Applied Physics*, **2012**, 12(1), 323.
- [4]. S.A. Umoren and M.M. Solomon, *The Arabian Journal of Science and Engineering*, **2009**, 35(2A), 115.

- [5]. A.A. El-Maghraby, *The Open Corrosion Journal*, **2009**, 2, 189.
- [6]. A.Y. El-Etre, *Corrosion Science*, **2003**, 45(11), 2485.
- [7]. M. Abdallah, *Corrosion Science*, **2004**, 46(8), 1981.
- [8]. S.A. Umoren, I.B. Obot, E.E. Ebenso, P.C. Okafor, O. Ogbobe, and E.E. Oguzie, *Anti-Corrosion Methods and Materials*, **2006**, 53(5), 277.
- [9]. L.A. Nnanna, I.U. Anozie, A.G.I. Avoaja, C.S. Akoma, and E.P. Eti, *African Journal of Pure & Applied Chemistry*, **2011**, 5(8), 265.
- [10]. I.B. Obot and N.O. Obi-Egbedi, *Journal of Applied Electrochemistry*, **2010**, 40, 1977.
- [11]. E.E. Oguzie, *Corrosion Science*, **2007**, 49(3), 1527.
- [12]. E. AlShamaileh, H. Saadeh, V. Favry, *Journal of Chemistry*, **2013**, doi: 10.1155/2013/383921.
- [13]. K. Devarayan, G. Mayakrishnan, S. Nagarajan, *Chemical Science Review and Letters*, **2012**, 1, 1.
- [14]. H.H. Huang, T-K. Yeh, J-C. Kuo, C-J. Wang, W-T. Tsai, *Corrosion Engineering, Science and Technology*, **2014**, 49(2), 81.



## STUDIES ON OBTAINING IONIC THERMOPLASTIC ELASTOMERS BASED ON MALEINIZED STYRENE-BUTADIENE BLOCK-COPOLYMERS

MARIA DANIELA STELESCU<sup>a</sup>

**ABSTRACT.** This article presents the process of obtaining ionic thermoplastic elastomers based on maleinized styrene-butadiene block-copolymers (SBS-g-AM) by melt mixing. The following were studied influence of the amount of maleic anhydride, mixing time and degree of neutralization on physico-mechanical properties of blends based on SBS-g-AM rubber.

**Keywords:** *styrene-butadiene block copolymer, maleic anhydride, ionic thermoplastic elastomers, physico-mechanical properties*

### INTRODUCTION

Styrene copolymers with diolefins such as: styrene-co-butadiene, random (SBR) and block (SBS) deserve similar industrial interest in the field of elastomers and thermoplastic elastomers and have been subjected to studies aimed at introducing functional groups, allowing a better interaction particularly with other polymers and inorganic fillers [1-2]. This can be done by modification of conventional polymers by grafting and graft-(co) polymerization techniques. Several researchers [3-7] have documented graft copolymerization reactions initiated by chemical treatment, photo-irradiation, high-energy radiation technique, etc. as a versatile means to modify polymers.

Maleic anhydride (AM) is a strong hydrophilic monomer. If it is grafted onto polymers they will carry a denser distribution of carbonyl or free carboxylic groups. These reactive groups can also serve as sites for further macromolecular reactions of copolymers and grafted polymers, especially for compatibilization of immiscible polymers and preparation of various reactive blends with higher engineering performance and controlled morphology and

---

<sup>a</sup> National Research and Development Institute for Textile and Leather – Leather and Footwear Research Institute, Ion Minulescu Street, 93, Bucharest, Romania, dmstelescu@yahoo.com

mechanical properties [8-9]. In the last decade, grafting of AM onto various thermoplastic polymers (predominantly polyolefins) and preparation of high performance engineering materials and nanocomposites by using reactive extruder systems and in situ compatibilization of polymer blends have been significantly developed, some results of which are employed in commercial applications [9].

The grafting of styrene-butadiene block copolymers with maleic anhydride occurs by radical mechanism. In literature are presented both the grafting mechanism and the influence of reaction conditions: concentration, structure, and position of the grafted anhydride, depending on the used method (solution, melt state and solid state), and the temperature, pressure, concentration, solvent, additive, etc. [10-11].

Iancu L. et al. [10] studied the functionalization reaction of the styrene-butadiene block copolymers with maleic anhydride was carried out in butyl acetate solution using 2, 2'-azo-bis-isobutyronitrile as initiator.

Passaglia et al. [12] studied the functionalization of polystyrene (PS) block in styrene-b-(ethylene-co-1-butene)-b-styrene (SEBS) triblock copolymer with AM and diethyl maleate (DEM). According to the authors, grafting of AM onto a-PS can be accomplished through a radical process, although the reaction mechanism is not clarity. The bulk functionalization of SEBS triblock copolymer with DEM or AM and dicumyl peroxide as initiator was carried out in a Brabender mixer. They established that the functionalization takes place with a very large preference at the aliphatic carbons of the polyolefin block. Moreover occurrence of degradation and chain extension reactions gives a functionalized product with a molecular weight distribution larger than 1.

A. Kurbanova et al. [13] have shown that functionalization of PS by grafting reaction can be carried out either via the polymer backbone in the case of radical initiators or through the side phenyl rings using cationic catalysts. They chemically modified PS with AM by use of certain cationic catalysts of Lewis acid type ( $\text{AlCl}_3$ ,  $\text{TiCl}_4$ ,  $\text{ZnCl}_2$ ,  $\text{FeCl}_3$ ,  $\text{SnCl}_4$  etc.) in chloroform at 0-30°C.

Rocetti L and Banzi V [14] have shown that the grafting of maleic anhydride onto unsaturated olefinic polymers (such as ethylene-propylene-ethylidene-1,3,-butadiene terpolymer etc.) can be carried out by mass polymerization, without encountering the above drawbacks, by allowing the reaction to take place in the presence of catalysts being compounds of metals of group VIII of the periodic system (in particular Rh and Ru), wherein the reaction mixture is heated at temperatures of from about 120°C to about 350°C.

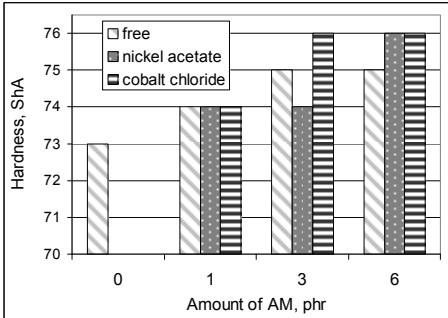
This article presents SBS maleinization by melt mixing the elastomer with AM in the presence of an additive/catalyst. SBS elastomers containing ionizable groups obtained were processed with a metal oxide - ZnO (which can react with the functional groups in the ionizable groups, thus yielding ionic ranges), filler, ionic plasticizer, antioxidants etc. in order to obtain ionic thermoplastic elastomer compounds. The following were studied: influence of the AM amount, of the type and amount of catalyst, and the mixing time after adding AM, on the physico and mechanical properties of blends. Also, the influence of the neutralization degree on physico-mechanical properties of blends based on SBS-g-AM rubber was studied.

## RESULTS AND DISCUSSIONS

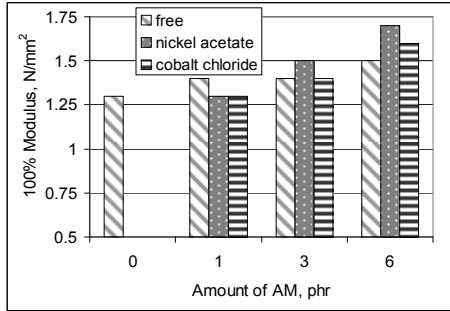
### 1. Influence of AM amount on the physico-mechanical properties

Figure 1 presents the effect of increasing the amount of AM on physico-mechanical properties of compounds based on SBS-g-AM. Mixing time after adding AM was 5' and the amount of catalyst was 0.5 phr (parts to 100 parts rubber). It is noticed that upon increasing the amount of AM, hardness and modulus also increase, indicating the growth of ionic groups on the macromolecular chain. Due to the property of groups specific to maleic anhydride existing on the macromolecular chain of reacting with oxides of divalent metals (zinc oxide), ionic bonds form similar to sulphur bridges from vulcanized rubber. This ionic crosslinking has led to an improvement in the value of the module and hardness. Zinc oxide replaces sulphur and vulcanization agents in these blends [15]. Concomitantly, adding ionic groups in SBS leads to a decrease in tensile strength, elongation at break and tear strength. This is explained through the existence of polar bonds  $\text{COO}^-$  which repel each other, as well as through the change in the polymer structure due to the grafting reaction [10].

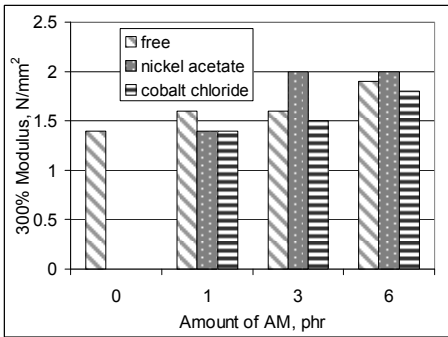
It is noticed that better properties are obtained for blends where additive/nickel acetate or cobalt chloride catalyst were used. As no significant differences of properties of mixtures containing 3 phr AM compared to those containing 6 phr AM were noticed, the next samples were processed using an amount of 3 phr AM.



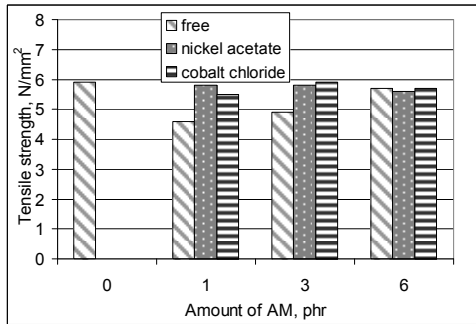
(a) Hardness



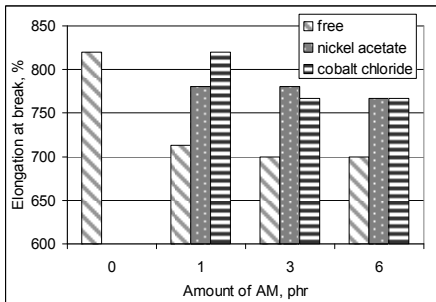
(b) 100% Modulus



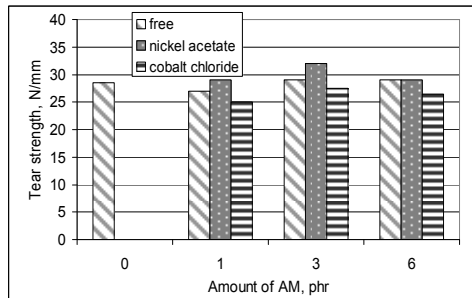
(c) 300% Modulus



(d) Tensile strength



(e) Elongation at break



(f) Tear strength

**Figure 1.** Influence of AM amount on physico-mechanical properties\*

\*The unit “phr” is “parts to 100 parts rubber” which is a weight measurement relative to the amount of rubber in the formulation.

## 2. Influence of mixing time after adding AM on the physico-mechanical properties

In order to determine the influence of mixing time after adding AM, blends were made in which 3 phr AM and 0.5 phr catalyst were added. In this case, better physico-mechanical properties are obtained for blends containing catalyst, particularly based on cobalt chloride, which, even after 2'30", have led to blends with very good values for hardness, modulus, tensile strength and elongation at break. The best characteristics were obtained after mixing for 5'.

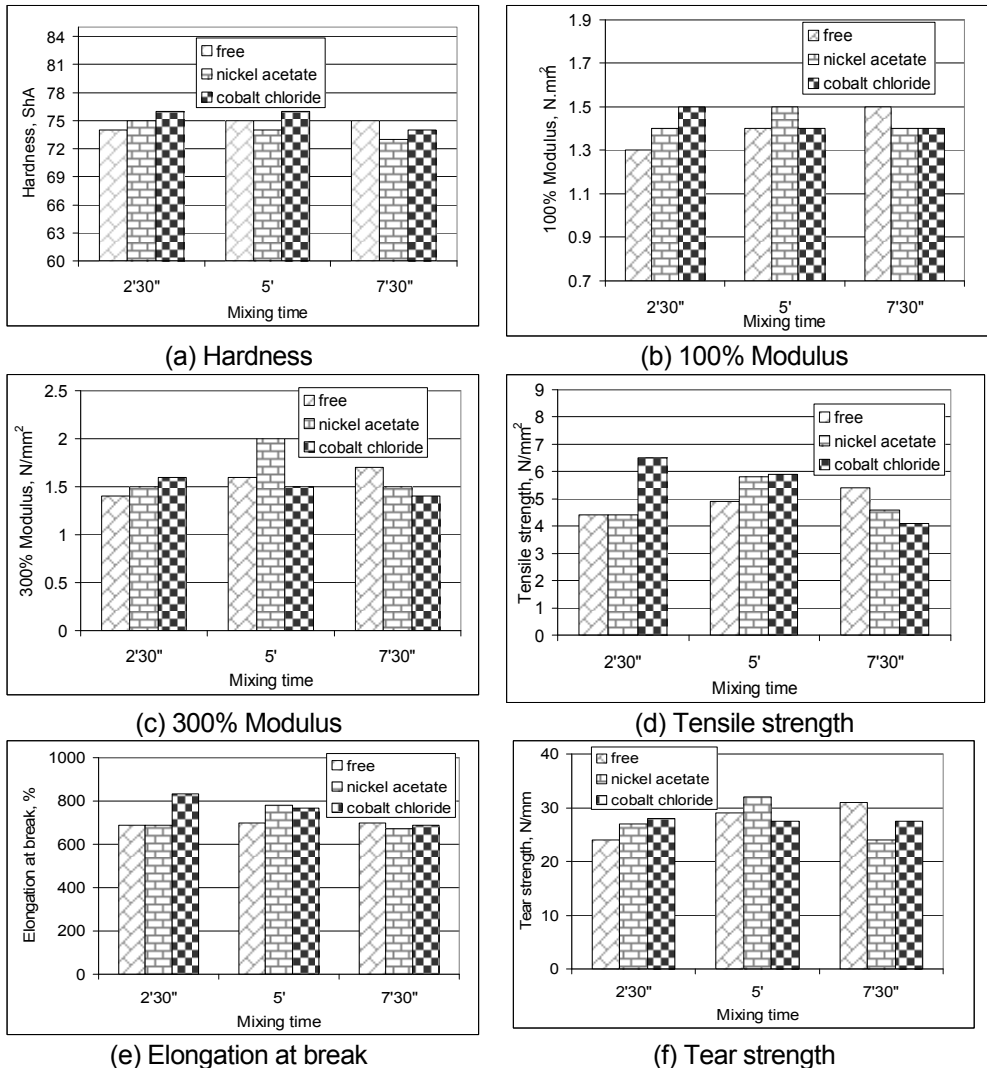


**Figure 2.** Influence of mixing time after adding AM on physico-mechanical properties

### 3.3. Influence of the catalyst amount on physico-mechanical properties

In order to determine the influence of catalyst amount on physico-mechanical properties, mixtures were made containing 3 phr AM, and the time after adding AM was 5'.

It can be noticed that, upon the significant increase of catalyst amount, no similar improvement of physico-mechanical properties occurs. Based on results presented in Figure 3 and in Figures 1 and 2, the mixture containing 0.5 phr cobalt chloride and 3 phr AM, mixing time 5' after adding AM, was selected.

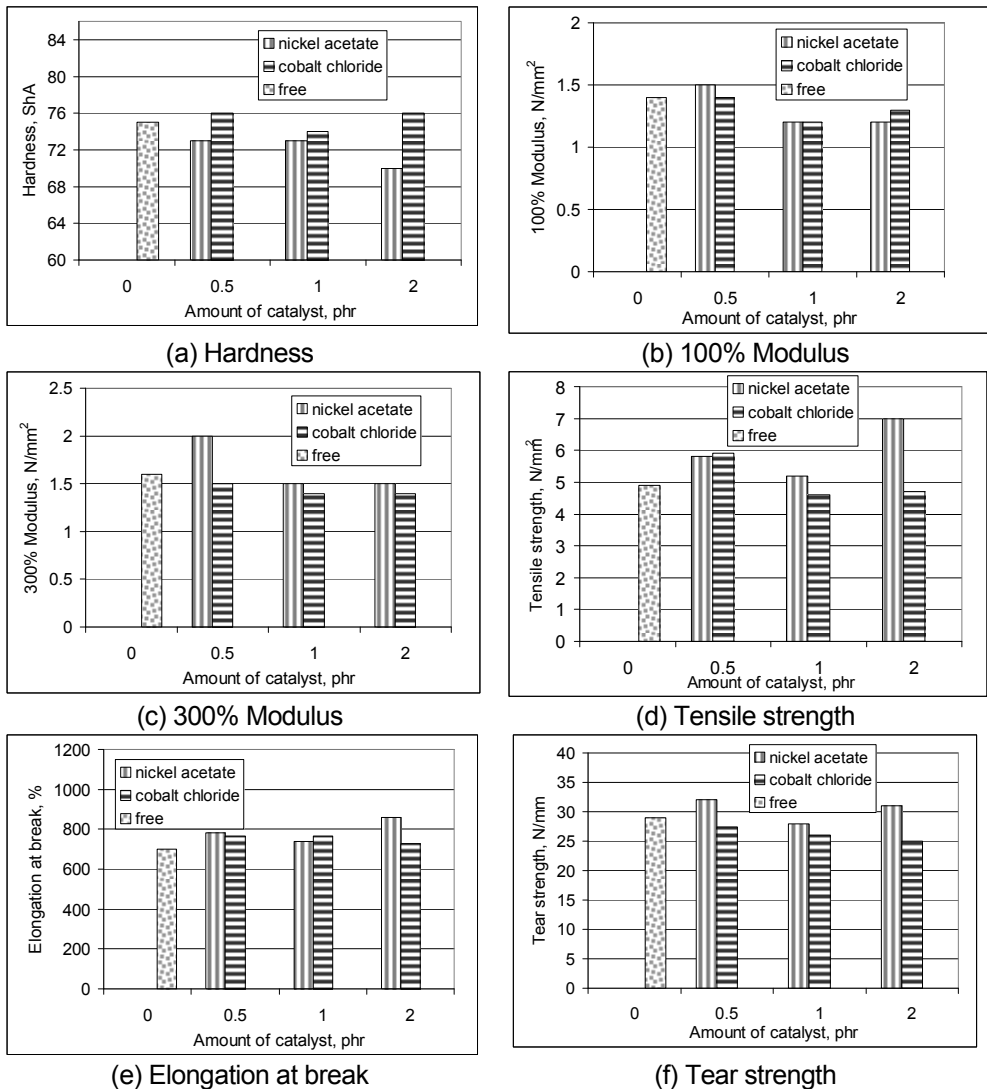


Figure 3. Influence of catalyst amount on physico-mechanical properties

### 3.4. Influence of the crosslinking degree on SBS-g-AM ionic thermoplastic elastomer characteristics

Table 1 presents formulations and characteristics for the polymer blends based on chemically unmodified SBS (M0 and M1) and blends where SBS elastomer was chemically modified by adding 3 phr AM in the presence of 0.5 phr cobalt chloride, mixing time after adding AM was 5'.

Comparing characteristics of blends where SBS is not modified (M0 and M1) with those having a similar composition, where SBS-g-AM was used (A0 and A2), it can be noticed that, as a result of the maleinization reaction, hardness decreased very much (by 10-13°ShA) and tensile strength and elongation at break also decreased. This can be due to the chemical modification of SBS through maleinization, which led to a change in the packing degree of macromolecules, changing the structure of the elastomer. This has also been reported by other researchers [10].

Analyzing the data in Table 1 it is noticed that upon adding ZnO in the blend containing chemically unmodified SBS (blend M0 compared to M1), no substantial change occurs in the physico-mechanical properties. In contrast, for blends containing SBS-g-AM (A0 compared to A1, A2, A3), it is noticed that upon increasing the amount of ZnO, hardness, 100% modulus and 300% modulus increase, while tensile strength and elongation at break increase up to a maximum and then decrease. This is due to ionic crosslinks forming between zinc ions and COO<sup>-</sup> groups of SBS-g-AM, upon increasing the neutralization degree of ionic groups in SBS-g-AM [15].

**Table 1.** Formulations and characteristics for the polymer blends based on SBS and SBS-g-AM

Ingredients / Mixture symbol	M0	M1	A0	A1	A2	A3
SBS	100	100				
SBS-g-AM		<b>0</b>	100	100	100	<b>100</b>
ZnO		5		2	5	10
Stearine		0.5		0.2	0.5	1
Irganox 1010		0.5		0.5	0.5	0.5
<b>Properties</b>						
Hardness, °ShA	70	69	57	59	59	61
100 % Modulus, N/mm <sup>2</sup>	1.1	0.7	0.9	1	1	1.2
300 % Modulus, N/mm <sup>2</sup>	1.3	1.2	1.3	1.9	2	<b>2</b>
Tensile strength, N/mm <sup>2</sup>	8.7	8.2	4	4.5	6.4	4.9
Elongation at break, %	890	900	620	620	680	540

Samples M0 and A0 were processed in order to be subjected to FTIR spectrophotometric analyses according to the work method presented in chapter 2. FTIR spectra are presented in Figures 4 and 5. Analysis of these spectra shows that the band at  $875.6\text{ cm}^{-1}$ , determined by the deformation vibration of CH bond in the aromatic ring, is more prominent for the SBS-g-AM spectrum and can indicate the fact that AM substituted a hydrogen atom in the meta position. The band at  $1421\text{ cm}^{-1}$  highlights the existence of COOH group, namely  $\nu\text{C}=\text{O}$  and  $\delta\text{OH}$  coupled bonds. This band overlaps with the band specific to the vibration of  $\delta\text{CH}_2$  bond, as well as with the one specific to double bonds in the aromatic ring.

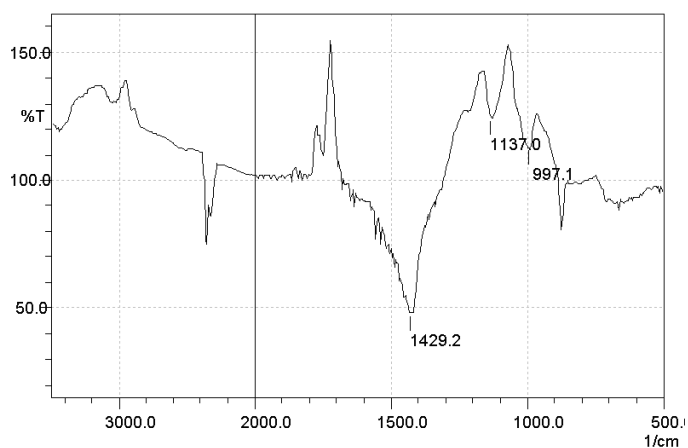


**Figure 4.** FT-IR spectra of styrene-butadiene block copolymer Calprene 484 (sample M0)

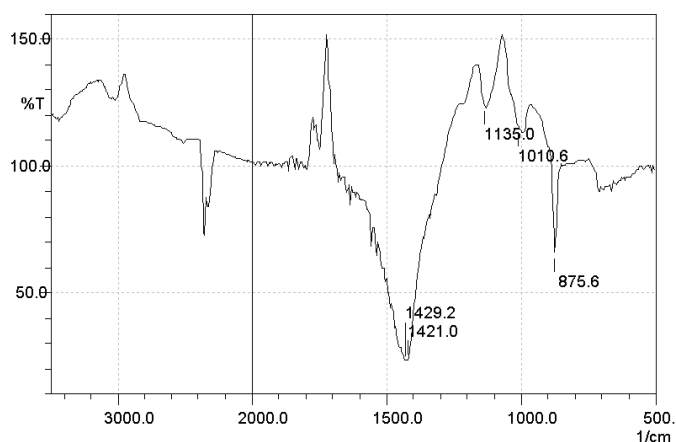


**Figure 5.** FT-IR spectra of maleinized styrene-butadiene block copolymer (sample A0)

## CONCLUSIONS

As a result of the conducted study, it can be concluded that SBS was maleinized by melt mixing the elastomer with AM in the presence of an additive/catalyst. The influence of AM amount, of the type and amount of catalyst and of the mixing time after adding AM on the physico-mechanical properties of blends was studied and optimal working parameters were established in order to obtain desired characteristics.

The new types of thermoplastic elastomers can be processed by specific techniques for thermoplastic materials, thus removing the vulcanization stage involving high power expenditure and release of noxious products, improved characteristics of these materials can be assured.

The potential users of the new rubber materials will be economic operators processing rubber and plastics, footwear and car component manufactures etc.

## EXPERIMENTAL

SBS maleinization was performed by melt mixing SBS with AM in the presence of an additive/catalyst. Mixing was performed in Plasticorder Brabender PLV 330 at 100 rpm and temperature of 180°C to allow the elastomer to melt. After elastomer melting, the catalyst was added, and then the maleic anhydride. We monitored the influence of AM amount, of the type/amount of catalyst and of the reaction time after adding AM on the physico-mechanical properties of ionic thermoplastic elastomer compounds obtained.

The following materials were used in the study to obtain SBS-g-AM:

*1,3-Butadiene-styrene block* polymer Calprene 484 (melt flow index at 190°C, 5kg, 7.5 g/10', volatile matter, 0.4%, oil, 31.5 %, total styrene (on polymer), 44 %, density 0.95 g/cm<sup>3</sup>).

Two types of additives/catalysts were used: (a) *cobalt chloride hexahydrate* - CoCl<sub>2</sub> x 6H<sub>2</sub>O - Lewis acids, molar mass 237,93 g/mol, density 1.924 g/cm<sup>3</sup>, appearance - pink monoclinic crystals, soluble in: water, ethyl alcohol, diethyl ether, acetone. (b) *nickel acetate tetrahydrate* (CH<sub>3</sub>COO)<sub>2</sub>Ni x 4H<sub>2</sub>O, molar mass 248.86 g/mol, density 1.79 g/cm<sup>3</sup>, appearance – green crystals.

*Maleic anhydride* - C<sub>2</sub>H<sub>2</sub>(CO)<sub>2</sub>O, molar mass 98.06 g/mol, appearance - white crystals, density 1.48 g/cm<sup>3</sup>, melting point 52.8°C; boiling point 202°C.

In order to analyze the efficiency of the method of SBS chemical modification (through maleinization) on the physico-mechanical properties, ionic thermoplastic elastomer compounds were developed using SBS elastomers chemically modified by grafting with maleic anhydride (SBS-g-AM).

They were obtained by adding: neutralizing agent of ionic groups - zinc oxide (zinc oxide content 99.2%, humidity 0.15%, free zinc 0.14%), stearophanic acid (titre fatty acids 59, mineral acids absence), ionic plasticizer- zinc stearate; (Zn content 11%, melting point 127°C), as active filler precipitated silica Ultrasil VN 30 and antioxidant Irganox 1010 - pentaerythritol tetrakis (3-(3,5-di-tert-butyl-4-hydroxyphenyl) propionate. Blends were developed on Plasticorder Brabender PLV 30. The process variables were: temperature: 170°C and rotational speed: 100 rpm.

The blends were homogenized on an electrically heated laboratory roller mill. The optimum process variables were: temperature: 150-160°C and friction coefficient: 1:1.1. The distance between the rolls was of 2 mm for 1', it decreased to 0.2 mm for 3' and then increased to 2 mm for 1' and the mixture was taken off the roller mill in a sheet.

Samples used in tests for physico-mechanical characterization were made by means of a laboratory electrical press at a temperature of 170°C and 150 MPa, pre-heating time 2', modeling time 5' and room temperature cooling time 2'.

Mechanical properties of samples were measured on a Schopper tensile tester with a nominal rate of the traverse of the moving grip of 460 mm/min. Modulus at 100% and 300% strain, tensile strength and elongation at break tests were carried out according to the conditions described in ISO 37/2012, on dumb-bell shaped specimens of Type 2. Tearing strength tests were carried out using angular test pieces (type II) according to SR EN 12771/2003. Hardness of materials was measured using the Shore A scale, by using a hardener tester according to ISO 7619-1/2011.

AM grafting on the SBS macromolecular chain was highlighted by FTIR spectroscopy. In order to do this: (a) the polymer was dissolved in toluene ( $\rho = 0.866 \text{ g/cm}^3$ ) at room temperature (approximately 5 hours), (b) the polymer was precipitated with acetone ( $\rho = 0.790 \text{ g/cm}^3$ ), (c) the precipitate was filtered and washed with acetone several times; (d) the precipitate was dried to eliminate traces of solvents and then used in FTIR spectroscopic analysis. A Shimadzu 8900 device was used for this, range: 4000 - 400  $\text{cm}^{-1}$ , resolution 2  $\text{cm}^{-1}$ .

## REFERENCES

- [1]. F. Ciardelli, M. Aglietto, E. Passaglia, F. Picchioni, *Polym. Adv. Technol.*, **2000**, 11, 371.
- [2]. Edwards DC, Sato K., *Chem. Technol.*, **1980**, 53, 66.

- [3]. A. Bhattacharya, B.N. Misra, *Prog. Polym. Sci.*, **2004**, *29*, 767.
- [4] Craciun, G., Manaila, E., Martin, D., Toader, D., Ighigeanu, D., *Materiale plastice*, **2011**, *48* (2), 183.
- [5] Timus, D.M., Cincu, C., Bradley, D.A., Craciun, G., Mateescu, E., *Applied radiation and isotopes*, **2000**, *53* (4-5), 937.
- [6] Martin, D.I., Ighigeanu, D.I., Mateescu, E.N., Craciun, G.D., Calinescu, I.I., Iovu, H.M., Marin, G.G., *IEEE transactions on industry applications*, **2004**, *40* (1), 41.
- [7] Martin, D., Ighigeanu, D., Mateescu, E., Craciun, G., Ighigeanu, A., *Radiation physics and chemistry*, **2002**, *65* (1), 63.
- [8]. A. Pucci, C. Barsocchi, R. Rausa, L. D'Elia, F. Ciardelli, *Polymer*, **2005**, *46*, 1497.
- [9]. Zakir M.O. Rzaev, *International Review of Chemical Engineering*, **2011**, *3*(2), 153.
- [10]. L. Iancu, P. Ghioca, B. Spurcaci, R.M. Grigorescu, C.-A. Nicolae, R.A. Gabor, *Materiale Plastice*, **2013**, *50* (2), 137.
- [11] Roover B., Sclavons M., Carlier V., Devaux J., Legras R., Momtaz A., *J. Polym. Sci, Polym. Chem.*, **1995**, *33*, 829;
- [12] E. Passaglia, S. Ghetti, F. Picchioni, G. Ruggeri, *Polymer*, **2000**, *41*, 4389.
- [13]. R.A. Kurbanova, R. Mirzaoğlu, G. Akovalı, Z.M. O. Rzaev, I. Karataş, A. Okudan, *J. Appl. Polym. Sci.*, **1996**, *65*, 235.
- [14]. Rocetti L and Banzi V, EP 0 353 720 A2, 07.02.1990, Bulletin 90/06, Process for grafting maleic anhydride onto unsaturated polyolefinic elastomers.
- [15]. Stelescu, M.D. (2010), The influence of the crosslinking degree on EPDM-g-MA elastomer characteristics, Proc. 3rd Int. Conf. Adv. Mater. Systems, ICAMS 2010, 137-142, Bucuresti, Romania, Sept. 16-18, 2010.



## EDGE GEOMETRIC-ARITHMETIC INDEX OF SOME GRAPHS

M. SAKI<sup>a</sup>, A. IRANMANESH<sup>b\*</sup> O. KHORMALI<sup>c</sup>

**ABSTRACT.** The edge version of geometric–arithmetic index of graphs is introduced based on the end-vertex degrees of edges of their line graphs. In this paper we compute this index for product graphs  $P_n \times P_m$  and  $P_n \times C_m$ , and a dendrimer nanostar  $D_n$ .

**Keywords:** edge geometric–arithmetic index, line graph, vertex degree, dendrimer

### 1. INTRODUCTION

A single number that can be used to characterize some properties of molecular graphs is called a topological index. There are numerous topological descriptors that have found applications in the theoretical chemistry, especially in QSPR/QSAR research [1]. The oldest topological index, introduced by Harold Wiener in 1947, is the ordinary (vertex) version of Wiener index [2], which is the sum of all distances between vertices of a graph. There is also known an edge versions of Wiener index, based on distance between edges, introduced by Iranmanesh et al. in 2008 [3].

One of the most important topological indices is the Randić connectivity index [4], defined as the sum of certain bond contributions calculated from the vertex degree of the hydrogen suppressed molecular graphs.

Inspired by the Randić index in a graph  $G(V, E)$ , with  $V(G)$  being the vertex/atom set and  $E(G)$  the edge/bond set, [5,6], Vukicevic and Furtula [7] proposed a topological index named the geometric-arithmetic index (shortly GA) as

---

<sup>a</sup> Department of Mathematics, Science and Research Branch, Islamic Azad University, Tehran, Iran

<sup>b</sup> Department of Pure Mathematics, Faculty of Mathematical Sciences, Tarbiat Modares University, Tehran, Iran

<sup>c</sup> Mathematics and Informatics Research Group, ACECR, Tarbiat Modares University, Tehran, Iran

\* Corresponding author: iranmanesh@modares.ac.ir

$$GA(G) = \sum_{uv \in E(G)} \frac{2\sqrt{d_G(u)d_G(v)}}{d_G(u) + d_G(v)}$$

where  $d_G(u)$  denotes the degree of the vertex  $u$  in  $G$ . The reader can find more information about geometric-arithmetic index in [7-9].

In [10], the edge version of geometric-arithmetic index (edge GA index) was introduced, based on the end-vertex degrees of edges in a line graph of  $G$ ; it is a derived graph such that each vertex of  $L(G)$  represents an edge in  $G$  and two vertices of  $L(G)$  are adjacent if and only if their corresponding edges share a common endpoint in  $G$

$$GA_e(G) = \sum_{ef \in E(L(G))} \frac{2\sqrt{d_{L(G)}(e)d_{L(G)}(f)}}{d_{L(G)}(e) + d_{L(G)}(f)}$$

where  $d_{L(G)}(e)$  denotes the vertex degree in  $L(G)$  or the degree of edge  $e$  in the original graph  $G$ .

We can calculate the edge GA index as

$$GA(G) = \sum_{i=1}^{|E(G)|} \xi_i$$

where  $\xi_i = \frac{2\sqrt{du_i dv_i}}{du_i + dv_i}$ . Also, we have  $d_e = d_u + d_v - 2$  where  $e = uv \in E(G)$ .

Then the number of edges in a line graph is

$$|E(L(G))| = \frac{1}{2} \sum_{e_i = u_i v_i \in E(G)} (d_{u_i} + d_{v_i} - 2) \times |E_i|$$

where  $|E_i| = \left| \left\{ e_i \mid e_i \in E(G), e_i = (du_i, dv_i) \right\} \right|$ .

In this paper, we compute this index for product graphs  $P_n \times P_m$  and  $P_n \times C_m$  and a dendrimer nanostar  $D_n$ .

## 2. EDGE GA INDEX OF PRODUCT GRAPHS $P_n \times P_m$ AND $P_n \times C_m$

At first, we compute the edge GA index for the product graph of two paths  $P_n$  and  $P_m$ , i.e.,  $P_n \times P_m$ . In Figure 1, the graph of  $P_7 \times P_6$  is shown. According to this figure, we have

$$\begin{aligned} |E(P_n \times P_m)| &= |E(P_n)| \times |V(P_m)| + |E(P_m)| \times |V(P_n)| \\ &= (n-1)(m) + (m-1)(n) = 2mn - (n+m) \end{aligned}$$

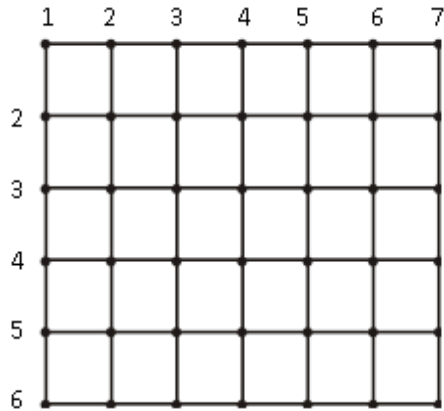


**Figure 1.** The graph of  $P_7 \times P_6$

In Figure 2, the line graph of  $P_7 \times P_6$  is shown. Accordingly, we have

$$|E(L(P_n \times P_m))| = 6mn - 6(n + m) + 4.$$

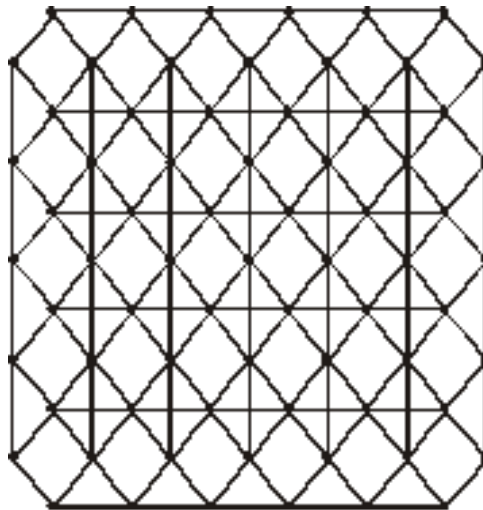


**Figure 2.** The graph of  $L(P_7 \times P_6)$

In Table 1, the type of edges, their numbers and amount of  $\xi_i$  are computed.

**Table 1.** Type of edges, their numbers and amount of  $\xi_i$  of  $L(P_n \times P_m)$

Number of edges	$\xi_i$	Type of edges
4	1	(3,3)
8	$\frac{2\sqrt{12}}{7}$	(3,4)
8	$\frac{2\sqrt{15}}{8}$	(3,5)
4	1	(5,5)
$2(n-4)+2(m-4)$	1	(4,4)
$4(n-3)+4(m-3)$	$\frac{2\sqrt{20}}{9}$	(4,5)
$6(n-4)+8(m-2)$	$\frac{2\sqrt{30}}{11}$	(5,6)
$6mn-18n-20m+60$	1	(6,6)

Then, we have the following Theorem:

**Theorem 1.** The edge GA index of  $P_n \times P_m$  is

$$GA_e(P_n \times P_m) = 6mn + \left( \frac{12\sqrt{30}}{11} + \frac{16\sqrt{5}}{9} - 16 \right) n + \left( \frac{16\sqrt{30}}{11} + \frac{16\sqrt{5}}{9} - 18 \right) m - \frac{96\sqrt{5}}{9} - \frac{80\sqrt{3}}{11} + 2\sqrt{15} + \frac{32\sqrt{3}}{7} + 52.$$

**Proof.** According to Table 1 and Figure 2, we obtain the result.

Now, we compute the edge GA index of  $P_n \times C_m$ , with  $C_m$  being a cycle of size  $m$ . In Figure 3, the graph of  $P_6 \times C_4$  is indicated. According to the following figure, we have  $|E(P_n \times C_m)| = (n-1)m + n.m = 2nm - m$ .

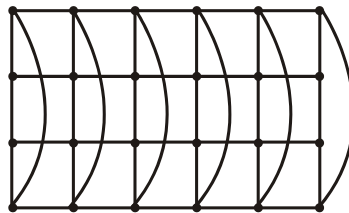


**Figure 3.** The graph of  $P_6 \times C_4$

In Figure 4, the line graph of  $P_6 \times C_4$  is shown. Accordingly, we have :

$$|E(L(P_n \times C_m))| = \frac{1}{2} [(3+3-2)(2m) + (3+4-2)(2m) + (2mn-5m)(4+4-2)]$$

$$= 6mn - 6m$$

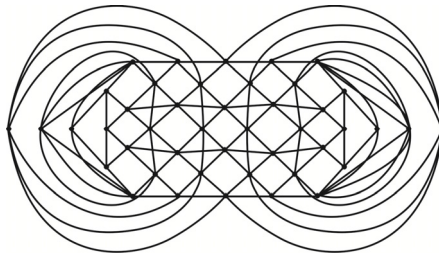


**Figure 4.** The graph of  $L(P_6 \times C_4)$

In Table 2, the type of edges, their numbers and amount of  $\xi_i$  are computed.

**Table 2.** The type of edges, their numbers and amount of  $\xi_i$  of  $L(P_n \times C_m)$

No. of edges	$\xi_i$	Type of edges
2m	1	(4,4)
4m	$\frac{4\sqrt{5}}{10}$	(4,5)
6m	$\frac{2\sqrt{30}}{11}$	(5,6)
6mn-18m	1	(6,6)

Then, we have the following Theorem:

**Theorem 2.** The edge GA index of  $P_n \times C_m$  is

$$GA_e(P_n \times C_m) = 6mn + \left( \frac{16\sqrt{5}}{9} + \frac{12\sqrt{30}}{11} - 16 \right) m.$$

**Proof.** According to Table 2 and Figure 4, we obtain the result.

### 3. EDGE GA INDEX OF DENDRIMER NANOSTAR $D_n$

In Figure 5, the dendritic graph  $D_n$  is shown. According to this figure, we

have  $|E(D_n)| = 66 \cdot 2^{n-1} - 45$ .

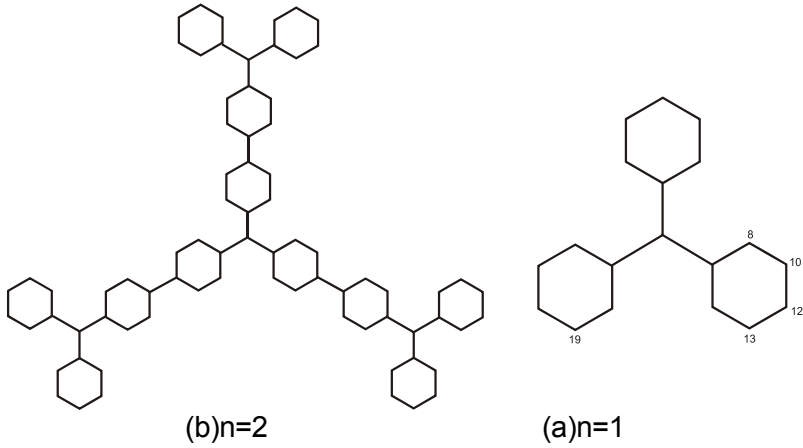


**Figure 5.** The dendrimer graph  $D_n$

In Figure 6, the line graph of  $D_2$  is shown. According to this figure, we have

$$|E(L(D_n))| = \frac{1}{2} \left[ (2+2-2) \cdot (24 \times 2^{n-1} - 12) + (2+3-2) (3 \times 2^{n-1} - 24) + (3+3-2) (12 \times 2^{n-1} - 9) \right]$$

$$= 93 \times 2^{n-1} - 66$$

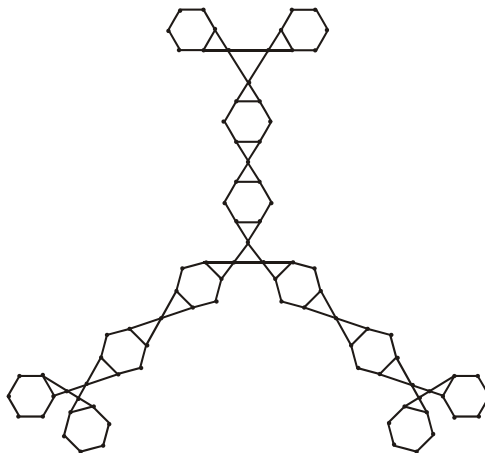


**Figure 6.** The line graph of  $D_2$

In the Table 3, the type of edges, their numbers and amount of  $\xi_i$  for this graph are computed.

**Table 3.** The type of edges, their numbers and amount of  $\xi_i$  of  $L(D_n)$

No. of edges	$\xi_i$	Types of edges
$9 \times 2^{n-1}$	1	(2,2)
$15 \times 2^{n-1} - 12$	1	(3,3)
$30 \times 2^{n-1} - 24$	$\frac{4\sqrt{3}}{7}$	(3,4)
$30 \times 2^{n-1} - 24$	$\frac{2\sqrt{6}}{5}$	(2,3)
$9 \times 2^{n-1} - 6$	1	(4,4)

Then, we have the following

**Theorem 3.** The edge GA index of  $D_n$  is

$$GA_e(D_n) = \left( 33 + \frac{120\sqrt{3}}{7} + 12\sqrt{6} \right) \times 2^{n-1} - \frac{96\sqrt{3}}{7} - \frac{48\sqrt{6}}{5} - 18$$

**Proof.** According to Table 3 and Figure 6, we obtain the result.

## CONCLUSIONS

By using the graph theory techniques, we computed the edge GA index for the product graphs  $P_n \times P_m$  and  $P_n \times C_m$ , and a dendrimer nanostar  $D_n$  and we expressed their exact values.

## REFERENCES

- [1] R. Todeschini, V. Consonni, "Handbook of Molecular Descriptors", Weinheim, Wiley-VCH, **2000**.
- [2] H. Wiener, *J. Am. Chem. Soc.*, **1947**, *69*, 17.
- [3] A. Iranmanesh, I. Gutman, O. Khormali, A. Mahmiani, *MATCH Commun. Math. Comput. Chem.*, **2009**, *61*(3), 663.
- [4] M. Randic, *J. Amer. Chem. Soc.*, **1975**, *97*, 6609.
- [5] X. Li, I. Gutman, "Mathematical Aspects of Randić-Type Molecular Structure Descriptors", Univ. Kragujevac, Kragujevac, **2006**.
- [6] I. Gutman, B. Furtula, "Recent Results in the Theory of Randić Index", Univ. Kragujevac, Kragujevac, **2008**.
- [7] D. Vukicevic, B. Furtula, *J. Math. Chem.*, **2009**, *46*, 1369.
- [8] Gh. Fath-Tabar, B. Furtula, I. Gutman, *J. Math. Chem.*, **2010**, *47*, 477.
- [9] Y. Yuan, B. Zhou, N. Trinajsti, *J. Math. Chem.*, **2010**, *47*, 833.
- [10] A. Mahmiani, O. Khormali, A. Iranmanesh, *Digest Journal of Nanomaterials and Biostructures*, **2012**, *7*(2), 411.

## 2-MERCAPTO-5-ACETYLAMINO-1,3,4-THIADIAZOLE AS CORROSION INHIBITOR FOR A NATURALLY PATINATED MONUMENTAL BRONZE ARTIFACT

JULIETA DANIELA CHELARU<sup>a</sup>, LIANA MARIA MURESAN<sup>a,\*</sup>

**ABSTRACT.** The present work aims to investigate the corrosion behavior of bronze screws covered with natural patina used in assembling the statuary group of Mathias Rex, placed in the center of Cluj-Napoca, Romania, dating back to 1902. Corrosion tests were carried out in the absence and presence of inhibitors in a 0.2 g / L Na<sub>2</sub>SO<sub>4</sub> + 0.2 g / L NaHCO<sub>3</sub> (pH = 5) solution simulating an acid rain. The research put on evidence the inhibiting effect of 2 - mercapto - 5 acetylamino - 1, 3, 4 - thiadiazole on the naturally patinated artefacts in order to avoid their further degradation. The obtained results were compared with those recorded in the presence of benzotriazole, the most common corrosion inhibitor for Cu and bronze.

**Key words:** *bronze, atmospheric corrosion, natural patina, acid rain, corrosion inhibitors*

### INTRODUCTION

Bronze (Cu - Sn based alloy) is one of the most widely used alloy in the monumental art. Exposed outdoors, the bronze develops in time a layer of corrosion products, called natural patina. There are many studies on the atmospheric corrosion of bronze and on the formation mechanisms of bronze corrosion products [1-7]. Some of these studies show that, in the case of bronze, there are two types of patina, respectively: Type I, or “even” surfaces and Type II, or “coarse” or “burgeoning” surface [1]. Type I patina is very protective and develops on the bronze surface an aesthetic pleasant aspect, for this reasons being called “noble patina” [1]. It has different colours depending on the nature of the atmosphere: blue, green, dark green or dark grey. On the other hand, the Type II patina is inferior to Type I and is characterized by changes of the original surface, being rough and

---

<sup>a</sup> Department of Chemical Engineering, “Babes-Bolyai” University, 11 Arany Janos St., 400028 Cluj-Napoca, Romania

\* Corresponding author: [liimur@chem.ubbcluj.ro](mailto:liimur@chem.ubbcluj.ro)

porous and coloured in red, brown or green [1]. Due to the increasing pollution in recent years is necessary to protect the “noble patina”. One common method is the use of corrosion inhibitors.

Recent studies have shown that benzotriazole (BTA), a consecrated inhibitor for cooper alloys, is highly toxic and carcinogenic [8]. Moreover, in time it leads to a depreciation of patina color (blackening). For this reason efforts are made towards finding protection methods based on the use of less toxic inhibitors for copper and bronze protection. In recent papers, different innocuous thiadiazole derivatives, namely 2 - amino - 5 - mercapto - 1, 3, 4 - thiadiazole [8-11], 2 - amino - 5 - ethylthio - 1, 3, 4 - thiadiazole [12], 2 - amino - 5 - ethyl - 1, 3, 4 - thiadiazole [13], 2 - methyl - 5-mercapto - 1, 3, 4 - thiadiazole [11], and 2 - acethylamino - 5 - mercapto - 1, 3, 4 - thiadiazole [14, 15], have been reported as efficient inhibitors for copper or bronze corrosion in different corrosive media. However, their effect on the natural patina of bronze artifacts is still to be investigated.

In this context, the present research focuses on the effect of an innocuous thiadiazole derivative on the corrosion behavior of some deteriorated bronze screws covered with natural patina, originating from the statuary group of Mathias Rex from Cluj-Napoca, Romania, in an aerated electrolyte simulating an acid rain (pH 5). The recent restoration of the bronze statuary group provided a unique occasion to better understand the impact of environmental conditions on the degradation of bronze components and to investigate the conservation possibilities directly on the bronze artifacts covered with natural patina, which had to be replaced. For this purpose, investigations have been made by means of electrochemical, microscopic and spectroscopic methods. The obtained results were compared with those recorded in the presence of BTA and could serve for the statuary group conservation well as for future protection of other monumental bronzes.

## RESULTS AND DISCUSSION

The chemical composition of bronze screws used for experiments was determined by X-ray fluorescence spectrometry (XRF). The results show that the alloy of screws is a binary Cu<sub>6</sub>Sn bronze of the following composition: 91.89 % copper, 5.15 % tin, 1.25 % zinc, 1.04 % lead and 0.57 % iron.

By microscopic observation (Fig. 1) it is shown that the corrosion products layer is porous, rough with cracks and pits. This indicated that the bronze screws analyzed were severely corroded [16]. It can be also observed that the patina layer is not uniform, so some alloy areas are not covered (Fig. 1b).

For the microscopic investigation, the bronze screws were polished on the sample polishing machine with alumina paste, after which the surface was washed with ammonia cupric chloride to bring out the grain contrast. Figure 2 presents the microscopic structures of the bronze screws, subjected to this study magnified at 100X and 200X.



**Fig. 1.** Microscopic observation of patina on bronze screw from Matthias Rex statuery group: (a), (b) X100.

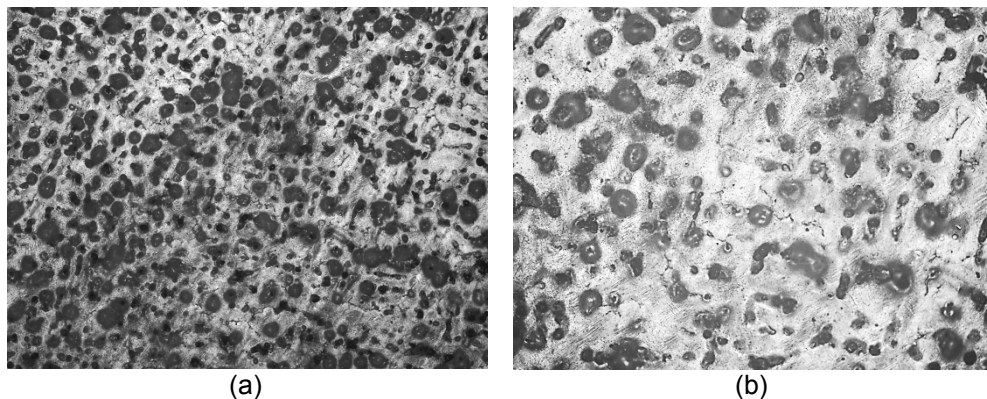
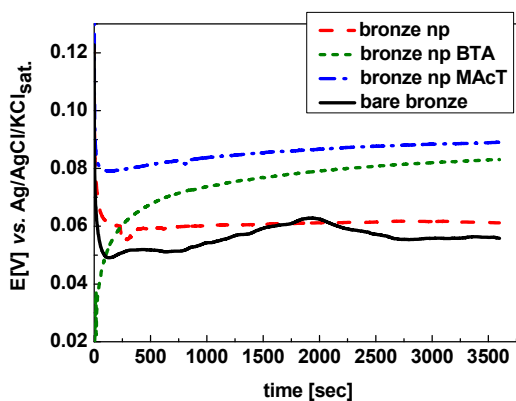


**Fig. 2.** Microscopic structure of bronze screws used for electrochemical studies: (a) X100, (b) X200.

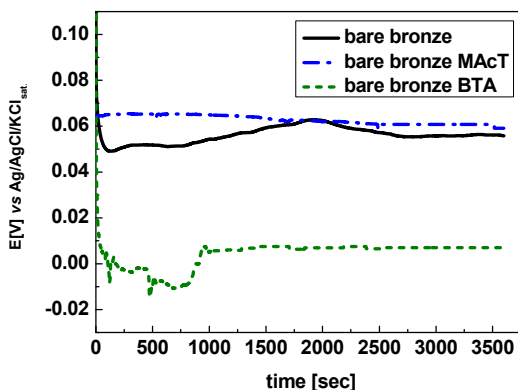
The microscopic structure of the bronze is a typical one. According to Scott [17] some of the inclusions observed in the metal are of cuprite ( $\text{Cu}_2\text{O}$ ), other are of segregated lead. In our case, the surface is rich in copper  $\alpha$ -phase with punctiform eutectoid ( $\alpha + \delta$ ) and lead segregations. This can be ascribed to the casting process that has resulted in the segregation of lead and to the fact that annealing was not extensive enough to eliminate all of the ( $\alpha + \delta$ ) eutectoid [17].

### Polarization measurements

In a first step, the corrosion behavior of bronze screw covered with natural patina was studied in the absence and in the presence of corrosion inhibitors in an electrolyte containing 0.2 g / L  $\text{Na}_2\text{SO}_4$  + 0.2 g / L  $\text{NaHCO}_3$ , pH = 5.



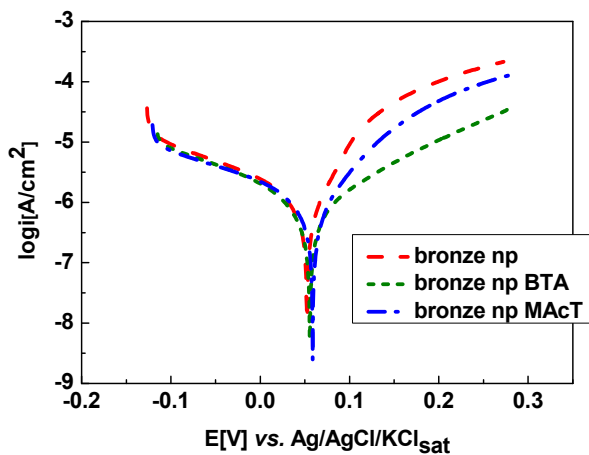
(a)



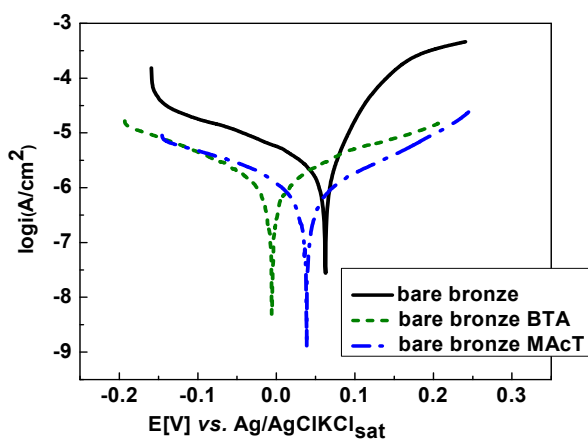
(b)

**Fig. 3.** Time variations of the open circuit potential (OCP) of the bronze screws exposed in the urban atmosphere of Cluj-Napoca, Romania, tested in 0.2 g / L  $\text{Na}_2\text{SO}_4$  + 0.2 g / L  $\text{NaHCO}_3$  (pH = 5) in the presence and absence of inhibitors, (a) – natural patina, (b) – bare bronze. In this figure “np” means natural patina.

The experiments started with measuring the open circuit potential of the bronze screws covered with natural patina, for a period of 3600 s, in the absence and in the presence of inhibitors, the results being presented in Fig. 3.



(a)



(b)

**Fig. 4.** The polarization curves ( $\pm 200$  mV vs. OCP) for the bronze screws exposed in the urban atmosphere of Cluj-Napoca, Romania, immersed in 0.2 g / L  $Na_2SO_4$  + 0.2 g / L  $NaHCO_3$  (pH = 5) in the presence and absence of inhibitors, a) - with natural patina, b) - bare bronze, scan rate, 10 mV / min. In this figure "np" means natural patina.

It can be observed that, in all cases, the OCP has positive values and the values recorded for the bronze screw covered with natural patina are more positive than that of bare bronze screw (Fig. 3a), suggesting an

ennoblement of the surface and, consequently, a braking of the anodic process (the metal dissolution). OCP values for bare bronze are more positive in the presence of MAcT than in its absence and more negative in the presence of BTA (Fig. 3b). In the last case, this could be due to interactions of the inhibitor with the cathodic depolarization reaction, in particular the reduction of  $O_2$ , which is diffusion-controlled.

To determine the polarization resistance of the electrodes, linear polarization curves were recorded, in the potential domain of  $\pm 20$  mV around the value of OCP. The polarization resistance values for each electrode, calculated as the inverse of the slope of each curve, are shown in Table 1.

As it can be observed, the natural patina increases only slightly the corrosion resistance of the bronze, due to the fact that the corrosion products layer is not nor continuous, neither compact. As expected, the highest value for  $R_p$  is noticed in the case of the bronze screw covered with natural patina, immersed in solution containing 0.2 g / L  $Na_2SO_4$  + 0.2 g / L  $NaHCO_3$  (pH = 5) in the presence BTA inhibitor, followed by the case when MAcT was present.

To determine the kinetic parameters of the corrosion process, polarization curves were recorded in the potential range of  $\pm 200$  mV vs. OCP (Fig. 4). The Tafel interpretation of the polarization curves led to the results presented in Table 1.

**Table 1.** Corrosion process parameters for the bronze screws exposed in the urban atmosphere of Cluj-Napoca, Romania, immersed in 0.2 g / L  $Na_2SO_4$  + 0.2 g / L  $NaHCO_3$  (pH = 5) in the presence and absence of inhibitors

Electrode	$E_{corr}$ [mV vs Ag/AgCl]	$i_{corr}$ [ $\mu A/cm^2$ ]	$\beta_a$ [mV/ decade]	$-\beta_c$ [mV/ decade]	$R_p$ [ $k\Omega cm^2$ ]
Bare bronze	62	0.71	44	162	2.98
Bronze with natural patina	52	0.81	49	117	2.77
Bronze with natural patina BTA	56	0.32	72	68	17.74
Bronze with natural patina MAcT	59	0.38	42	63	5.41
Bare bronze BTA	5	0.25	131	135	41.10
Bare bronze MAcT	39	0.14	112	108	139.22

$\beta_a$  and  $\beta_c$  are the Tafel coefficients

Analyzing the data in Table 1 it can be observed that, in the absence of inhibitors, the screw covered with natural patina has the lowest corrosion resistance ( $R_p=2.77$  [ $k\Omega cm^2$ ]), and the highest  $i_{corr}$  (0.81 [ $\mu A/cm^2$ ]), followed by the bare bronze sample.

### X-ray mapping of the screws surface covered with corrosion products

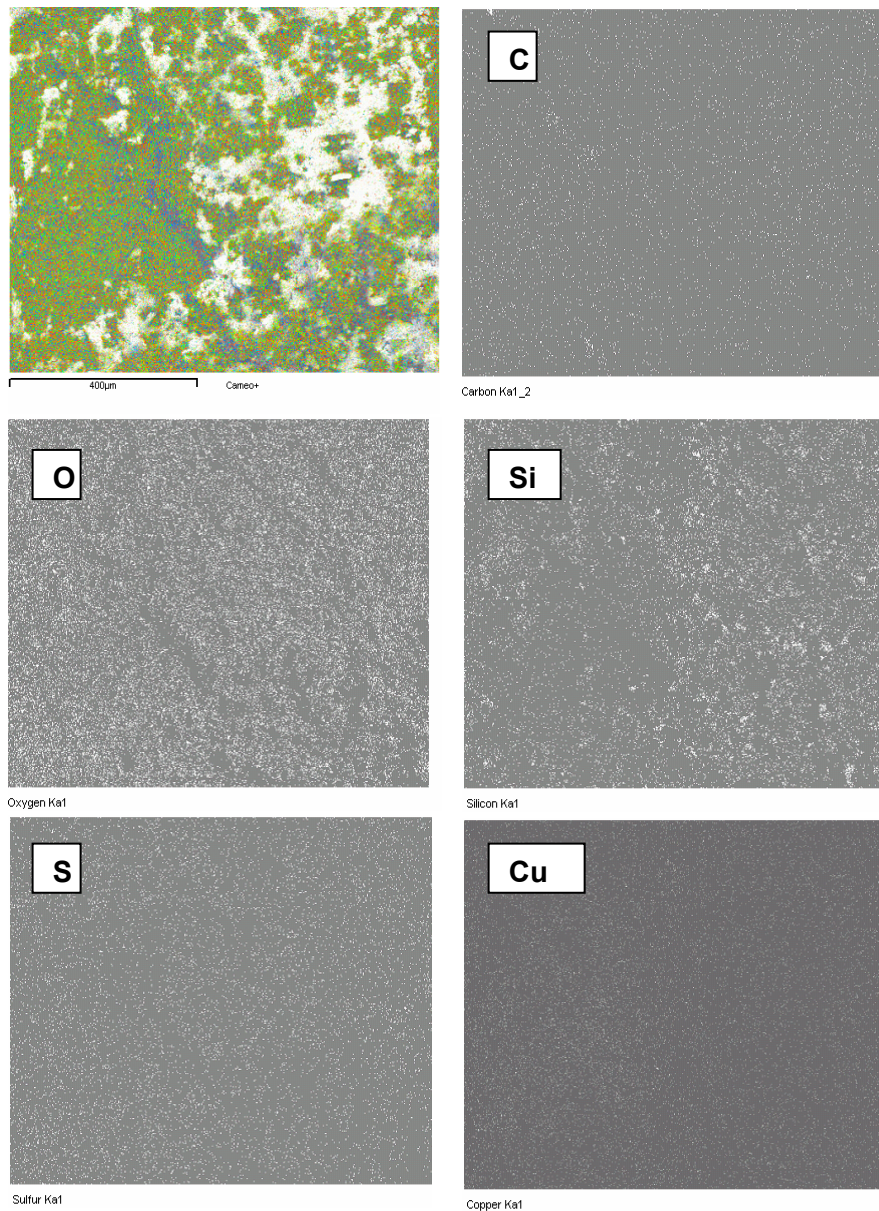


**Fig. 5.** Mapping results obtained on screw surface covered with natural patina.  
X-ray maps for C, O, Si, S, Cu

The lack of protection of the natural patina could be attributed to the advanced stage of degradation of the screw, with the appearance of intergranular corrosion. Also this behavior can be ascribed to the absence of tin compounds on the surface, which are usual in the case of Type II patinas [1] and which hinder the oxidation process of copper to Cu(I) oxide [18]. This is in accordance with the results obtained by SEM / EDX analysis reported elsewhere [19]. According to [19] the natural patina formed on screw surface is discontinuous, porous and has tendency to retain contaminant elements. It can be observed from Fig. 5 that the natural patina layer is not continuous nor homogeneous, fact confirmed by the absence of O and S in some areas (see X-Ray maps for O and S). Therefore the corrosion compounds such as brochantite  $[\text{Cu}_4(\text{SO}_4)(\text{OH})_6]$  which would protect the surface of the screw, are missing. On the other hand, X-ray mapping analysis indicates the presence of Si, confirming the ability of the natural patina to retain pollutants.

Bare screw has the highest corrosion resistance in the presence of inhibitor MACT. This is suggested by the high value of the polarization resistance ( $R_p=139.22$  [ $\text{k}\Omega\text{cm}^2$ ]) and the low value of the corrosion current density ( $i_{\text{corr}}=0.14$  [ $\mu\text{A}/\text{cm}^2$ ]).

Based on the corrosion current density ( $i_{\text{corr}}$ ) calculated from Tafel representation, the protection efficiency (PE) conferred by inhibitors can be determined using the following formula:

$$PE[\%] = \frac{(i_{\text{corr}})_{\text{without.inhibitor}} - (i_{\text{corr}})_{\text{inhibitor}}}{(i_{\text{corr}})_{\text{without.inhibitor}}} \times 100 \quad (1)$$

Another way of appreciation of inhibitor effectiveness is based on the variation of polarization resistance ( $R_p$ ), according to the relation:

$$PE[\%] = \frac{R_p_{\text{inhibitor}} - R_p_{\text{without.inhibitor}}}{R_p_{\text{inhibitor}}} \times 100 \quad (2)$$

The protection efficiencies of corrosion inhibitors for bronze screws calculated with formula 1 and 2 are depicted in Figure 6.

It is worth mentioning that, despite the differences between the values of PE, the variation tendency of inhibition efficiencies is the same for both methods.

It was observed that the best results were obtained in the case of bare bronze in presence of MACT (efficiency between 80 - 97 %). For bronze screw covered with natural patina the best results were in case of inhibitor BTA (efficiency between 55 - 83%). The rough surface of patinated bronze

along with its different adsorption properties toward the two organic compounds could explain this behavior. However, the relatively good efficiency of MACT especially for bare bronze surfaces and its non-toxic nature recommend it as possible substitute of BTA for bronze artifacts.

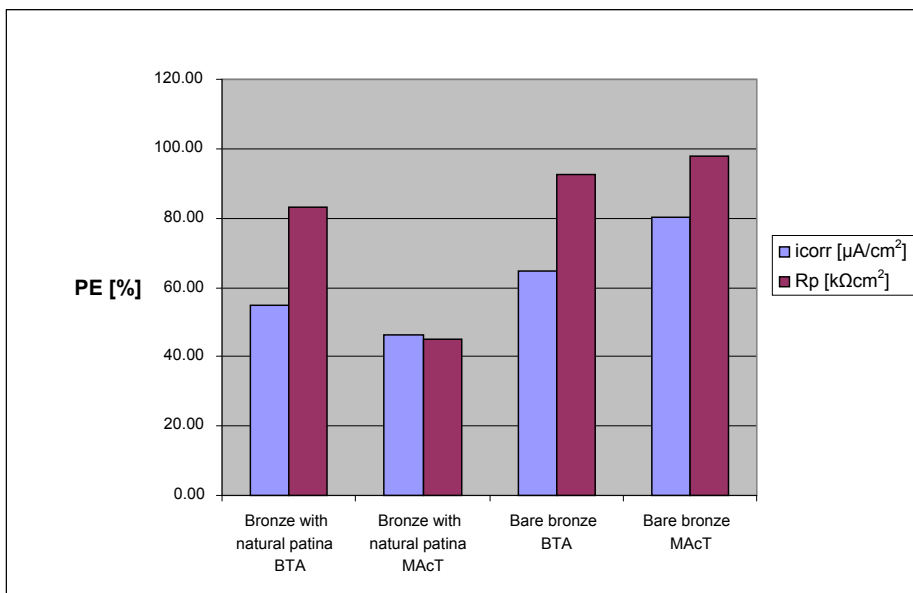


**Fig. 6.** Protection efficiency (PE) of inhibitors, calculated according to corrosion current density and polarization resistance.

## CONCLUSIONS

The corrosion of bronze screws used to assemble Matthias Rex statuary group, Cluj-Napoca, Romania was investigated, in the presence and absence of natural patina and of corrosion inhibitors in an attempt to improve bronze monuments protection against corrosion in urban atmospheric conditions.

Accelerated corrosion tests in an environment that simulated acid rain on bronze screw covered with a patina formed over 100 years, showed that the natural patina does not confer complete protection against corrosion to the bronze, due to its discontinuity.

The investigation indicates that both studied inhibitors provide protection to bronze monuments in the tested conditions. BTA showed best efficiency on patinated bronze, (65 - 92 %), while the best protection efficiency

on bare bronze was exerted by MAcT (80 - 97 %). The good efficiency of MAcT (even on patinated bronze) and its non-toxic nature recommend it as possible substitute of BTA for the protection of bronze monuments exposed to the atmosphere.

## EXPERIMENTAL

The bronze screws covered with natural patina, and cylindrically shaped were sampled during the restoration of the bronze statue of Mathias Rex in 2011. They were used as working electrodes during the corrosion measurements. The surface of the electrode exposed to the solution was disk - shaped, with a surface  $S = 3.14 \text{ cm}^2$ . The rest of the screw was isolated from the contact with the electrolyte by using a lacquer. For electrical contact, a metal wire was attached to the screw (Fig. 7).

The corrosion behavior of bronze screws covered with natural patina (Fig. 7a) in conditions that simulate acid rain was compared with that of a bronze screw without patina (Fig. 7b), obtained by cutting the original screw's head and by polishing it on emery paper and finally with alumina ( $\text{Al}_2\text{O}_3$ ), so that it did not present dents, goals, porosity, cracks, inclusions or other non-metallic impurities.

The study of the screws'surface was done by optical microscopy (OLIMPUS GS 51).

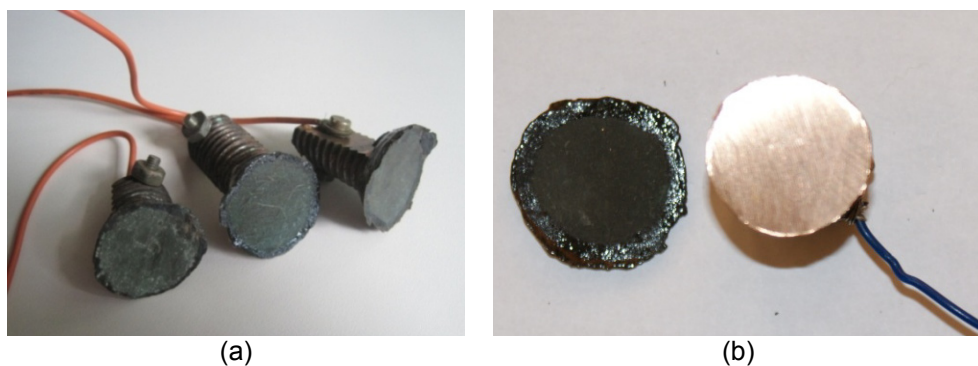


**Fig. 7.** Bronze screws used in the experiments: (a) with natural patina, (b) the original screw's head and the bare bronze screw.

The electrochemical corrosion measurements were performed on a PC - controlled electrochemical analyzer AUTOLAB - PGSTAT 10 (Eco Chemie BV, Utrecht, The Netherlands) using a three electrodes cell containing a working electrode (bronze screws), an Ag/AgCl electrode as reference

electrode and a platinum counter electrode. Anodic and cathodic polarization curves were recorded in a potential range of  $\pm 20$  mV and of  $\pm 200$  mV vs. the value of the open circuit potential, with a scan rate of 10 mV / min, after 1 hour immersion in corrosive solution.

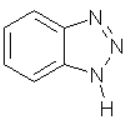
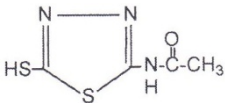
The chemical composition of bronze screws used for experiments was determined by X - ray fluorescence analysis (XRF). Analyses were performed using an installation type InnovX System Alpha Series with W anticathode, at 30 kV, 40  $\mu$ A, exposure time 60 seconds. SEM analysis were performed with a Scanning Jeol JEM5510LV (Japan) coupled with Oxford Instruments EDX Analysis System Inca 300 (UK) at 15kV and spot size 39  $\mu$ m.

## Reagents

The inhibitor used in the experiments was a non-toxic thiadiazole derivative, respectively 2 - mercapto - 5 acetylamino - 1, 3, 4 - thiadiazole (MAcT, from Sigma Aldrich) in a concentration of 1mM and the obtained results were compared with those recorded with benzotriazole (BTA) (Sigma Aldrich). The physical - chemical properties of the two compounds are presented in Table 2.

The electrolyte solution for corrosion measurements contained 0.2 g / L  $\text{Na}_2\text{SO}_4$  + 0.2 g / L  $\text{NaHCO}_3$  (pH = 5). All the other chemicals were of analytical grade and used as received.

**Table 2.** The physical-chemical characteristics of tested inhibitors

Inhibitor	Molecular formula	Molar mass [g/mol]	Melting point [°C]
BTA		$\text{C}_6\text{H}_5\text{N}_3$	119,12
MAcT		$\text{C}_3\text{H}_5\text{N}_3\text{OS}_2$	175,2

## ACKNOWLEDGEMENTS

The authors thank to Assoc. Prof. Dr. Eng. Ovidiu Nemeş from the Faculty of Materials and Environmental Engineering, Technical University of Cluj-Napoca, for microscopic images.

## REFERENCES

- [1]. L. Robbiola, J.M. Blengino, C. Fiaud, *Corrosion Science*, **1998**, *40*, 2083.
- [2]. M.C. Squarzialupi, G.P. Bernardini, V. Faso, A. Atrei, G. Rovida, *Journal of Cultural Heritage*, **2002**, *3*, 199.
- [3]. G.P. Cicileo, M.A. Crespo, B.M. Rosales, *Corrosion Science*, **2004**, *46*, 929.
- [4]. L. Robbiola, R. Portier, *Journal of Cultural Heritage*, **2006**, *7*, 1-12.
- [5]. K. Polikreti, V. Argyropoulos, D. Charalambous, A. Vossou, V. Perdikatsis, C. Apostolaki, *Corrosion Science*, **2009**, 2416-2422.
- [6]. C. Chiavari, K. Rahmouni, H. Takenouti, S. Joiret, P. Vermaut, L. Robbiola, *Electrochimica Acta*, **2007**, *52*, 7760.
- [7]. R. Picciochi, A.C. Ramos, M.H. Mendonça, I.T.E. Fonseca, *Journal of Applied Electrochemistry*, **2004**, *34*, 989.
- [8]. R.B. Faltermeier, *Studies in Conservation*, **1998**, *44*, 121.
- [9]. I. Ignat, S. Varvara, L. Muresan, *Studia Universitatis Babeş-Bolyai Chemia*, **2006**, *LI*, 127.
- [10]. L. Ying, F. Haitao, Z. Yifan, W. Wuji, *Journal of Materials Science*, **2003**, *38*, 407.
- [11]. O. Blajiev, A. Hubin, *Electrochimica Acta*, **2004**, *49*, 2761.
- [12]. E.-S.M. Sherif, *Applied Surface Science*, **2006**, *252*, 8615.
- [13]. E.-S.M. Sherif, S.-M. Park, *Corrosion Science*, **2006**, *48*, 4065.
- [14]. L. Valek, S. Martinez, *Materials Letters*, **2007**, *61*, 148.
- [15]. S. Varvara, L.M. Muresan, K. Rahmouni, H. Takenouti, *Corrosion Science*, **2008**, *50*, 2596.
- [16]. L. He, J. Liang, X. Zhao, B. Jiang, *Microchemical Journal*, **2011**, *99*, 203-212.
- [17]. David A. Scott, *Metallography and Microstructure of Ancient and Historic Metals*, The Getty Conservation Institute in association with Archetype Books, Singapore, **1991**.
- [18]. D. Šatović, Valek Žulj, V. Desnica, S. Fazinić, S. Martinez, *Corrosion Science*, **2009**, *51*, 1596.
- [19]. J.D. Chelaru, L.M. Mureşan, V.F. Soporan, O. Nemeş, L. Barbu-Tudoran, *Journal of Cultural Heritage*, **2013**, DOI: 10.1016/j.culher.2013.11.005.

## TOPOLOGICAL SYMMETRY OF MULTI-SHELL ICOSAHEDRAL CLUSTERS

ATENA PARVAN-MOLDOVAN<sup>a</sup>,  
FATEMEH KOOREPAZAN-MOFTAKHAR<sup>b</sup> AND MIRCEA V. DIUDEA<sup>a\*</sup>

**ABSTRACT.** Topological symmetry is referred to the maximum possible symmetry achievable by a given molecular structure; it can be performed either by permutations on the adjacency matrix or by calculating the values of some topological indices. The equivalence classes of vertices/atoms of the multi-shell nanostructures under study were solved by using a topological index computed on the layer matrix of atom surrounding rings and compared with the results of matrix permutation. A centrality order of vertices in multi-shell clusters is given. The design of nanostructures was performed by map operations as implemented in our original CVNET and Nano Studio software programs.

**Keywords:** *Multi-shell cage, centrality index, vertex equivalence class, automorphism.*

### INTRODUCTION

Molecular structures show various types of geometrical symmetry [1-4]. Geometrical symmetry is reflected in several molecular properties, which are dependent on the spatial structure of molecules. Molecular topology reveals a *topological symmetry* (*i.e.*, constitutional symmetry), defined in terms of *connectivity* and expresses equivalence relationships among elements of graph: vertices, bonds, faces or larger subgraphs.

Using the notions of the Group action [3], in which every element of the group acts like as a one-to-one mapping, the group  $G$  is said to act on a set  $X$  when there is a function  $\phi$  such that  $\phi: G \times X \longrightarrow X$  and for any element  $x \in X$ ,

---

<sup>a</sup> Department of Chemistry, Faculty of Chemistry and Chemical Engineering, Babes-Bolyai University, 400028 Cluj-Napoca, Romania

<sup>b</sup> Department of Mathematics, Faculty of Mathematical Sciences, University of Kashan, Kashan 87317-51167, I. R. Iran

\* Corresponding author: diudea@chem.ubbcluj.ro

there exists:  $\phi(g, \phi(h, x)) = \phi(gh, x)$ , for all  $g, h \in G$ , with  $\phi(e, x) = x$ ,  $e$  being the identity element of  $G$ . The mapping  $\phi$  is called a group action while the set  $\{\phi(gx) \mid g \in G\}$  is called the *orbit* of  $x$ . For a permutation  $\sigma$  on  $n$  objects, the permutation matrix is an  $n \times n$  matrix  $P_\sigma$ , with elements  $x_{ij} = 1$  if  $i = \sigma(j)$  and 0 otherwise. For any permutation  $\sigma$  and  $\tau$  on  $n$  objects,  $P_\sigma P_\tau = P_{\sigma\tau}$ , while the set of all permutation matrices is a group isomorphic to the symmetry group  $S_n$  on  $n$  symbols. A permutation  $\sigma$  of the vertices of a graph  $H(V, E)$  ( $V$  being the set of vertices and  $E$  the set of edges in  $H$ ) belongs to an automorphism group  $G$  if one satisfies  $P_\sigma^t A P_\sigma = A$ , where  $A$  is the adjacency matrix of the graph  $H$ . Given  $Aut(H) = \{\sigma_1, \dots, \sigma_m\}$ , the matrix  $S_G = [s_{ij}]$ , where  $s_{ij} = \sigma_i(j)$  is called a solution matrix for  $H$  and its calculation will provide the automorphism group of  $H$ .

Given a graph  $H(V, E)$  and the automorphism group  $Aut(H)$ , two vertices,  $i, j \in V$  are called *equivalent* if  $\{\phi(ij) \mid i, j \in Aut(H)\}$ , in other words, they belong to the same orbit of automorphisms.

Suppose  $v_1, v_2, \dots, v_m$  are  $m$  disjoint *automorphic partitions* of the set of vertices  $V(H)$ , then:  $V = V_{v_1} \cup V_{v_2} \cup \dots \cup V_{v_m}$  and  $V_{v_i} \cap V_{v_j} = \emptyset$ .

Let now consider a vertex invariant,  $In = In_1, In_2, \dots, In_m$ , which assigns a value  $In_i$  to the vertex  $i$ . Two vertices  $i$  and  $j$  of a molecular graph (with vertices meaning the atoms and edges the bonds in the molecule) belong to the same *invariant class IC* if  $In_i = In_j$ . The partitioning in *classes of vertices/atoms* leads to  $m$  classes, with  $v_1, v_2, \dots, v_m$  atoms in each class; such a partitioning may differ from the *orbits of automorphism* i.e. *classes of equivalence*, since no vertex invariant is known so far to always discriminate two non-equivalent vertices in any graph. The classes of vertices are eventually *ordered* according to some rules.

A given binary relation  $\sim$  on a set  $A$  is said to be an *equivalence relation* if and only if it is: reflexive ( $x \sim x$ ); symmetric ( $x \sim y \Rightarrow y \sim x$ ) and transitive ( $x \sim y$  and  $y \sim z \Rightarrow x \sim z$ ).

It is worthy to mention that topological symmetry equals the maximum geometrical symmetry a molecular graph can have.

A layer matrix [5] is built up on a layer partition of a vertex  $i$  in the graph  $G(V, E)$ :

$$G(i) = \{G(i)_j, j \in [0, ecc_i] \text{ and } v \in G(i)_j \Leftrightarrow d_{iv} = j\}$$

where  $ecc_i$  is the eccentricity of  $i$  (i.e., the largest distance from  $i$  to the other vertices of  $G$ ). The entries in a layer matrix, **LM**, collect the vertex property  $p_v$  (a topological, chemical, or physical property) for all the vertices  $v$  belonging to the layer  $G(i)_j$ :

$$[\mathbf{LM}]_{ij} = \sum_{v \in G(i)_j} p_v,$$

for vertices located at distance  $j$  from vertex  $i$ . The matrix **LM** is defined as

$$\mathbf{LM}(G) = \{ [\mathbf{LM}]_{ij}; i \in V(G); j \in [0, d(G)] \}$$

where  $d(G)$  is the diameter of the graph. The dimensions of the matrix is  $N \times (d(G)+1)$ ; the zero-distance column is just the column of vertex properties. The most simple and essential layer matrix is the *counting* property (i.e., the existence of a vertex in a given position  $l$  at a given distance is counted by 1, and zero, otherwise). In the following, as a property, the count of rings  $R$  around each vertex is considered, the layer matrix being  $\mathbf{LR}$ .

Layer matrices are used to derive the indices of *centrality*  $C(\mathbf{LM})$ , that quantify the centrality of vertices and finally the inside centrality of a graph

$$C(\mathbf{LM})_i = \left[ \sum_{k=1}^{ecc_i} ([\mathbf{LM}]_{ik}^{2k})^{1/(ecc_i)^2} \right]^{-1}$$

where  $ecc_i$  is the eccentricity of  $i$ .

## RESULTS AND DISCUSSION

### Design of multi-shell cages

The cages under study represent 3D-tessellations, recently developed by Diudea [1], achieved by map operations [6-8], as implemented by the original software CVNET [9].

In building the cluster  $C_{750}$ , the sequence of operations is as follows:  $\text{TRS}(P_4(C_{60}))_{330}; S_2(C_{60})_{420}; \text{TRS}(P_4(C_{60}))@S_2(C_{60})_{750}$  (Figure 1).

The structure  $\text{TRS}(P_4(C_{60}))@S_2(C_{60})_{750} = C_{60}((C_{20})_{60})_{750}$  is a "spongy" one, with the central hollow of exact topology of  $\text{TRS}(P_4(C_{60}))_{330}$ . It is a  $C_{20}$ -tessellation: formally, every point in the graph of  $C_{60}(I_h)$  is changed by a cage  $C_{20}$ ; notation  $C_{60}((C_{20})_{60})$  means  $60 \times (C_{20})$  within the topology of  $C_{60}(I_h)$ . The joining of the two halves was made by our original software Nano Studio [10].

Cluster  $C_{408}$  was made by all-point truncation of the Diudea's cluster  $\text{Tr}(\text{Diu}_{45})_{408}$ , where  $\text{Diu}_{45} = (\text{IcoP}@(\text{IcoP}_{12}))_{45}$ . It is the intersection of  $12 \times \text{Tr}(\text{IcoP})_{84}$  (related to Samson's cluster<sub>104</sub>), the core being the  $13^{\text{ne}}\text{Tr}(\text{IcoP})_{84}$  (Figure 2).

### Topological symmetry

Topological symmetry is referred to the maximum possible symmetry achievable by a given molecular structure; it can be performed either by permutations on the adjacency matrix [1-3] or by calculating the value of some topological indices [1-4]. In the following tables, the equivalence classes of vertices/atoms are presented in their descending centrality, calculated on the layer matrix of surrounding rings RL. The atom type, eg.  $3^3 3.5^2 6^4$  reads:  $R_3 \times 3; R_5 \times 2; R_6 \times 4$ ,  $R_3$  being a triangle,  $R_5$  a pentagon and  $R_6$  a hexagon.

The symmetry for the icosahedral structures in Figures 1 and 2 was computed by the GAP software program as being

$$C_2 \times A_5 = I_h; |I_h| = 120.$$

It confirmed the equivalence class established by the centrality index (Tables 1 and 2).

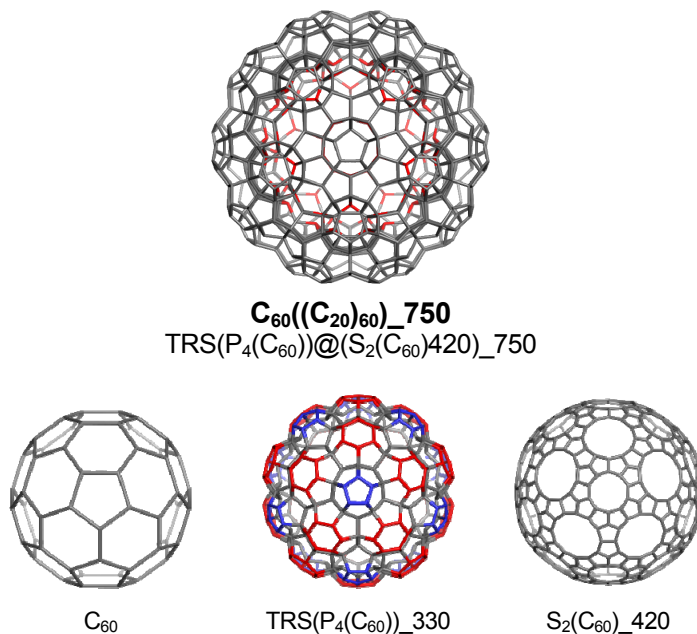
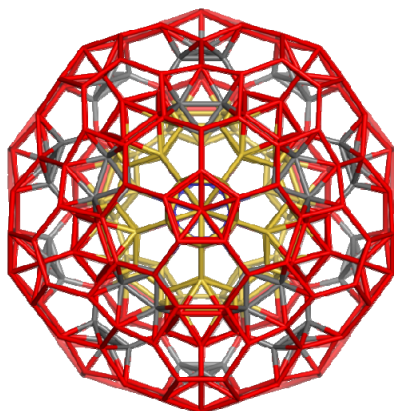


**Figure 1.**  $C_{750}$  and its substructures

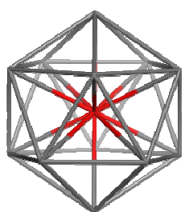
**Table 1.**  $C_{750}$ : Automorphism group =  $C_2 \times A_5 = I_h; |I_h| = 120$  (cf. GAP permutations). Equivalence classes of atoms in the descending order of their centrality cf. LR matrix.

Class	Centrality signature	No. Elements	Vertex degree	Atom type
1	0.0425537487829127	60	4	$5^5$
2	0.0425405656366799	30	4	$5^5$
3	0.0408741428983785	60	3	$5^3$
4	0.0403249632533878	60	4	$5^6$
5	0.0403215210989583	60	4	$5^5.6$
6	0.0403184110690464	60	4	$5^5.6$
7	0.0380980964599947	60	4	$5^5$
8	0.0380776127196794	60	4	$5^5$
9	0.0380525586272046	60	4	$5^5$
10	0.0363966020960237	60	3	$5^3$
11	0.0363899446618803	60	3	$5^3$
12	0.0363398403991418	120	3	$5^3$

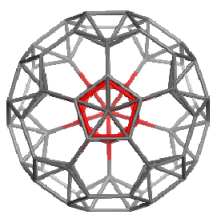


**Tr(IcoP)84@((Tr(IcoP)84)<sub>12</sub>\_408**

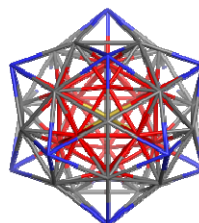
(Ico@(TT<sub>20</sub>)@(Ico<sub>12</sub>;TT<sub>20</sub>;TT<sub>30</sub>)@(Py<sub>5</sub>;TT<sub>5</sub>)<sub>12</sub>\_408  
Tr(Diu45)\_408



IcoP\_13



Tr(IcoP)\_84



Diu\_45=IcoP@IcoP12\_45

**Figure 2.** C<sub>408</sub> and its substructures

**Table 2.** C<sub>408</sub>: Automorphism group = C<sub>2</sub> × A<sub>5</sub> = I<sub>h</sub>; |h| = 120 (cf. GAP permutations). Equivalence classes of atoms in the descending order of their centrality cf. LR matrix.

Class	Centrality signature	No. Elements	Vertex degree	Atom type
1	0.0825432266953615	12	6	3 <sup>5</sup> .5 <sup>5</sup> .6 <sup>5</sup>
2	0.0723127280340924	12	6	3 <sup>5</sup> .5 <sup>5</sup> .6 <sup>5</sup>
3	0.064639289864084	60	6	3 <sup>5</sup> .5 <sup>5</sup> .6 <sup>5</sup>
4	0.0580357622307322	60	6	3 <sup>5</sup> .5 <sup>5</sup> .6 <sup>5</sup>
5	0.0572358681133143	12	6	3 <sup>5</sup> .5 <sup>5</sup> .6 <sup>5</sup>
6	0.0564467194639707	60	6	3 <sup>5</sup> .5 <sup>2</sup> .6 <sup>5</sup>
7	0.0552836553218085	60	5	3 <sup>3</sup> .5 <sup>2</sup> .6 <sup>4</sup>
8	0.0512081941907237	12	6	3 <sup>5</sup> .6 <sup>5</sup>
9	0.0505895569851173	60	4	3 <sup>2</sup> .5.6 <sup>3</sup>
10	0.0467456474901417	60	4	3 <sup>2</sup> .5.6 <sup>3</sup>

## COMPUTATIONAL DETAILS

The multi-shell cages  $C_{750}$  and  $C_{408}$ , Figure 1, were built up on computer by using CVNET [9] software program and their topology analysed. The vertices were partitioned in classes function of the surrounding rings and then by their centrality index. The calculations were made by Nano-Studio [10]. The automorphism data for both these structures were calculated by the GAP (Groups, Algorithms and Programming) program.

## CONCLUSION

Classes of equivalence of vertices/atoms of the multi-shell icosahedral nanostructures were solved by using the Centrality topological index, computed on the layer matrix of all rings around atoms and confirmed by the results of matrix permutation. Future work will analyze the equivalence classes of edges/ bonds and faces/rings by transforming the actual cages in their medial and dual graphs, respectively.

## ACKNOWLEDGMENTS

The work was supported by the Romanian CNCSIS-UEFISCSU project, PN-II IDEI 129/2010, PN-II-ID-PCE-2011-3-0346.

## REFERENCES

- [1]. M. Diudea, in *Diamond and Related Nanostructures*, eds. M.V. Diudea and C.L. Nagy, Diamond and Related Nanostructures, Springer, Dordrecht, **2013**, Chap.19, p. 335.
- [2]. A.R. Ashrafi, F. Kooperazan-Moftakhar, M.V. Diudea, M. Stefu, in: M.V. Diudea, C.L. Nagy, Eds., *Diamond and Related Nanostructures*, Springer, Dordrecht, **2013**, Chap. 18, p. 321.
- [3]. Hungerford, Thomas W. *Algebra*. Reprint of the 1974 original. Graduate Texts in Mathematics, 73. Springer-Verlag, New York-Berlin, **1980**.
- [4]. M.V. Diudea and C.L. Nagy, *Periodic Nanostructures*, Springer, Dordrecht, **2007**.
- [5]. M.V. Diudea and O. Ursu, Layer matrices and distance property descriptors, *Indian J. Chem. A*, **2003**, *42*, 1283.
- [6]. M.V. Diudea, M. Stefu, P.E. John and A. Graovac, Generalized operations on maps, *Croat. Chem. Acta*, **2006**, *79*, 355.
- [7]. M.V. Diudea, Nanoporous Carbon Allotropes by Septupling Map Operations, *J. Chem. Inf. Model.*, **2005**, *45*, 1002.
- [8]. M.V. Diudea, Capra-a leapfrog related operation on maps, *Studia UBB Chemia*, **2003**, *48* (2), 3.
- [9]. M. Stefu and M.V. Diudea, CageVersatile\_CVNET, Babes-Bolyai Univ. Cluj, **2005**.
- [10]. Cs.L. Nagy, M.V. Diudea, NANO-Studio, Babes-Bolyai Univ. Cluj, **2009**.

## INVESTIGATION OF DNA BINDING AND CLEAVAGE ACTIVITIES OF BORON COMPLEXES IN THE PRESENCE OF HYDROGEN PEROXIDE

ALPARSLAN KADİR DEVRİM<sup>a</sup>, ALİ ARSLANTAS<sup>b,\*</sup>,  
MERT SUDAGIDAN<sup>c</sup>, DURSUN ALİ KÖSE<sup>d</sup>, BİRGÜL KARAN<sup>e</sup>

**ABSTRACT.** Magnesium [di(hydroxy)mono(citratoborate)]dihydrate ( $\text{Mg}[\text{B}(\text{Cit})(\text{OH})_2]_2 \cdot 2\text{H}_2\text{O}$ ), Lithium [di(hydroxy)mono(citratoborate)]hydrate  $\text{Li}[\text{B}(\text{Cit})(\text{OH})_2] \cdot \text{H}_2\text{O}$ , Sodium [di(hydroxy)mono(salicylato) borate]hydrate  $\text{Na}[\text{B}(\text{Sal})(\text{OH})_2] \cdot \text{H}_2\text{O}$  and Magnesium[bis(salicylatoborate)]decahydrate  $\text{Mg}[\text{B}(\text{Sal})_2]_2 \cdot 10\text{H}_2\text{O}$  complexes have been synthesized and characterized. The cattle genomic DNA (CG-DNA) interaction of the complexes was studied by spectroscopic methods, viscosity, and electrophoresis measurements. The complexes partially intercalated to CG-DNA. Furthermore, DNA cleavage activity of these complexes was also investigated using agarose gel electrophoresis and the complexes show moderate ability of cleavage to the DNA.

**Keywords:** Boron complexes, DNA-binding cleavage, DNA cleavage

### INTRODUCTION

Cancer is still most common cause of death and may grow into the most common disease in the future in spite of remarkable therapeutic achievements [1]. Thereby, the discovery and development of new therapeutic agents have a crucial importance. Drug researches propose that a lot of anticancer, antiviral and antiseptic compounds act through binding to DNA [2–4], because the interaction between small molecules and DNA can usually

---

<sup>a</sup> Department of Biochemistry, Faculty of Veterinary Medicine, Mehmet Akif Ersoy University, 15030 Burdur, Turkey

<sup>b</sup> Department of Biomedical Engineering, Karabuk University, 78050 Karabuk, Turkey

<sup>c</sup> Scientific and Technology Application and Research Center, Mehmet Akif Ersoy University, 15030 Burdur, Turkey

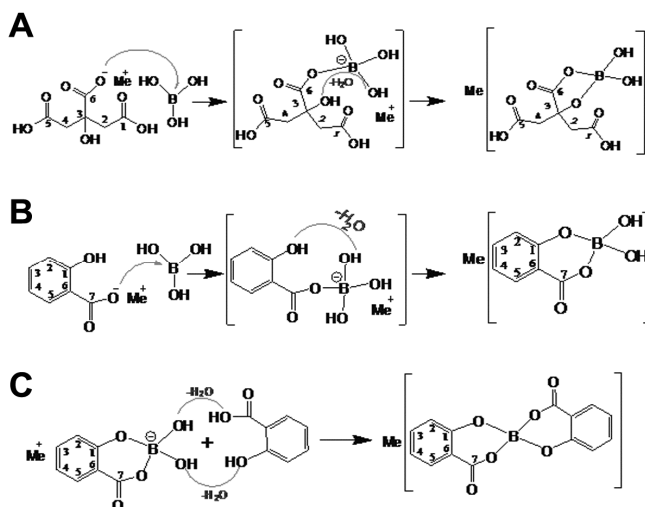
<sup>d</sup> Department of Chemistry, Hitit University, 19040 Corum, Turkey

<sup>e</sup> Department of Chemistry, Hacettepe University, 06532 Ankara, Turkey

\* Corresponding Author: [aliarslantas@karabuk.edu.tr](mailto:aliarslantas@karabuk.edu.tr)

cause DNA damage in cancer cells, blocking cell division and resulting in cell death [5–7]. Compounds can interact non-covalently with DNA by intercalation, groove binding or external electrostatic binding [8]. Many significant applications of the compounds demand that they could attach to DNA in an intercalative mode [9].

Boron complexes of inorganic and organic molecules have important pharmacological properties, such as hypolipidemic, anti-inflammatory, anti-osteoporosis, and antineoplastic activities [10, 11]. Nowadays, there is interest in the synthesis of boron complexes with potential use for the treatment of some types of malignant cancers, such as melanoma and glioblastoma multiform brain tumors [12]. The synthesis of boron complexes of biomolecules like amino acids, peptides, nucleosides is one of the main fields of cancer research [13]. Actions of boron molecule include arthritis alleviation, bone growth and maintenance of central nervous system function, hormone facilitation, immune response, inflammation, and oxidative stress modulation were previously reported [14]. There is a significant literature supporting the application of artificial DNA binding and cleaving agents in biotechnology. Compounds showing the properties of effective binding as well as cleaving double stranded DNA under physiological conditions are of great importance since these could be used as diagnostic agents in medicinal and genomic research. Therefore, it is obvious that the nature of the ligand plays significant roles in their interaction with DNA [15–19].



**Scheme 1.** (A) Proposed complexation mechanism of boric acid with citric acid, Me=Mg or Li, (B) Proposed mechanism for the complexation of boric acid with salicylic acid, Me=Na, (C) Me=Mg.

In this study, DNA binding and interaction activities of synthesized [20] complex 1 ( $\text{Mg}[\text{B}(\text{Cit})(\text{OH})_2]_2 \cdot 2\text{H}_2\text{O}$ ) (Scheme 1A.), complex 2 ( $\text{Li}[\text{B}(\text{Cit})(\text{OH})_2] \cdot \text{H}_2\text{O}$ ) (Scheme 1A.), complex 3 ( $\text{Na}[\text{B}(\text{Sal})(\text{OH})_2] \cdot \text{H}_2\text{O}$ ) (Scheme 1B.) and complex 4 ( $\text{Mg}[\text{B}(\text{Sal})_2]_2 \cdot 10\text{H}_2\text{O}$ ) (Scheme 1C.) were investigated with the cattle genomic DNA (CG-DNA) to demonstrate their ability to bind and cleave the DNA [21] by UV absorption, agarose gel electrophoresis, and viscosity measurement methods.

## RESULTS AND DISCUSSION

### DNA Binding and Electronic Absorption Spectra

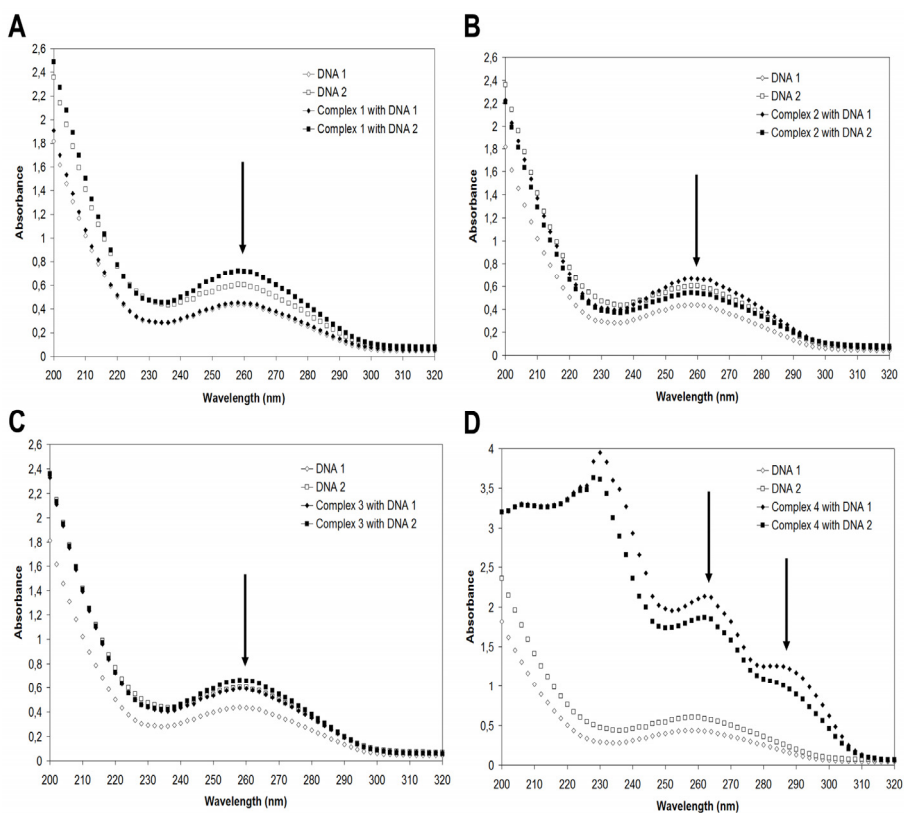


**Figure 1.** (A) Electronic absorption spectra of complex 1 (100  $\mu\text{M}$ ), (B) complex 2 (100  $\mu\text{M}$ ), (C) complex 3 (100  $\mu\text{M}$ ) and (D) complex 4 (100  $\mu\text{M}$ ) in the absence and presence of increasing amounts of the cattle genomic DNA (CG-DNA) (DNA 1 (11.25  $\mu\text{g}$ ) and DNA 2 (22.50  $\mu\text{g}$ ). Arrows show the changes in absorbance with respect to an increase in the DNA concentration

The absorption spectra of CG-DNA in the absence and presence of the complexes are shown in Fig. 1A-D. On the addition of CG-DNA, hypo and hyperchromism effect were observed. The absorption bands of  $\text{Mg}[\text{B}(\text{Cit})(\text{OH})_2]_2 \cdot 2\text{H}_2\text{O}$ ,  $\text{Li}[\text{B}(\text{Cit})(\text{OH})_2] \cdot \text{H}_2\text{O}$ ,  $\text{Na}[\text{B}(\text{Sal})(\text{OH})_2] \cdot \text{H}_2\text{O}$  and  $\text{Mg}[\text{B}(\text{Sal})_2]_2 \cdot 10\text{H}_2\text{O}$  complexes at around 260 nm show hypochromism. In fact, the hypochromic impact, characteristic of intercalation, is generally connected to the interaction between the electronic states of the complexes and those of DNA bases [22, 23]. The observed spectroscopic shifts suggest that the complex molecules have interaction with DNA.

### DNA Cleavage Activities

The interaction of the cattle genomic DNA (CG-DNA) with  $\text{Mg}[\text{B}(\text{Cit})(\text{OH})_2]_2 \cdot 2\text{H}_2\text{O}$ ,  $\text{Li}[\text{B}(\text{Cit})(\text{OH})_2] \cdot \text{H}_2\text{O}$ ,  $\text{Na}[\text{B}(\text{Sal})(\text{OH})_2] \cdot \text{H}_2\text{O}$  and  $\text{Mg}[\text{B}(\text{Sal})_2]_2 \cdot 10\text{H}_2\text{O}$  complexes was investigated in order to specify the DNA cleavage efficiencies of these complexes. The aim was succeeded by observing through agarose gel electrophoresis of CG-DNA. After 3 h incubation at 37 °C, in the concentration range of 5, 0.5, 0.05 mM complexes, the results of the experiments implemented and DNA bands are shown in Fig. 2.

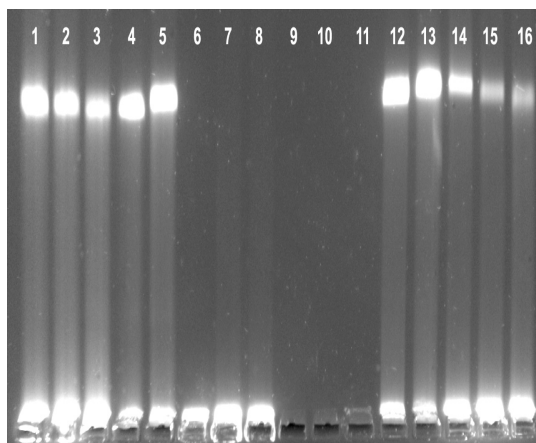


**Figure 2.** DNA cleavage by the complexes 1, 2, 3, and 4 obtained using agarose gel electrophoresis. The chemical activity of the cattle genomic DNA (CG-DNA) incubated at 37 °C for 3 h with varied concentrations of the complexes in the presence of  $\text{H}_2\text{O}_2$  as an oxidizing agent: lane 1, 2, and 3, CG-DNA +  $\text{H}_2\text{O}_2$  (60 mM) + complex 1 (5, 0.5 and 0.05 mM); lane 4, control CG-DNA; lane 5, CG-DNA +  $\text{H}_2\text{O}_2$  (60 mM); lane 6, 7 and 8, CG-DNA +  $\text{H}_2\text{O}_2$  (60 mM) + complex 2 (5, 0.5 and 0.05 mM); lane 9, 10, and 11, CG-DNA +  $\text{H}_2\text{O}_2$  (60 mM) + complex 3 (5, 0.5 and 0.05 mM); lane 12, control CG-DNA; lane 13, CG-DNA +  $\text{H}_2\text{O}_2$  (60 mM); lane 14, 15 and 16, CG-DNA +  $\text{H}_2\text{O}_2$  (60 mM) + complex 4 (5, 0.5 and 0.05 mM)

Nevertheless, a raise in concentration of the complexes resulted in increased DNA cleavage. It was found that complex 1 and 4 have a moderate DNA cleavage ability than either complex 2 and 3. The results show that complex 2 almost can slightly promote DNA cleavage at given complex concentrations and complex 3 has the most cleavage activity than other three complexes because DNA bands disappeared completely in the presence of complex 3 (Fig. 2 lanes 9–11). The complexes 1, 2, 3 and 4 show cleavage potential because of the increased reaction of complexes with  $H_2O_2$ , thereby creating hydroxyl radicals or molecular oxygen, both of which have ability of damaging DNA [24, 25].

### Viscosity Experiments

Optical photophysical studies give important, but not provide enough evidence to promote a binding model. The complexes bind particularly in DNA grooves with partial non-classical intercalation, under the same conditions, generally lead to negative or no shift in DNA solution viscosity [26, 27]. In order to verify the binding mode of the complexes 1, 2, 3 and 4 with CG-DNA, the viscosity measurements of the complexes with CG-DNA were carried out by varying the concentration of complexes. The effect of  $Mg[B(Cit)(OH)_2]_2 \cdot 2H_2O$ ,  $Li[B(Cit)(OH)_2] \cdot H_2O$ ,  $Na[B(Sal)(OH)_2] \cdot H_2O$  and  $Mg[B(Sal)_2]_2 \cdot 10H_2O$  complexes on the viscosity of DNA is shown in Fig. 3.

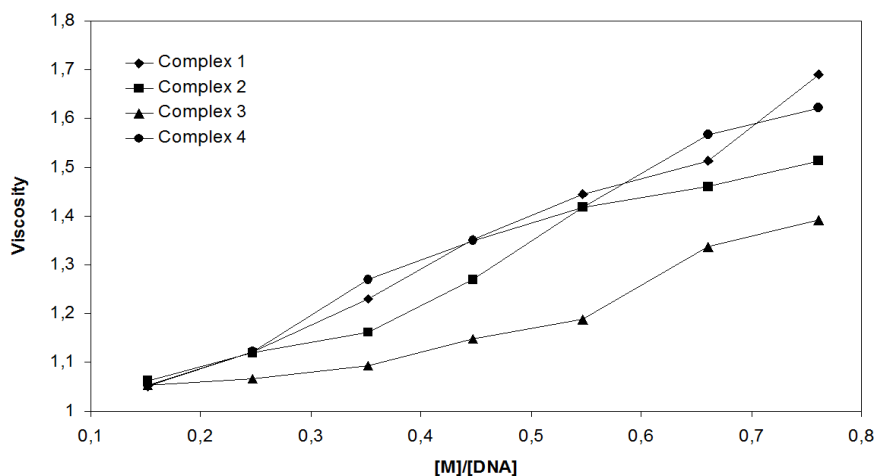


**Figure 3.** Effect of increasing concentrations of the complexes on the relative viscosity of CG-DNA at 25 °C

The results of viscosity measurements obviously show that all complexes have an intercalative interaction between next to DNA base pairs and it led to an extension in the DNA helix and also increased the viscosity of DNA with a raising concentration of the complexes. The viscosity of DNA is slightly increased with the increase of the concentration of the complexes 1, 2, 3 and 4, in contrast to that of proven DNA intercalator ethidium bromide (EtBr). Based upon all the spectroscopic studies together with the viscosity measurements, it was found that the boron complexes can bind to CG-DNA through an intercalative interaction.

## CONCLUSIONS

In conclusion, the citric acid and salicylic acid-based ligands and their boron (boric acid) complexes have been prepared and fully characterized. In agreement with UV-Vis absorption and viscosity measurements, there is an intercalative interaction between the complexes and CG-DNA. DNA cleavage studies reveal that entire four complexes have the capability to cleave the DNA.

## EXPERIMENTAL SECTION

### *Synthesis of Mg[B(Cit)(OH)<sub>2</sub>]<sub>2</sub>·2H<sub>2</sub>O, Li[B(Cit)(OH)<sub>2</sub>]<sub>2</sub>·H<sub>2</sub>O complexes*

The molecular structure of citric acid provides various coordination sites for complex formation with metals. Controlling the molar ratios, mono-chelate complexes were prepared in this work. As for the *bis*-chelate complexes, binding of citrate ligands was suggested to occur through the carboxylate group and the nearest OH group forming five-membered rings. Mono- and bis-chelates of citric acid with boron were prepared in salt form with Mg and Li ions. The compounds were obtained as crystallites and found to be stable at room conditions. The compositions and melting points of the products are summarized in Table 1 [20].

**Table 1.** Chemical compositions<sup>a</sup> and melting points of citrate-borate complexes

Compound	M.p.(°C)	C(%)	H(%)	H <sub>2</sub> O(%)
Citric acid	153	37.46(37.48)	4.14(4.17)	-
Li[B(Cit)(OH) <sub>2</sub> ] <sub>2</sub> ·H <sub>2</sub> O	95	32.14(31.89)	3.54(4.13)	7.50(8.00)
Mg[B(Cit)(OH) <sub>2</sub> ] <sub>2</sub> ·2H <sub>2</sub> O	115	27.49(27.63)	4.42(4.60)	7.80(7.00)

<sup>a</sup> Calculated in parentheses (Cit=C<sub>6</sub>H<sub>6</sub>O<sub>7</sub>)

### FTIR Spectra of Boric acid Complexes with Citric Acid

FTIR spectral data of boric acid-citrate complexes are given in Table 2. In the spectra of the complexes, in addition to the -OH stretching vibrations of the acidic, alcoholic groups and water molecules at 3600-3200  $\text{cm}^{-1}$ ,  $\nu_a(\text{C}=\text{O})$  of non ionized carboxylic acid groups ( $\approx 1740 \text{ cm}^{-1}$ );  $\nu_a(\text{COO})$  ( $\approx 1590 \text{ cm}^{-1}$ ) and  $\nu_s(\text{COO})$  ( $1350 \text{ cm}^{-1}$ ) of carboxylate groups were observed. Asymmetric B-O vibrations were observed around 1100  $\text{cm}^{-1}$  and the specific tetrahedral B-O band appeared in the range of 825  $\text{cm}^{-1}$ – 784  $\text{cm}^{-1}$  [20].

**Table 2.** summary of the FT-IR spectral data of citric acid-borate complexes

Compound	$\nu(\text{O-H})$	$\nu_a(\text{C}=\text{O})$	$\nu_a\text{COO}$	$\nu_s\text{COO}$	$\nu_a(\text{B-O})/\text{BO}_4$ & $\nu(\text{C-O})$	$\nu_s(\text{B-O})/\text{BO}_4$
Citric acid	3496, 3293	1739, 1686	–	–	1252	–
Borax	~3300	–	–	–	1220	834,815 doublet
Li[B(Cit)(OH) <sub>2</sub> ].H <sub>2</sub> O	3503	1715	1597	1347	1111, 1060	835, 787
Mg[B(Cit)(OH) <sub>2</sub> ] <sub>2</sub> .2H <sub>2</sub> O	3429	1728	1571	1356	1110, 1073	820, 776

### Synthesis of Na[B(Sal)(OH)<sub>2</sub>].H<sub>2</sub>O and Mg[B(Sal)<sub>2</sub>]<sub>2</sub>.10H<sub>2</sub>O complexes

Mono- and bis-chelates of salicylic acid with boron were prepared in salt form with Na and Mg ions. The compounds were obtained as white crystallites and found to be stable at room conditions. X-ray quality crystals were obtained only for the 1:1 complex with Na and for the 1:2 complex with Mg. The compositions and melting points of the products are summarized in Table 3 [20].

**Table 3.** Chemical compositions<sup>a</sup> and melting points of salicylic acid-borate complexes

Compound	M.p.(°C)	C(%)	H(%)	H <sub>2</sub> O(%)
Na[B(Sal)(OH) <sub>2</sub> ].H <sub>2</sub> O	140	38.44(37.83)	3.75(3.60)	8.3(8.1)
Mg[B(Sal) <sub>2</sub> ] <sub>2</sub> .10H <sub>2</sub> O	110	43.84(44.66)	3.99(4.52)	22.3(21.6)

<sup>a</sup> Calculated in parentheses (Sal=C<sub>7</sub>H<sub>4</sub>O<sub>3</sub>)

### FTIR Spectra of Boric Acid-Salicylic Acid Complexes

One of the most significant changes is the narrowing in the O-H stretching band on going from salicylic acid itself (a) to the complexes. The intermolecular hydrogen bonds formed by the carboxylic acid and OH groups of salicylic acid were cleaved in the complexes since these groups were involved in esterification reaction. The disruption of the hydrogen bonded network resulted in a narrowing in the O-H stretching band. Some important shifts and intensity changes, due to complexation with boron, in  $\nu(\text{CO})$ ,  $\nu(\text{CC})_{\text{arom}}$  vibrations of salicylic acid and  $\nu_a(\text{COO})$  and  $\nu_s(\text{COO})$  of sodium salicylate, are summarized in Table 4. There are also changes in the  $\delta_{\text{OH}}$  vibrations around  $1600 \text{ cm}^{-1}$  due to the participation of the phenol group in esterification with boron, however these changes are difficult to clarify due to the overlapping  $\nu(\text{CC})$  and  $\nu_a(\text{COO})$  vibrations in the same region. The characteristic vibrations of B-O bond in the tetra hedral boron complexes in the range  $900\text{-}1000 \text{ cm}^{-1}$  were also overlapped with the  $\nu(\text{C-O})$  band [20].

### Genomic DNA Isolation

Peripheral blood samples (9 ml) of healthy, male, Holstein calves at 6 months of age were collected from *vena jugularis* in EDTA containing blood tubes and CG-DNA were extracted using Wizard<sup>®</sup> Genomic DNA Purification kit (Promega, Medison WI, USA). The amounts and purity (260/280 nm ratio) of extracted DNA samples were detected on a microplate spectrophotometer (Epoch, BioTek, Vermont, USA) and  $250 \text{ ng}/\mu\text{l}$  concentration was used in DNA binding experiments. The concentration of DNA was determined by absorption spectroscopy using the molar absorptivity of  $6600 \text{ M cm}^{-1}$  at  $260 \text{ nm}$  [28].

**Table 4.** A summary of the FT-IR spectral data of salicylic acid-borate complexes

Compound	$\nu(\text{O-H})$	$\nu(\text{CO})$ & $\nu(\text{CC})$	$\nu_a(\text{COO})$ & $\nu_s(\text{COO})$	$\nu(\text{C-O})$ & $\nu_a(\text{B-O})/\text{BO}_4$	$\nu_s(\text{B-O})/\text{BO}_4$
Salicylic Acid	3350-2400	1685s, 1613		–	–
Na-salicylate		1597	1583, 1376	1250w	–
Borax	~3300	–	–	1220s	834+815 doublet
$\text{Na}[\text{B}(\text{Sal})(\text{OH})_2] \cdot \text{H}_2\text{O}$	3700-3000 (3436,3068)	1687s	1613s, 1351s	260-900 sharp (max. at 1150)	753, 695
$\text{Mg}[\text{B}(\text{Sal})_2]_2 \cdot 10\text{H}_2\text{O}$	3700-2800 (3424,3070)	1662vs	1611s, 1362m	1200-900,b (max. at 1144)	753, 698

### **DNA Binding Experiment**

In DNA binding experiments, in order to adjust the desired concentrations, the complexes were dissolved in sterile deionized ultrapure water. The extracted CG-DNA (11.25 and 22.50  $\mu\text{g}$ ) was mixed with a solution of the complex (100  $\mu\text{M}$ ) at a fixed concentration and UV-Vis spectra were obtained using the microplate spectrophotometer in 96-well UV microtiter plates (Thermo Scientific) [21, 29, 30].

### **DNA Cleavage Experiments**

The level of DNA cleavage was observed by agarose gel electrophoresis. A solution containing 25  $\mu\text{l}$  of CG-DNA (1.67  $\text{ng}/\mu\text{l}$ ), the complexes (5, 0.5 and 0.05  $\text{mM}$ ), and  $\text{H}_2\text{O}_2$  (60  $\text{mM}$ ) was incubated at 37  $^\circ\text{C}$  for 3 h. The gel electrophoresis experiment was conducted at 75 V for 3 h in 0.7% (w/v) agarose gel containing 0.5 $\times$  TBE buffer. After electrophoresis, the gel was stained with 3 $\times$  GelRed (Biotium) fluorescent nucleic acid dye in 0.5 $\times$  TBE buffer for 30 min by shaking and visualized using Doc EZ gel imaging system (Bio-Rad) [31].

### **Viscosity measurements**

Viscosity measurements were carried out using an Ubbelodhe viscometer, which was immersed in a thermostatic water-bath that kept at a constant temperature at 25  $^\circ\text{C}$ . The compounds were added into CG-DNA solution presented in the viscometer. The flow time of each compound was measured by a digital stopwatch. Data were shown as  $(\eta/\eta_0)^{1/3}$  vs. binding ratio [32], where  $\eta$  and  $\eta_0$  were the viscosity of DNA in the presence and absence of the complexes. Viscosity values were calculated from the observed flow time of CG-DNA containing solutions corrected from the flow time ( $t_0$ ),  $\eta = t - t_0$  [32–34].

### **ACKNOWLEDGMENTS**

The authors thank Dr. Nermin Sarigül and Dr. Gülden Başıyigit Kılıç (Mehmet Akif Ersoy University) for technical support in the experiments.

### **REFERENCES**

- [1]. G. Ciciani, M. Coronello, G. Guerrini, *Bioorg. Med. Chem.*, **2008**, *16*, 9409.
- [2]. C.P. Tan, J. Liu, L.M. Chen, *J. Inorg. Biochem.*, **2008**, *102*, 1644.
- [3]. J. Liu, W.J. Mei, A.W. Xu, *Antiviral. Res.*, **2004**, *62*, 65.
- [4]. B.N. Trawick, A.T. Daniher, J.K. Bashkin, *Chem. Rev.*, **1998**, *98*, 939.

- [5]. S.C. Zhang, Y. Shao, *Chinese J. Inorg. Chem.*, **2006**, 22, 1733.
- [6]. V.S. Li, D. Choi, Z. Wang, *J. Am. Chem. Soc.*, **1996**, 118, 2326.
- [7]. G. Zuber, J.C. Quada Jr., S.M. Hecht, *J. Am. Chem. Soc.*, **1998**, 120, 9368.
- [8]. S.M. Hecht, *J. Nat. Prod.*, **2000**, 63, 158.
- [9]. J-G. Liu, B-H. Ye, H. Li, *J. Inorg. Biochem.*, **1999**, 76, 265.
- [10]. L.M. Chen, J. Liu, J.C. Chen, *J. Mol. Struct.*, **2008**, 881, 156.
- [11]. G.W. Kabalka, Current topics in the chemistry of boron, The Royal Society of Chemistry, Cambridge, **1994**, pp. 255, 265, 303, 323, 337.
- [12]. S. Díaz, A. González, S. González, A. Rodríguez, *J. Organometallic Chem.*, **2000**, 610, 25.
- [13]. F.H. Nielsen, S.L. Meacham, *J. Evid. Based Complementary Altern. Med.*, **2011**, 16, 169.
- [14]. N. Raman, K. Pothiraj, T. Baskaran, *J. Mol. Struct.*, **2011**, 1000, 135.
- [15]. S.E. Livingstone, *Coord. Chem.*, **1980**, 20, 141.
- [16]. A.K. Mesmaeker, J.P. Lecomte, J.M. Kelly, *Top. Curr. Chem.*, **1996**, 177, 25.
- [17]. L-N. Ji, X-H. Zou, J-G. Liu, *Coord. Chem. Rev.*, **2001**, 216-217, 513.
- [18]. N.A.P. Kane-Maguire, J.F. Wheeler, *Coord. Chem. Rev.*, **2001**, 211, 145.
- [19]. Y. Xiong, L-N. Ji, *Coord. Chem. Rev.*, **1999**, 185-186, 711.
- [20]. D.A. Köse, Ph.D. Thesis, Ankara-Turkey, **2008**, 56-84.
- [21]. P. Krishnamoorthy, P. Sathyadevi, A. H. Cowley, *Eur. J. Med. Chem.*, **2011**, 46, 3376.
- [22]. J. Marmur, *J. Mol. Biol.*, **1961**, 3, 208.
- [23]. J. Jiang, X. Tang, W. Dou, *J. Inorg. Biochem.*, **2010**, 104, 583.
- [24]. A. Wolfe, G.H. Shimer, T. Meehan, *Biochemistry*, **1987**, 26, 6392.
- [25]. J. Bernadou, G. Pratviel, F. Bennis, *Biochemistry*, **1989**, 28, 7268.
- [26]. M.T. Carter, M. Rodriguez, A.J. Bard, *J. Am. Chem. Soc.*, **1989**, 111, 890.
- [27]. M. Eriksson, M. Leijon, C. Hiort, *Biochemistry*, **1994**, 33, 503.
- [28]. Y. Xiong, X-F. He, X-H. Zou, *J. Chem. Soc., Dalton Trans.*, **1999**, 19.
- [29]. J.K. Barton, A. Danishefsky, J. Goldberg, *J. Am. Chem. Soc.*, **1984**, 106, 2172.
- [30]. F. Arjmand, M. Aziz, *Eur. J. Med. Chem.*, **2009**, 44, 834.
- [31]. A.Y. Louie, T.J. Meade, *Chem. Rev.*, **1999**, 99, 271.
- [32]. B.V. Kumar, H.S. Bhojya Naik, D. Girija, *Spectrochim. Acta A*, **2012**, 94, 192.
- [33]. I. Haq, P. Lincoln, D. Suh, *J. Am. Chem. Soc.*, **1995**, 117, 4788.
- [34]. J. Kang, S. Dong, X. Lu, *J. Macromol. Sci. A: Pure Appl. Chem.*, **2006**, 43, 279.
- [35.] A. Arslantas, A.K. Devrim, M. Sudagidan, D.A. Köse, *Journal of Chemistry*, **2013**, 2013, 1.

## C REACTIVE PROTEIN LEVEL AS A DIAGNOSE TEST FOR SLEEP APNEA-HYPOPNEA SYNDROME

MIHAELA ALEXANDRA POP<sup>a</sup>, TUDOR CATALIN DRUGAN<sup>b\*</sup>,  
ADRIANA GROZAV<sup>c\*</sup>, BIANCA DOMOKOS<sup>a</sup>,  
ANDRADA URDA<sup>a</sup>, CARMEN MONICA POP<sup>a</sup>

**ABSTRACT.** Sleep apnea-hypopnea syndrome is a disease characterized by repetitive episodes of partial or total collapse of the upper airways during sleep. The collapse of the upper airways and the repeated nocturnal desaturations of arterial blood in this disease lead to the development of chronic low-grade systemic inflammation, contributing to the pathogenesis of cardiovascular diseases. C-reactive protein is an inflammatory marker with pentameric structure that migrates electrophoretically in the gamma vicinity. The present study has aimed to determine the diagnostic ability of CRP levels for SAHS in order to facilitate exploratory tests in sleep medicine. In order to obtain a proper diagnostic test a compromise was made between sensitivity and specificity using Receiving Operating Characteristic curve. "Area under curve" was 0,7742 for a 95% confidence interval,  $p = < 0,0001$ . CRP values  $< 10$  mg/ l showed a less sensitive test, but very specific. CRP values  $> 12$  mg/ l showed a very sensitive test, but the specificity decreased dramatically. We have demonstrated that CRP levels cannot be used for positive diagnosis of SAHS, because, despite high values are associated with a positive diagnosis, the specificity of the test decreases dramatically when the CRP values are higher than 13 mg/ l.

**Keywords:** *apnea, hypopnea, polysomnography, C- reactive protein, the ROC curve*

### INTRODUCTION

Sleep apnea-hypopnea syndrome (SAHS) is a disease that affects 4% of middle-aged men and 2% of middle-aged women [1]. This disease is

---

<sup>a</sup> "Iuliu Hațieganu" University of Medicine and Pharmacy, Cluj – Napoca. Department of Pneumology, B. P. Hașdeu no. 6, 400609, Cluj – Napoca, Romania

<sup>b</sup> "Iuliu Hațieganu" University of Medicine and Pharmacy, Cluj – Napoca. Department of Medical Informatics and Biostatistics, Pasteur no. 6, 400012, Cluj – Napoca, Romania

<sup>c</sup> "Iuliu Hațieganu" University of Medicine and Pharmacy, Cluj – Napoca. Department of Organic Chemistry, Victor Babeș no. 41, Cluj – Napoca, Romania.

\* Corresponding authors: [tdrugan@umfcluj.ro](mailto:tdrugan@umfcluj.ro), [adriana.ignat@umfcluj.ro](mailto:adriana.ignat@umfcluj.ro)

characterized by repetitive episodes of partial (hypopnea) or total (apnea) collapse of upper airways during sleep which arise from the pharyngeal muscle relaxation [2, 3, 4]. Along with sleep initiation, in these patients, a vicious cycle is repeated: upper airways obstruction, reopening them, a time for arousals and subsequent asphyxia [5]. All these events occurred every night, are associated with intermittent hypoxemia and hypocapnia, hyperventilation, and thus sleep fragmentation and excessive daytime sleepiness [2, 4]. The collapse of the upper airways, repeated nocturnal desaturations of arterial blood, result in a chronic low-grade systemic inflammation, thereby contributing to the pathogenesis of atherosclerosis and the process of atheromatosis [6, 7]. The C-reactive protein (CRP), interleukin 6, tumor necrosis factor alpha and pentraxin 3 are part of the inflammatory markers and cardiovascular pathologies encountered in respiratory disorders during sleep [1, 8]. Interleukin 6 is a pro-inflammatory cytokine and an inducer of the hepatic acute phase response which stimulates the production of CRP [1]. CRP is a non-glycosylated protein with pentameric structure that migrates electrophoretically in the gamma vicinity. This is an acute phase reactant that increases rapidly in response to tissue damage, viral/ bacterial and neoplastic pathologies. During tissue necrosis and inflammation resulting from microbial infection, the concentration of this protein may increase to 300 mg/ l in 12/ 24 h. At the same person, CRP concentration/ 24 h is almost stable, thus easy to detect a possible inflammatory response in patients with SAHS [9]. Fragmentation and sleep deprivation are pro-inflammatory by themselves. Meier- Ewert et al. demonstrated that 88 hours/ 12 days of sleep deprivation, or 10 days of sleep restriction for 4 hours/ night were associated with increased levels of CRP [10].

Validity of diagnostic procedures means its ability to identify subjects touched by the disease and healthy subjects. Establishing a diagnosis is an imperfect process, which can be expressed rather in terms of probability than in terms of certainty. A diagnostic test will not be effective unless the result is able to alter the probability of disease, or to reduce the likelihood of it to such a level, that treatment should not be done, or to rise to the level at which treatment is legitimate.

The probability of being touched by a disease is not fixed, but related to the diagnostic test: before the test, it is likely "a priori" (pre-test probability) - that is, simply, the prevalence; after the test, it is likely "a posteriori" (post-test probability) - is what is called the predictive value of the test.

The sensitivity of a test (or the likelihood of a positive real) is the probability of a positive test when there is disease. A sensitive test rarely misses the diagnosis in patients touched by the disease. False negative results are rare. Such a test should be chosen when a disease is serious and cannot be ignored, when there is a cure for the disease or when a possible false positive has harmful consequences for the patient. False negative results are rare, a sensitive test is useful for the doctor, especially when the result is negative; it can be pretty sure that eliminates the disease.

The specificity of a test (or negative real probability) is the probability of a negative test, when there is disease. A specific test rarely says that a subject is sick, when in reality it is not. False positive results are rare. A specific test should be chosen when a false positive can be harmful to the patient, in physical, psychological or economic terms. Since false positives are rare, a specific test is especially useful when the result is positive; the doctor can be pretty sure that the disease is present.

The compromise between sensitivity and specificity is achieved using a curve that characterizes the performance of the test (ROC Curve: Receiving Operating Characteristic). It is obvious that the doctor wants to order a diagnostic test at the same time, sensitive and specific. This is not possible in practice. You always have to make a compromise between sensitivity and specificity. ROC curve represents a way of expressing the relationship between sensitivity and specificity of a diagnostic test. This allows the description of test accuracy and can be used practically to compare two different tests to diagnose the same disease: accepted standard test (golden standard) and a new diagnostic test.

In these circumstances, the present study aims to determine the ability of CRP levels to diagnose SAHS in order to facilitate exploratory tests in sleep medicine.

## RESULTS AND DISCUSSION

Of 100 patients entered into the study, 60 were diagnosed with SAHS. 55 patients had obstructive apnea- hypopnea. Forms of mild, moderate and severe disease were found in 2%, 21% and 37%. Like other studies in the medical literature, males predominated in 57% [11, 12]. 26 patients had values of CRP in the range of  $\leq 1,4$  to 9,52 mg/ l and 74 patients CRP values above 9,52 mg / l (Figure 1).

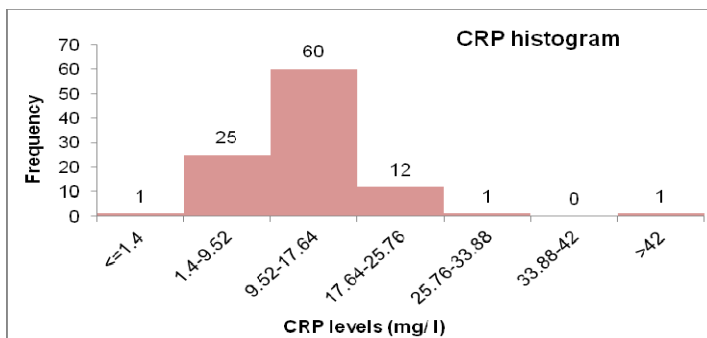
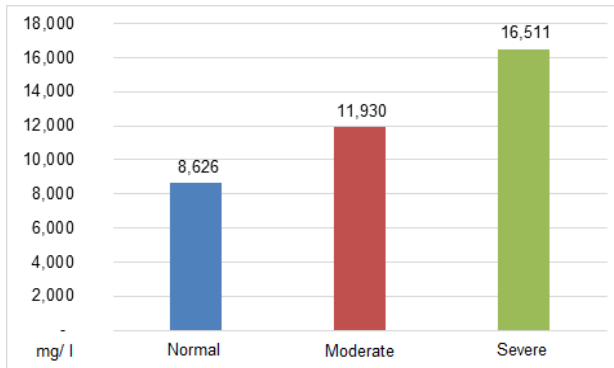


Figure 1. Distribution of patients after CRP levels

CRP Average in patients with SAHS was 14,54 and in those without apnea- hypopnea was 8, 62.

In this study, the moderate and severe forms of SAHS predominated, as the CRP levels presented in Figure 2. SAHS is a prevalent sleep disease and an independent risk factor in the development of cardiovascular diseases and in worsening of their morbidity and mortality. This was associated with risen levels of different circular and inflammatory markers [13]. There are studies that have demonstrated important and independent associations between the CRP levels and the severity of sleep apnea- hypopnea [2, 14, 15, 16]. Only a few studies showed an association between the moderate SAHS and high CRP level [17]. In our study the intermediary values of CRP were associated to the moderate forms of SAHS, as they were shown in figure 3. Nocturnal hypoxemia and sleep deprivation are often present in patients with SAHS and could be a way to mediate the association between SAHS and increased levels of inflammatory markers. [18, 19] Oxygen desaturation index could explain some of the apnea- hypopnea index (AHI) associations with the CRP level. [19]



**Figure 2.** Distribution of CRP levels according to the severity of SAHS

The ability of CRP to diagnose SAHS was performed using ROC analysis and showed an "area under curve" of 0,7742 for a confidence interval of 95% ( $p < 0,0001$ ); table 1. In figure 3 we showed the ROC curve of CRP.

**Table 1.** ROC curve for CRP vs SAHS

Area under the ROC curve	
Area	0,7742
Std. Error	0,04696
95% confidence interval	0.6821 to 0.8662
P value	< 0.0001
Data	
Control	40
Patient	60

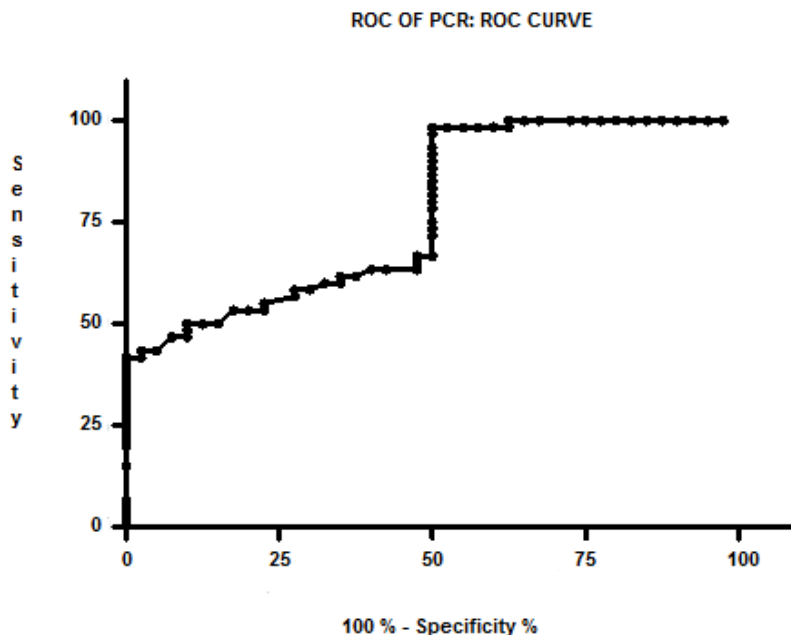


**Figure 3.** Graphical representation of the ROC curve

CRP values <10 mg/ l showed that the test was less sensible, there are many false- negative patients, but was very specific, so that all patients with CRP levels below 10 mg/ l were correctly diagnosed as not having SAHS.

CRP values > 12 mg/ l have shown that the test was very sensitive, being detected all patients with SAHS, but specificity decreased dramatically, leading to errors in the classification of subjects in false positive patients.

## CONCLUSIONS

We have demonstrated that CRP levels can be used as a negative diagnostic test for SAHS, this eliminating the suspicions of sleep apnea-hypopnea because it is a quick exploration, cheap, easy and practiced in routine.

CRP levels cannot be used for positive diagnosis because despite increased values are associated with a positive diagnosis, the specificity of the test decreases dramatically to more than 13 mg/ l of the CRP.

## **EXPERIMENTAL SECTION**

### **Patients and study design**

This study was conducted for 6 months in Sleep Laboratory Alpes-Leman in Contamine- sur Arve, France. We included patients aged between 18 and 80 years, 60 subjects with a positive diagnosis of SAHS (if after performing the polysomnography (PSG) the AHI  $\geq 5$ / hour of sleep) and 40 subjects as control group with negative diagnosis of SAHS (AHI  $< 5$ / h). For each patient we included demographic data, levels of CRP and polysomnographic data. CRP values  $\geq 10$  mg/ l were considered pathological. Patients with various bacterial or viral infections, inflammatory disease/ different systemic or malignant neoplasia were excluded. The study was approved by the chief of Pneumology, being consistent with the principles of the Declaration of Helsinki. Each patient gave his verbal consent to participate in research. There weren't used experimental methods on subjects and the tests applied were the ones current of the hospital, the purpose of the paper was to emphasize the standard methods of diagnosis.

### **Polysomnographic monitoring**

The polysomnography was performed with "Morpheus hand held", recorded by Micromed s.p.A connected to System Plus Evolution 1061. This unit has recorded various nocturnal signals such as: electro-encephalogram, electro- oculogram, electro- cardiogram, nasal respiratory flow, pulse, oxygen saturation, snoring intensity, mentonier tone, thoracic and abdominal respiratory movements, leg movements, the position of the body and the time spent in bed. PSG recordings were performed manually using the program "Rembrandt Analysis Manager 7.5", by doctors attached to the service, in accordance with the recommendations of Rechtschaffen – Kales and the American Academy of Sleep Medicine.

An AHI  $\geq 5$ / h of sleep was needed to diagnose SAHS, an AHI  $\geq 5 < 15$  indicated mild SAHS and AHI  $\geq 15$ / h indicated a moderate to severe SAHS. PSG recordings were not taken into account if the total sleep time was  $< 180$  minutes or quality of the main signals (electro- encephalogram, oxygen saturation, nasal flow, toraco- abdominal movements) was lower than 20% of the total registration.

### **Measurement of C- reactive protein**

The amount of CRP in the serum was dispensed obtained after centrifugation (3000 revolutions/ minute, during 10 minutes) of the patient's peripheral venous blood. CRP concentration was measured by latex

turbidimetry. Latex- turbidimetry was based on antigen- antibody complex formation in solution. The solutions of antigen and antibody were mixed, being required small quantities of reactive; aggregate formation occurring rapidly. This method was based upon the reactions between C- reactive protein and latex covalently bound antibodies against human CRP. CRP values were determined photometrically.

### **Statistical Analysis**

It was performed a case- control study between CRP concentrations and the presence or absence of apnea- hypopnea. Qualitative variables were described using frequency tables, contingency and column graphs. To describe quantitative variables we used the average (mean), median, range interquartile Q25, Q75, frequency tables, histograms. Test "t" Student for independent samples or analysis of variance ANOVA were applied for comparison of means. Mann-Whitney/ Kruscal- Wallis tests were used for a confidence interval of 95%. We made the ROC curves and determined the "area under the curve" for a confidence interval of 95%. We calculated the sensitivity and specificity of CRP for the diagnosis of SAHS. In order to calculate the ROC curve and its parameters it was used specific software named GraphPad Prism.

### **ABREVIATIONS**

AHI, Apnea- Hypopnea Index; CRP, C- Reactive Protein; PSG, Polysomnography; ROC, Receiver Operating Characteristic; SAHS, Sleep Apnea-Hypopnea Syndrome.

### **ACKNOWLEDGMENTS**

The authors are sincerely grateful to the POSDRU 107/ 1.5/ S/ 78702 project of "Iuliu Hatieganu" University of Medicine and Pharmacy, Cluj – Napoca for financial support and research facilities.

### **REFERENCES**

- [1]. T. Young, M. Palta, J. Dempsey, J. Skatrud, S. Weber, S. Badr, S. *N. Engl. J. Med.*, **1993**, 328, 1230.
- [2]. R. Mehra, S. Redline, *J. Allergy Clin. Immunol.*, **2008**, 121(5), 1096.

- [3]. K. Murase, K. Mori, C. Yoshimura, K. Aihara, Y. Chihara, M. Azuma, et al., *Plos One*, **2013**, *8*(1), e54184.
- [4]. Q. Wang, Q. Wu, J. Feng, X. Sun, *Patient Preference and Adherence*, **2013**, *7*, 1077.
- [5]. N. M. Al Lawati, S.R. Patel, N.T. Ayas, *Prog. Cardiovasc. Dis.*, **2009**, *51*, 285.
- [6]. A. Baessler, R. Nadeem, M. Harvey, E. Madbouly, A. Younus, H. Sajid, et al., *Journal of Inflammation*, **2013**, *10* (13), 1.
- [7]. W. Sun, X. Yin, Y. Wang, Y. Tan, L. Cai, B. Wang, et al., *Dose-Response*, **2013**, *11*, 385.
- [8]. H.J. Yue, P.J. Mills, S. Ancoli- Israel, J.S. Lored, M.G. Ziegler, J.E. Dimsdale, *Sleep Breath*, **2009**, *13*, 263.
- [9]. O. Kokturk, T.U. Ciftci, E. Mollarecep, B. Ciftci, *Int. Heart J.*, **2005**, *46* (5), 801.
- [10]. H.K. Meier- Ewert, P.M. Ridker, N. Rifai, M.M. Regan, N.J. Price, D.F. Dinges, J.M. Mullington, *J. Am. Coll. Cardiol.*, **2004**, *43* (4): 678.
- [11]. I. Peregrim, S. Gresova, M. Pallayova, B.L. Fulton, J. Stimmelova, I. Bacova, et al., *Physiol. Res.*, **2013**, *62*, 569.
- [12]. J.P. Bounhoure, M. Galinier, A. Didier, P. Leophonte, *Bull. Acad. Natl. Med.*, **2005**, 189: 445.
- [13]. K.M. Edwards, L.M. Tomfohr, P.J. Mills, J.A. Bosch, S. Ancoli-Israel, J.S. Lored, J. Dimsdale, *Sleep*, **2011**, *34*(2), 161.
- [14]. U. Hatipoglu, I. Rubinstein, *Respiration*, **2003**, *70*, 665.
- [15]. A. Panoutsopoulos, A. Kallianos, K. Kostopoulos, C. Seretis, E. Koufogiorga, A. Protogerou, et al., *Med. Sci. Monit.*, **2012**, *18*(12), CR747- 751.
- [16]. M. Sevensson, P. Venge, C. Janson, E. Lindberg, *J. Sleep Res.*, **2012**, *21*, 147.
- [17]. J. Sahlman, K. Miettinen, K. Peuhkurinen, J. Seppa, M. Peltonen, C. Herder, et al., *J. Sleep Res.*, **2010**, *19*, 341.
- [18]. M. Planellas, R. Cuenca, M.D. Tabar, C. Bertolani, C. Poncet, J.M. Closa, et al., *BMC Veterinary Research*, **2012**, *8* (152), 1.
- [19]. E.K. Larkin, C.L. Rosen, H.L. Kirchner, A. Storfer-Isser, J.L. Emancipator, N.L. Johnson, et al., *Circulation*, **2005**, *111*, 1978.

## SOME NEW RESULTS ON THE NULLITY OF MOLECULAR GRAPHS

MODJTABA GHORBANI<sup>a</sup>

**ABSTRACT.** The nullity of a graph is defined as the multiplicity of eigenvalue zero of graph  $G$  is named the nullity of  $G$  denoted by  $\eta(G)$ . In this paper we investigate some properties of the nullity of some classes of graphs and then we compute the nullity of some infinite families of dendrimers.

**Key Words:** *characteristic polynomial, nullity, dendrimers.*

### INTRODUCTION

Let  $G = (V, E)$  be a graph and  $e$  be an arbitrary edge. Then  $G \setminus e$  means a subgraph of  $G$  obtained by removing the edge  $e$  from  $G$ . On the other hand, the subgraph  $G \setminus \{v_1, \dots, v_k\}$  is a graph obtained by removing the vertices  $v_1, \dots, v_k$  from  $G$  and all edges incident to any of them. The line graph of  $G$ , denoted by  $L(G)$ , is the graph whose vertex set is  $E(G)$  and two vertices of  $L(G)$  are adjacent if the corresponding edges in  $G$  are incident.

The adjacency matrix  $A(G)$  of graph  $G$  with vertex set  $V(G) = \{v_1, v_2, \dots, v_n\}$  is a square  $n \times n$  symmetric matrix  $[a_{ij}]$ , such that  $a_{ij} = 1$  if  $v_i$  and  $v_j$  are adjacent and 0, otherwise. The characteristic polynomial  $\Phi_G(\lambda)$  of  $G$  is defined as

$$\Phi_G(\lambda) = \det(A(G) - \lambda I).$$

Hence, the eigenvalues of graph  $G$  are the roots of  $\Phi_G(\lambda)$  and form the spectrum of  $G$ . The nullity of graph  $G$  is the number of zero eigenvalues in its spectrum denoted by  $\eta(G)$ . Suppose  $r(A(G))$  be the rank of  $A(G)$ ; it is well – known fact that  $\eta(G) = n - r(A(G))$ .

A null graph is a graph in which all the vertices are isolated. It is clear that  $\eta(G) = n$  if and only if  $G$  is a null graph, see [1].

---

<sup>a</sup> Department of Mathematics, Faculty of Science, Shahid Rajaee Teacher Training University, Tehran, 16785 – 136, I. R. Iran; E-mail: mghorbani@srttu.edu

The problem of characterizing all the graphs with zero nullity was first considered by Collatz and Sinogowitz [2]. This question is of great interest in chemistry because, if a conjugated hydrocarbon molecule is chemically stable, then its Hückel graph has zero nullity, see [3]. Computing the nullity of a graph is also an interesting problem in mathematics, since it is related to the rank of the adjacency matrix. There are many results on the nullity of trees, unicyclic graphs and bicyclic graphs, see [4-8]. Let  $G$  be a graph with edge set  $E(G)$ . For instance, Gutman and Sciriha [9] proved that for any tree  $T$ ,  $\eta(L(T)) = 0$  or  $1$ . Some results on the nullity of line graphs can be found in [10-16].

## PRELIMINARIES

We first introduce some concepts and notations of signed graphs. Recall that a set  $M$  of edges of  $G$  is a matching if every vertex of  $G$  is incident with at most one edge in  $M$ ; it is a perfect matching if every vertex of  $G$  is incident with exactly one edge in  $M$ . Maximum matching is a matching with the maximum possible number of edges. The size of a maximum matching of  $G$ , is the maximum number of independent edges of  $G$  denoted by  $\mu = \mu(G)$ .

**Proposition 1**[1]. Let  $G = G_1 \cup G_2 \cup \dots \cup G_t$  where  $G_1, G_2, \dots, G_t$  are connected components of  $G$ . Then

$$\eta(G) = \sum_{i=1}^t \eta(G_i).$$

**Proposition 2**[17]. Let  $G$  be a simple graph on  $n$  vertices and  $K_p$  be a subgraph of  $G$ , where  $2 \leq p \leq n$ . Then  $\eta(G) \leq n - p$ .

**Theorem 1**[18]. If a bipartite graph  $G$  with  $n \geq 1$  vertices does not contain any cycle of length  $4s$ , ( $s = 1, 2, \dots$ ), then  $\eta(G) = n - 2\mu(G)$ .

**Corollary 1** [19]. If the bipartite graph  $G$  contains a pendent vertex, and if the induced subgraph  $H$  of  $G$  is obtained by deleting this vertex together with the vertex adjacent to it, then  $\eta(G) = \eta(H)$ .

**Corollary 2.** Let  $G_1$  and  $G_2$  be bipartite graphs. If  $\eta(G_1) = 0$  and if the graph  $G$  is obtained by joining an arbitrary vertex of  $G_1$  by an edge to an arbitrary vertex of  $G_2$ , then  $\eta(G) = \eta(G_2)$ .

**Theorem 2**[20].

- (i) A path with four vertices of degree 2 in a bipartite graph  $G$  can be replaced by an edge without changing the value of  $\eta(G)$ .
- (ii) Two vertices and the four edges of a cycle of length 4, that lie in a bipartite graph  $G$ , can be removed without changing the value of  $\eta(G)$ .

**Example 1.** Consider graph  $G_r$ , with  $r$  hexagons depicted in Figure 1(a). By using Corollary 1, it is easy to see that  $\eta(G_r) = \eta(G_{r-1})$  ( $r = 1, 2, \dots$ ). By induction on  $r$  it is clear that  $\eta(G_r) = 0$ . Now consider graph  $H_r$  (Figure 1(b)). This graph has a pendent vertex, thus according to Corollary 2,  $\eta(H_r) = \eta(T_{r-1})$ . By using Corollary 2, one can see that  $\eta(T_{r-1}) = \eta(H_{r-1})$ . By continuing this method we see that  $\eta(H_r) = \eta(H_1)$ .  $H_1$ , has a pendent vertex joined to a hexagon. Corollary 2 implies that  $\eta(H_1) = \eta(P_5)$  and by using Lemma 2.1, we have  $\eta(H_r) = \eta(P_5) = 1$ .

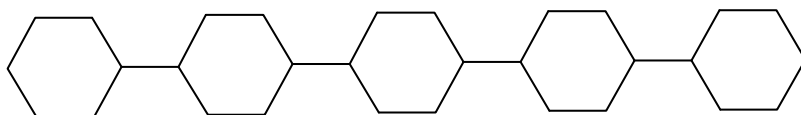


Figure 1 (a). Graph  $G_r$ .

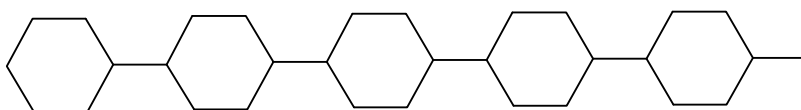


Figure 1(b). Graph  $H_r$ .

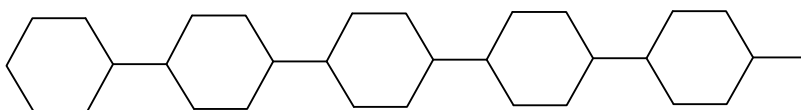
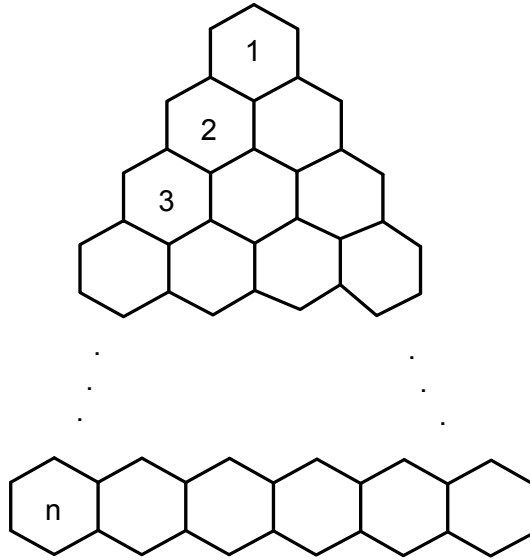


Figure 1(c). Graph  $T_{r-1}$ .

Here, by using Theorem 1, we compute the nullity of triangular benzenoid graph  $G[n]$ , depicted in Figure 2. By using Figure 3, one can deduce that the maximum matching can be computed as follows:

First we color the boundary edges, being exactly  $3 \times n$  edges. The number of colored vertical edges in the  $k$ -th row is  $k - 1$ . Hence, the number of colored vertical edges is  $1 + 2 + \dots + n - 2 = (n - 1)(n - 2)/2$ . By summation of these values one can see that the number of colored edges are  $3n + (n - 1)(n - 2)/2 = (n^2 + 3n + 2)/2$  which is equal to the size of maximum matching. This graph has  $n^2 + 4n + 1$  vertex,  $3(n^2 + 3n)/2$  edges and by using Theorem 1,  $\eta(G[n]) = n^2 + 4n + 1 - (n^2 + 3n + 2) = n - 1$ , thus we proved the following Theorem.

**Theorem 3.**  $\eta(G[n]) = n - 1$ .



**Figure 2.** Graph of triangular benzenoid  $G[n]$ .

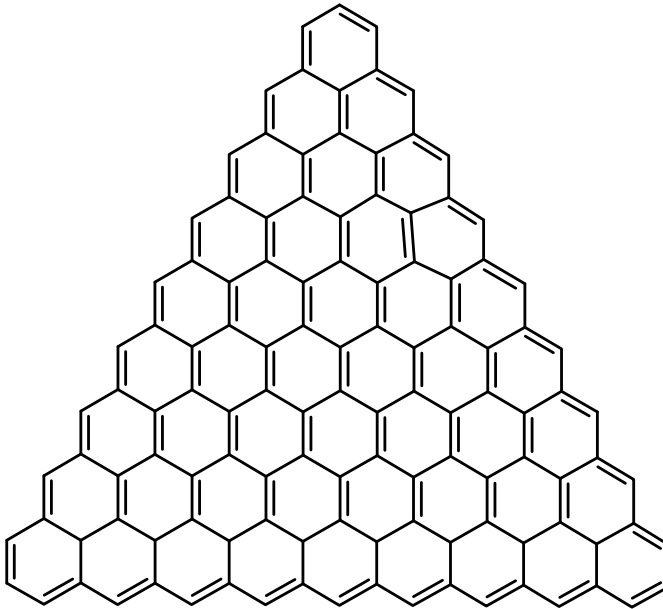


**Figure 3.** Graph of triangular benzenoid  $G[n]$ .

## MAIN RESULTS

In this section, we study some theoretical properties of nullity of graphs. We recall that a clique of a simple graph  $G$  is a subset  $S$  of  $V(G)$  such that  $G[S]$  is complete. A clique  $S$  is maximum if  $G$  has no clique  $S'$  with  $|S'| \geq |S|$ . The number of vertices in a maximum clique of  $G$  is called the clique number of  $G$  and is denoted by  $\omega(G)$ .

The  $k$ -coloring of a graph is an assignment of  $k$  colors to the vertices of the graph so that adjacent vertices have different colors. A chromatic number is the minimum required number of colors for the vertices of a given graph denoted by  $\chi(G)$ .

An independent vertex set of graph  $G$  is a set of vertices such that any two vertices are not adjacent. Thus, the independence number of  $G$  is the maximum of the cardinalities of all vertex independent sets denoted by  $\alpha(G)$ . Here, we compute some bounds for nullity with respect to the above definitions.

**Lemma 1** [21]. We have

$$\omega(G) \geq 2\chi(G) + \alpha(G) - n - 1.$$

**Theorem 3.** Let  $K_p$  be an induced subgraph of  $G$ , then

$$\eta(G) \leq 2n - 2\chi(G) - \alpha(G) + 1.$$

**Proof.** Since  $K_p$  is an induced subgraph of  $G$ ,  $\text{rank}(G) \geq p$  and thus  $\eta(G) \leq n - \omega(G)$ . By using Lemma 1, the proof is completed.

It is easy to see that the edge set  $E(G)$  of  $G$  can be partitioned into disjoint independent sets. Let  $E(G) = \bigcup_{i=1}^s E_i$  be a partition of disjoint elements of  $E(G)$ , where  $r_i$  is the number of parts of size  $e_i = |E_i|$ ,  $i = 1, 2, \dots, s$ . Then we have the following result.

**Lemma 2.** Let  $G$  be a bipartite graph with  $n \geq 1$  vertices and  $m$  edges without any cycle of length  $4s$  ( $s = 1, 2, \dots$ ), then

$$n - 2 \frac{m - (s-1)r_1 e_1}{r_s} \leq \eta(G) \leq n - 2 \frac{m + (s-1)r_1}{r_s + (s-1)r}.$$

**Proof.** Since  $e_s$  is the size of maximum matching of  $G$ ,  $e_s = \mu(G)$  and then

$$\begin{aligned} m &= |E(G)| = r_1 e_1 + r_2 e_2 + \dots + r_s \mu(G) \\ &\leq r_s \mu(G) + \sum_{i=1}^{s-1} r_i (\mu(G) - 1) \leq r_s \mu(G) + (\mu(G) - 1)(s-1)r_1. \end{aligned}$$

This implies that

$$\mu(G) \geq \frac{m + (s-1)r_1}{r_s + (s-1)r}.$$

For computing the lower bound it follows that:

$$m = \sum_{i=1}^s r_i e_i \geq (s-1)r_1 e_1 + r_s \mu(G)$$

Hence,

$$\mu(G) \leq \frac{m - (s-1)r_1 e_1}{r_s}$$

and the proof is completed.

Recall that a vertex in graph  $G$  is well-connected if it is adjacent with other vertices of  $G$ .

**Lemma 3.** Let  $v$  be a well – connected vertex so that  $G - \{v\}$  is a connected regular graph on  $n$  vertices. Then

$$\eta(G) = \eta(G - \{v\}).$$

**Proof.** It is easy to see that  $G = G - \{v\} + K_1$ . Since  $G - \{v\}$  is regular, by [22, Theorem 2.8],  $rank(G) = rank(G - \{v\}) + rank(K_1)$ .

This implies that

$$\eta(G) = n + 1 - rank(G) = n + 1 - [rank(G - \{v\}) + 1] = \eta(G - \{v\}).$$

**Corollary 3.** If  $G$  satisfies the conditions of Lemma 3, then

$$\eta(\bar{G}) = 1 + \eta(G - \{v\}).$$

**Theorem 4.** Let  $G$  be a connected graph and  $w$  be a vertex of  $G$  in which  $N(w) = N(u) \cup N(v)$  and  $N(u) \cap N(v) = \emptyset$  for some vertices  $u$  and  $v$ . Then

$$\eta(G) = \eta(G - \{w\}).$$

**Proof.** Let  $G$  satisfies the above conditions and  $A$  be adjacency matrix of  $G$ . Clearly, the sum of  $u$ -th and  $v$ -th rows equals the  $w$ -th row of  $A$  and this completes the proof.

**Corollary 4.** Let  $G$  be connected graph and  $w$  be a vertex of  $G$  in which  $N(w) = \bigcup_{j=1}^n N(u_j)$  so that  $N(u_i) \cap N(u_j) = \emptyset$  ( $1 \leq i, j \leq n$ ). Then

$$\eta(G) = \eta(G - \{w\}).$$

Let now  $G$  and  $H$  be two connected graphs,  $u \in V(G)$  and  $v \in V(H)$ , respectively. By connecting the vertices  $u$  and  $v$ , we obtain a bridge graph denoted by  $GuvH$ .

**Theorem 5.** We have

$$\eta(GuvH) = \min\{\eta(G), \eta(G - u)\} + \min\{\eta(H), \eta(H - v)\}.$$

**Proof.** It is easy to see that the characteristic polynomial of  $G$  can be written as follows:

$$\phi_G(x) = x^{\eta(G)} f(x),$$

where  $f(x)$  is a polynomial of  $rank(G)$ . It follows that

$$\phi(H, x) = x^{\eta(H)} g(x), \quad \phi(G - u, x) = x^{\eta(G-u)} h(x) \quad \text{and} \quad \phi(H - v, x) = x^{\eta(H-v)} k(x)$$

for some polynomials  $g(x)$ ,  $h(x)$  and  $k(x)$ , respectively. On the other hand, by [23] we have

$$\phi_{GuvH}(x) = \phi_G(x)\phi_H(x) - \phi_{G-u}(x)\phi_{H-v}(x).$$

This leads us to conclude that

$$\phi_{GuvH}(x) = x^{\eta(G)+\eta(H)}f_1(x) + x^{\eta(G-u)+\eta(H-v)}f_2(x)$$

for some polynomials  $f_1(x)$  and  $f_2(x)$  and this completes the proof.

**Corollary 5.** In Theorem 5, suppose  $u$  and  $v$  be cut vertices,  $G_1, G_2, \dots, G_k$  and  $H_1, H_2, \dots, H_k$  be respectively the components of  $G-u$  and  $H-v$  in which

$$\eta(G_1) = \eta(G_1 + u) + 1 \text{ and } \eta(H_2) = \eta(H_2 + v) + 1.$$

Then

$$\eta(GuvH) = \eta(G) + \eta(H).$$

Let  $G \square H$  be a graph obtained by coinciding vertex  $u$  of  $G$  by vertex  $v$  of  $H$ . Then we have:

**Corollary 6.** We have

$$\eta(G \square H) = \eta(G) + \eta(H) + 1.$$

**Proof.** By [22, Theorem 2.2.4], it is easy to see that:

$$\begin{aligned} \phi(G \square H, x) &= \phi(G, x)\phi(H - v, x) + \phi(G - u, x)\phi(H, x) - x\phi(G - u, x)\phi(H - v, x) \\ &= x^{\eta(G)+\eta(H-v)}p_1(x) + x^{\eta(G-u)+\eta(H)}p_2(x) \\ &\quad - x^{\eta(G-u)+\eta(H-v)+1}p_3(x) \end{aligned}$$

where,  $p_1(x)$ ,  $p_2(x)$  and  $p_3(x)$  are some polynomials. Clearly we have

$$\begin{aligned} \eta(G \square H) &= \min\{\eta(G) + \eta(H - v), \eta(G - u) + \eta(H), \eta(G - u) + \eta(H - v) + 1\} \\ &= \min\{\eta(G) + \eta(H) + 1, \eta(G) + \eta(H) + 3\} \\ &= \eta(G) + \eta(H) + 1. \end{aligned}$$

## NULITY OF DENDRIMERS

Consider the graph  $C$  depicted in Figure 4. By using Corollary 1,  $\eta(C) = \eta(C_1)$  and by Corollary 2,  $\eta(C_1) = \eta(C_2)$ . By continuing this method one can see that  $\eta(C) = \eta(C_5) = 1$  and we can deduce the following theorem.

**Theorem 6** [24]. Consider dendrimer graph  $S[n]$  depicted in Figure 5. Then,

$$\eta(S[n]) = 1.$$

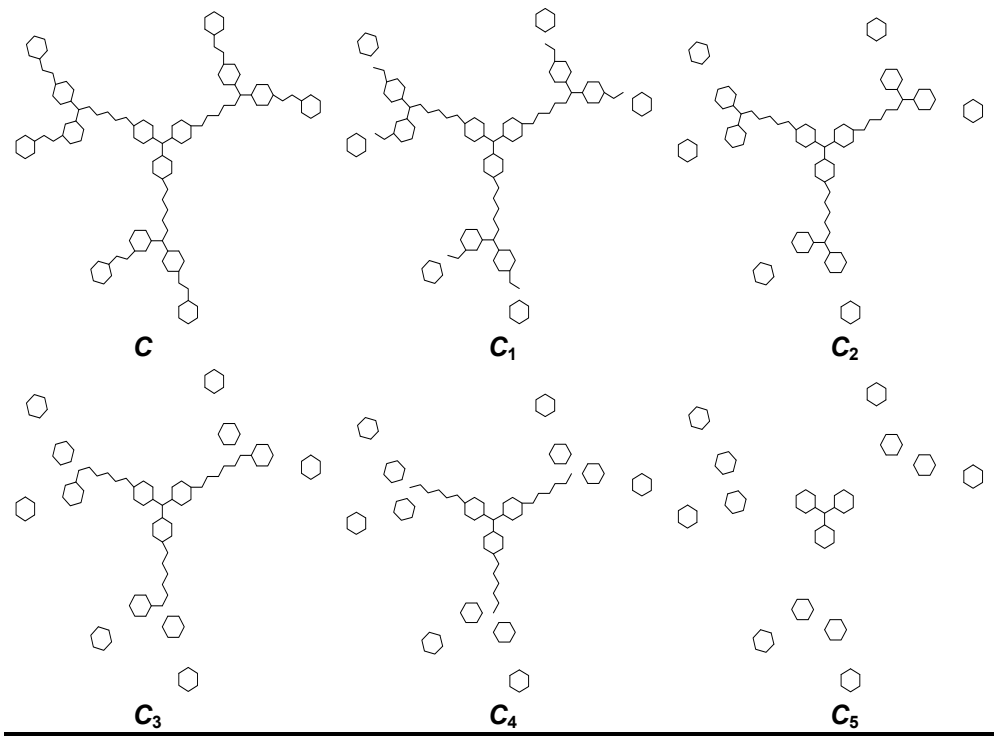


Figure 4. Computing the nullity of dendrimer  $C$  for  $n = 3$ .

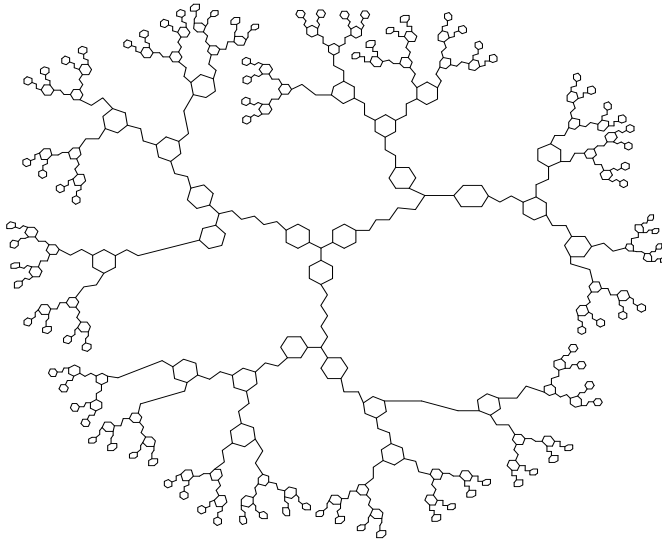
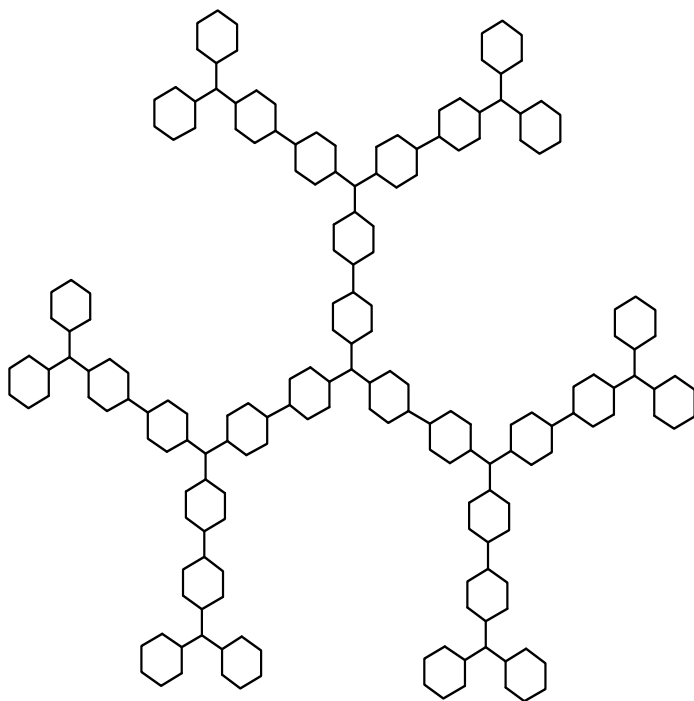


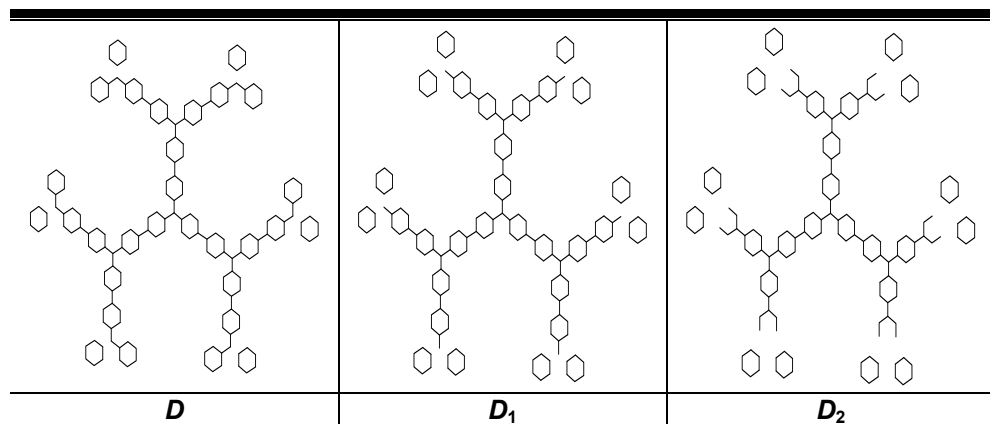
Figure 5. 2-D graph of dendrimer  $S[n]$ .

**Theorem 7** [24]. Consider the nanostar dendrimer  $D[n]$  in Figure 6, where  $n = 1, 2, \dots$ . Then

$$\eta(D[n]) = 2^{n-1}.$$



**Figure 6.** D graph of  $D[n]$ , for  $n = 3$ .



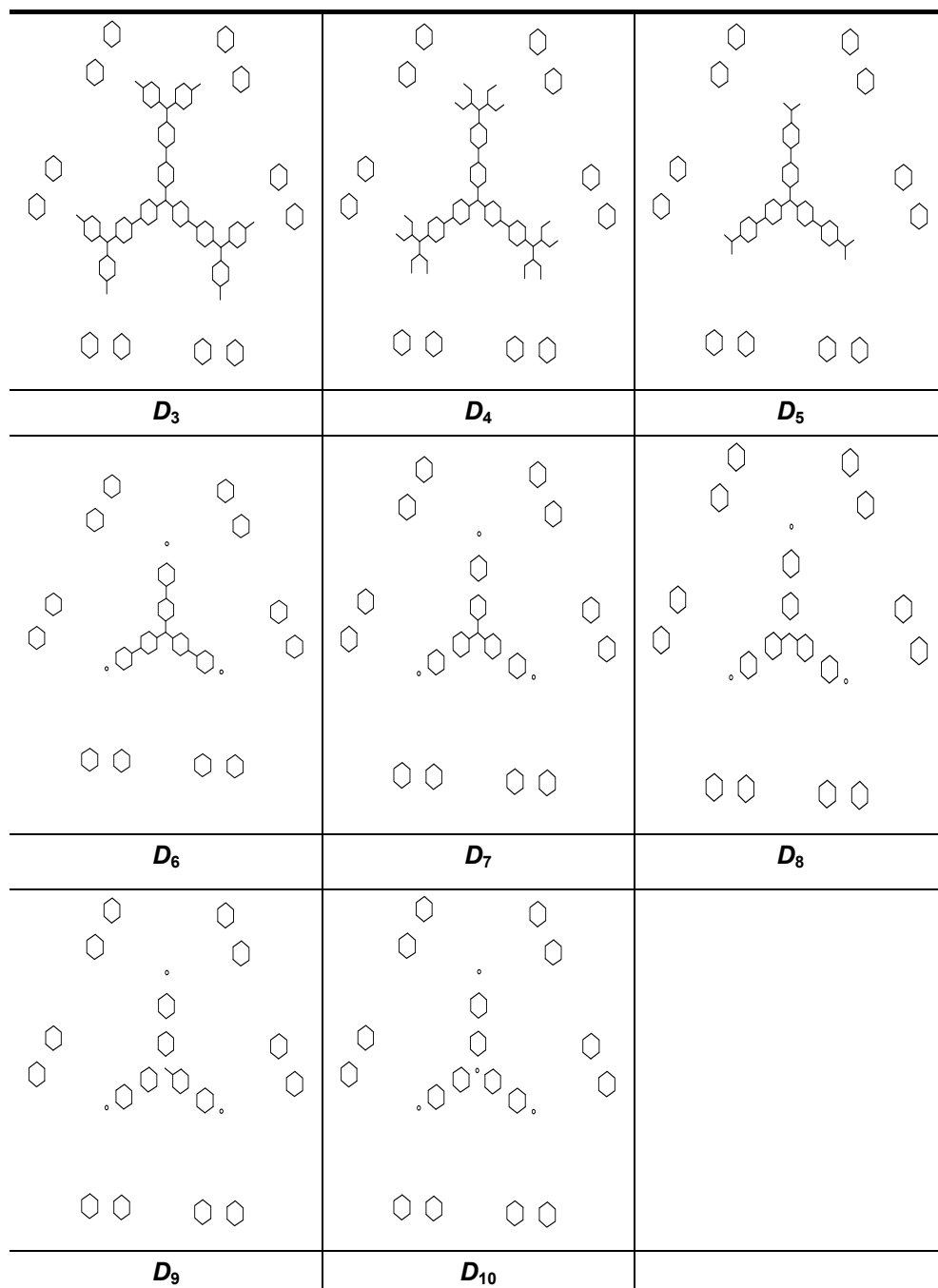


Figure 7. Computing the nullity of  $D[n]$ , for  $n = 3$ .

Here, we determine the nullity of dendrimer  $T[n]$ , depicted in Figure 8. First, suppose that  $n$  is even. It should be noted that the number of vertices of  $T[n]$  is  $2^{n+1}-1$ . The number of edges of a maximum matching is

$$\mu(T[n])=2+2^3+\dots+2^{n-1}=(2^{n+1}-2)/3.$$

Hence, according to Theorem 1, we have

$$\eta(T[n])=|V(T[n])|-2\mu(T[n])=2^{n+1}-1-2\cdot\frac{2^{n+1}-2}{3}=\frac{2^{n+1}+1}{3}.$$

Now suppose  $n$  is odd. Similar to the last discussion the matching number is  $\mu(T[n])=(2^{n+1}-1)/3$  and hence

$$\eta(T[n])=2^{n+1}-1-2\cdot\frac{2^{n+1}-1}{3}=\frac{2^{n+1}-4}{3}.$$

Thus, we proved the following theorem.

**Theorem 8.** Consider the dendrimer  $T[n]$ , depicted in Figure 8. Then

$$\eta(T[n])=\begin{cases} \frac{2^{n+1}+1}{3} & 2 \nmid n \\ \frac{2^{n+1}-4}{3} & 2 \mid n \end{cases}.$$

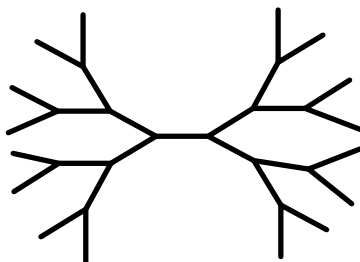


Figure8. 2-D graph of dendrimer  $T[n]$  for  $n = 3$ .

## REFERENCES

- [1] M. Watanabe, A.J. Schwenk, *J. Austral. Math. Soc. Ser. A*, **1979**, 28, 120.
- [2] L. Collatz, U. Sinogowitz, *Abh. Math. Sem. Univ. Hamburg*, **1957**, 21, 63.
- [3] H.C. Longuet-Higgins, *J. Chem. Phys.*, **1950**, 18, 265.

- [4] F. Ashraf, H. Bamdad, *MATCH Commun. Math. Comput. Chem.*, **2008**, 60, 15.
- [5] J.M. Guo, W.G. Yan, Y.N. Yeh, *Linear Algebra Appl.*, **2009**, 431, 1293.
- [6] J.X. Li, A. Chang, W.C. Shiu, *MATCH Commun. Math. Comput. Chem.*, **2008**, 60, 21.
- [7] W. Li, A. Chang, *MATCH Commun. Math. Comput. Chem.*, **2006**, 56, 501.
- [8] X.Z. Tan, B.L. Liu, *Linear Algebra Appl.*, **2005**, 408, 212.
- [9] I. Gutman, I. Sciriha, *Discrete Math.*, **2001**, 232, 35.
- [10] R.B. Bapat, *Bull. Kerala Math. Assoc.*, **2011**, 8, 207.
- [11] E. Ghorbani, *Disc. Math.*, **2014**, 324, 62.
- [12] S.C. Gong, G.H. Xu, *Linear Algebra Appl.*, **2012**, 436, 135.
- [13] H.H. Li, Y.Z. Fan, L. Su, *Linear Algebra Appl.*, **2012**, 437, 2038.
- [14] M.C. Marino, I. Sciriha, S. Simić, D.V. Tošić, *Publ. Inst. Math. (Beograd)*, **2006**, 79, 1.
- [15] I. Sciriha, *Congr. Numer.*, **1998**, 135, 73.
- [16] I. Sciriha, *Rend. Sem. Mat. Messina, Ser II*, **1999**, 5, 167.
- [17] B. Cheng, B. Liu, *El. J. Lin. Algebra*, **2007**, 16, 60.
- [18] A.J. Schwenk, R.J. Wilson, *On the eigenvalues of a graph*, in: L.W. Beineke, R.J. Wilson, Eds. *Selected Topics in Graph Theory*, Academic Press, London, **1978**.
- [19] D. Cvetković, I. Gutman, N. Trinajstić, *Croat. Chem. Acta*, **1972**, 44, 365.
- [20] S.C. Gong, G.H. Xu, *Linear Alg. Appl.*, **2012**, 436, 135.
- [21] G. Chartrand, P. Zhang, *Chromatic Graph Theory*, Chapman and Hall/CRC, **2008**.
- [22] D. Cvetković, P. Rowlinson, S. Simić, *An Introduction to the Theory of Graph Spectra*, Cambridge University Press, **2009**.
- [23] M. Ghorbani, M. Songhori, *Utilitas Mathematica*, in press.
- [24] M. Ghorbani, M. Songhori, *Studia UBB Chemia*, **2011**, 56 (2), 75.

## AN INTERPRETATION OF SOLID-LIQUID EXTRACTION USING THE GENERAL DIMENSIONAL METHOD

BARBU-RADU-HORATIU MISCA<sup>a,\*</sup>, DORIN-IOSIF MANCIULA<sup>b</sup>

**ABSTRACT.** The solid-liquid extraction is a very common method for recovery of bioactive compounds in both laboratory and large scale. Determining the conditions of operation is based for the most part on a researcher's practical experience. For scaling up to industrial conditions mathematical models or criteria equations are necessary. The paper presents the application of a general dimensional method to determine the parameters which influence the process and their respective degrees of impact. The parameters considered are: time, the equivalent diameter, the diffusion coefficient, density, dynamic viscosity, Earth's gravity, the interfacial force, the power dissipated into the process and linear velocity. The mathematical relation between the parameters in different conditions and the interpretation of this result is presented.

**Keywords:** *solid-liquid extraction, general dimensional method, mathematical model of solid-liquid extraction, criteria equation of solid-liquid extraction.*

### INTRODUCTION

The solid-liquid extraction is a very common method for recovery of bioactive compounds both in the laboratory and in large scale industrial processes. The determination of laboratory conditions of operation is work based in major part on a researcher's practical experience and on empirical study. For scaling up to industrial conditions, mathematical models obtained through theoretical calculus, criteria equations and experimental data are all necessary and must be compared and adjusted for specific conditions. In this work we propose a way to present the specific influence of any parameters which can determine solid-liquid extraction by means of the general dimensional analysis method.

---

<sup>a</sup> Babeş-Bolyai University, Faculty of Chemistry and Chemical Engineering, 11 Arany Janos Str., RO-400028, Cluj-Napoca, Romania

<sup>b</sup> Babeş-Bolyai University, Faculty of Environmental Science and Engineering, 30, Fantanele, Str., RO-400028, Cluj-Napoca, Romania

\* Corresponding author: [miscar@chem.ubbcluj.ro](mailto:miscar@chem.ubbcluj.ro)

For varied complex processes which offer complicate solutions, dimensional analysis is a most common way to initialise the research. In the study of a process, it can start from the differential equations which describe it, [1,2,3], or from the phenomenon theory, [4,5,6]. Knowledge of phenomenology may suggest the introduction of some variables in the list, size where is it not usually included in the differential equations. In this way, the number of variables included can increase so much that the determination of the groups of similitude and the numerical constants can be a laborious task from the experimental point of view, pursued at great expense of time, materials and human energy. The classical method of the determinant criterion and the incompatibility of the groups offer a global image over the fact that for every process variables exist which are sometimes important, but at other times become secondary. The relative importance of the variables can be evaluated after the identification of the numerical values of the exponents of the dimensionless groups from the  $\pi$  relation.

## RESULTS AND DISCUSSION

The general dimensional analysis method, (GDAM), [3], through the algorithm of development, allows the reduction of the number of numerical constants belonging to the criteria relation to one single value, giving thus an important advantage over the classical method. The mathematical base, regarding the reduction of the number of numerical constants, is represented by the possibility of writing the  $\pi$  equation which describes a physical phenomenon:

$$\pi_1 = C_1 \cdot \pi_2 \cdot \pi_3 \cdot \pi_4 \cdots, \text{ or: } (B \cdot J / E \cdot F) = C_1 \cdot (H \cdot I / N)^x \cdot (O \cdot P / R)^y \cdots \quad (1),$$

in the form of a relation of monomial type:

$$B = k \cdot (E \cdot F \cdot H^x \cdot I^x \cdot O^y \cdot P^y \cdots / J \cdot N^x \cdot R^y \cdots), \quad (2).$$

In order to treat a phenomenon using the general dimensional analysis, (GDA), this study contains three stages, [3]:

1. The first stage includes the presentation of the physical phenomenon, the assessment of the variables which interfere in its development and the separation of those which have a direct or reverse proportional action upon the variable which is considered to be most important (the independent variable). This stage can be performed by either studying the theory of the phenomenon, or can be done experimentally, and it leads to the elaboration of the matrix line of variables which describe the discussed process [1-5]. The separation of the variables is based on the mathematical evidence of the fact that a certain function, (1), or (2):

$$f_1 (B^{-1}, E, F, H^x, I^x, O^y, P^y, \dots, J^{-1}, N^{-x}, R^{-y}, \dots), \quad (3),$$

can be rewritten under the following form:

$$f_2 (E, F, H^x, I^x, O^y, P^y, \dots) = f_3 (B, J, N, R, \dots) \quad (4).$$

If the exponents of the dimensional equations  $f_2$  and  $f_3$  are only **positive** values, the solution of the non determined system of equations belonging to the exponential indexes will have only positive values.

The exponent index 0, (zero), **is not possible** because the mathematical evidence:

$$H^0 = 1 \quad (5),$$

leads to a numerical constant and the phenomenological analysis leads to a variable without importance to the process [1, 7].

2. The second phase refers to the assembly of the matrix of the dimensional variables, the allocation of an exponent index for each variable and the building of the undetermined system of dimensional equation through the method of the “progressive homogeneity” [1]. This is followed by the identification of the whole, positive, minimum and non-null solution and the formation of the dimensional relation of monomial type formed by the variables from the dimensional matrix having as the exponent the values from the solution of the system, [3]. The relation between variables which interfere during the development of a process or of a determined physical phenomenon is explained by taking into consideration the independent variable B. The expression of the relation is the simplest for the clear explicit dimension. The relation can be raised to a certain power index without losing the physical value, the new relation being different only in external form. Practically, these raises at a power are done in order to obtain complete, (whole), values of the exponents. To obtain such values, it is necessary that the relation be raised at a power of a common multiple of the denominators which belong to the rational exponents. In the case in which the adopted denominators have the lowest common multiple, the new values of the exponents will be the lowest, they will be at a minimum.

3. The third phase refers to determination of the numerical factor, (the numerical constant), of the monomial type relation. This operation is done considering experimental data and the constant value of the numerical factor is the theoretical and practical guarantee of the mathematical and phenomenological correctness of the monomial type relation which was obtained through GDAM, [1].

I propose to introduce another working stage in the methodology, [7]. This new stage should be placed between the two first stages and is expected to lead to the establishment of a certain importance hierarchy among the variables describing the process. Thus, a real mathematical basis may result in neglecting certain variables that are empirically considered to be less important,

a situation often encountered in during practical work and experimental studies. Moreover, after establishing the monomial type relation, one may operate mathematically upon it to obtain some criteria relations describing the process. Criteria expressions show the influence that different types of forces exert on the system, presenting details about this process phenomenology that would not be relevant otherwise, being dissimulated by other aspects.

The model bellow describes the dynamic solid-liquid extraction between the raw material and a solvent. During the contact of the raw material with the solvent, the dissolution of active component into solvent is initialised. This process is driven by the concentration difference of said active component between the solid and liquid phases and stops when the difference is zero. The duration of the process (process time) is a major parameter for solid-liquid extraction.

In the 1<sup>st</sup> stage, the matrix line of the variables describing the solid-liquid extraction and their influence, direct or reverse, is formed. The list of all the possible variables is presented bellow:

//  $\tau$ ;  $D_{1,2}$ ;  $d$ ;  $\rho$ ;  $\eta$ ;  $\sigma$ ;  $P$ ;  $g$ ;  $w$ ;  $c_{in}$ ;  $v$ ; //

where:

- $\tau$  - the time of process, [s];
- $D_{1,2}$  - the mass diffusion coefficient, [ $m^2/s$ ];
- $d$  - the equivalent diameter, [m];
- $\rho$  - the density, [ $kg/m^3$ ];
- $\eta$  - the dynamic viscosity, [Pa·s];
- $\sigma$  - the interfacial tension, [ $kg/s^2$ ];
- $P$  - the dissipate power, [ $kg \cdot m^2/s^3$ ];
- $g$  - the earth's gravitation, [ $m/s^2$ ];
- $c_{in}$  - the initial concentration of raw material, [ $kg/m^3$ ];
- $w$  - the velocity, [m/s];
- $v$  - the kinematical viscosity, [ $m^2/s$ ].

The 2<sup>nd</sup> stage. So that the additional proposed stage, the evaluation of the importance of functional parameters, can unfold, one starts by forming the minimum list of variables that are capable to describe the process. This can be measured from the solving condition of the system of undetermined diophantian equations imposed by GDAT: minimum, complete, positive and non-null solution.

- The combination of minimum variables, whit dimensional measure of each parameter, formed the dimensional matrix presented below:

$$\begin{array}{rcc}
 // & \tau^a, & D_{1,2}^b, & d^c // \\
 L & 0 & 2 & 1 \\
 M & 0 & 0 & 0 \\
 T & 1 & -1 & 0
 \end{array}$$

- L - the symbol of dimension "length";
- M - the symbol of dimension "mass";
- T - the symbol of dimension "time".

Its undetermined system of exponents is:

$$\begin{array}{l} L \quad 2b = c \\ M \quad 0 = 0 \\ T \quad a - b = 0, \end{array}$$

and has the minimum, entire, positive and not-null solution which is accepted by GDAM:

$$\begin{array}{l} L \quad c = 2, \\ M \quad 0 = 0, \\ T \quad a = 1; \quad b = 1. \end{array}$$

he monomial type relation generated by these results:

$$\tau = k_1 \cdot \frac{d^2}{D_{1,2}}, \quad (6),$$

is homogenous dimensionally, [s] = [s] and can form the Fourier criteria for diffusion,  $Fo_D$ ;

$$Fo_D = \frac{\tau \cdot D_{1,2}}{d^2} = k_1. \quad (7),$$

The expression indicated very clear and rigorously the mass transport mechanism for solid-liquid extraction, mass diffusivity.

For verification and for finding the relative importance of all parameters, the procedure is repeated, trough the introduction into the matrix line, step by step, of the desired parameter:

Through the introduction of **the initial concentration of raw material**,  $c_{in}$ :

//	$\tau^a$ ,	$D_{1,2}^b$ ,	$d^c$ ,	$c_{in}^q$ //
L	0	2	1	-3
M	0	0	0	1
T	1	-1	0	0

The following solution is obtained:

$$\begin{array}{l} L \quad c = 2; \\ M \quad n = 0; \\ T \quad a = 1; \quad b = 1; \end{array}$$

which is unacceptable for GDAM, given that the n exponent is null, (0).

The conclusion is that the newly introduced parameter, the initial concentration of raw material,  $c_{in}$ , is not important for the solid-liquid extraction.

The introduction of **kinematical viscosity,  $v$** , leads to the following dimensional matrix of variables:

$$\begin{array}{r} // \tau^a, D_{1,2}^b, \quad d^c, v^e, // \\ L \quad 0 \quad 2 \quad 1 \quad 2 \\ M \quad 0 \quad 0 \quad 0 \quad 0 \\ T \quad 1 \quad -1 \quad 0 \quad -1 \end{array}$$

The non determinate system of variables exponents leads to six solutions:

$$\begin{array}{l} * \quad c = 1; \quad b = 1; \quad e = 1/2; \\ ** \quad c = 1; \quad e = 1; \quad b = 3/2; \\ *** \quad b = 1; \quad e = 1; \quad c = 0; \\ **** \quad a = 1, \quad b = 1; \quad e = 0; \\ ***** \quad a = 1; \quad e = 1; \quad b = 2; \\ ***** \quad b = 1; \quad e = 1; \quad a = 0. \end{array}$$

Only \*\*\*\*\* solution is acceptable under GDAT rules. The result shows that the momentum diffusivity is not important for the solid-liquid extraction. The introduction into matrix line of **solvent density,  $\rho$** :

$$\begin{array}{r} // \tau^a, D_{1,2}^b, \rho^f, \quad d^c, // \\ L \quad 0 \quad 2 \quad -3 \quad 1 \\ M \quad 0 \quad 0 \quad 1 \quad 0 \\ T \quad 1 \quad -1 \quad 0 \quad 0. \end{array}$$

The indeterminate system of variables exponents leads to a solution unacceptable for GDAT:  $f = 0$ . Result: density of solvent is not an important parameter for solid-liquid extraction.

The introduction into matrix line of a **dynamic viscosity,  $\eta$** :

$$\begin{array}{r} // \tau^a, D_{1,2}^b, \quad d^c, \eta^h, // \\ L \quad 0 \quad 2 \quad 1 \quad -1 \\ M \quad 0 \quad 0 \quad 0 \quad 1 \\ T \quad 1 \quad -1 \quad 0 \quad -1. \end{array}$$

The indeterminate system of variables exponents leads to a solution unacceptable for GDAT:  $f = 0$ . Result: dynamic viscosity of solvent is not an important parameter for solid-liquid extraction.

The introduction into matrix line **simultaneously of a dynamic viscosity,  $\eta$** , and a **solvent density,  $\rho$** :

$$\begin{array}{rcccl}
 // \tau^a, & D_{1,2}^b, & \rho^f, & & d^c, \eta^h, // \\
 L & 0 & 2 & -3 & 1 & -1 \\
 M & 0 & 0 & 1 & 0 & 1 \\
 T & 1 & -1 & 0 & 0 & -1
 \end{array}$$

leads to one accepted solution:

$$\begin{array}{l}
 L \quad c = 2; \\
 M \quad f = 1; \quad h = 1; \\
 T \quad a = 1; \quad b = 2.
 \end{array}$$

The monomial type relation is:

$$\tau = k_2 \cdot \frac{d^2 \cdot \eta}{D_{1,2}^2 \cdot \rho}, \quad (8),$$

which can be re-written as:

$$\frac{\tau \cdot D_{1,2}}{d^2} = k_2 \cdot \frac{\eta}{D_{1,2} \cdot \rho}, \text{ or: } Fo_D = k_2 \cdot Sc, \quad (9).$$

The solution obtained through GDAM shows the following facts:

- the density and dynamic viscosity do have an impact on the solid-liquid extraction process, but only together. They have an opposite influence upon the process.

- a high density of a solvent is beneficial for the extraction. The justification of this fact is the influence of density in the case of Supercritical Fluid Extraction, (SCFE).

- lower viscosity favours both the molecular transport mechanism and increases the diffusion coefficient. SCFE works as a good example in this case as well.

If into matrix line of variables the parameter **speed (linear velocity), w**, is introduced, then:

$$\begin{array}{rcccl}
 // \tau^a, & D_{1,2}^b, & w^j, & & d^c, // \\
 L & 0 & 2 & 1 & 1 \\
 M & 0 & 0 & 0 & 0 \\
 T & 1 & -1 & -1 & 0,
 \end{array}$$

which leads to the accepted solution:

$$\begin{array}{l}
 L \quad b = 1; \quad j = 1; \quad c = 3; \\
 T \quad a = 2.
 \end{array}$$

The monomial type relation is:

$$\tau^2 = k_4 \cdot \frac{d^3}{D_{1,2} \cdot w}. \quad (10),$$

which can be written as:

$$\frac{\tau \cdot D_{1,2}}{d^2} \cdot \frac{\tau}{d} \cdot \frac{w}{1} = \frac{\tau \cdot D_{1,2}}{d^2} \cdot \frac{1}{\frac{d}{\tau}} \cdot \frac{w}{1} = \frac{\tau \cdot D_{1,2}}{d^2} \cdot \frac{w}{w'} = k_4,$$

or: 
$$Fo_D \cdot Ho = k_4, \tag{11}.$$

The result indicates two conclusions. Firstly, the newly introduced parameter, linear velocity,  $w$ , is an important one for the solid-liquid extraction. Secondly, a new non dimensional rapport appears, Homocronie (Strouhal), where the expected speed of the process is divided by the general speed of the process and characterizes non steady state processes.

The introduction into the matrix line of simultaneously **solvent density,  $\rho$ , dynamic viscosity,  $\eta$**  and **linear velocity,  $w$** , results in:

$$\begin{matrix} // \tau^a, & D_{1,2}^b, & \rho^f, & w^j, & d^c, & \eta^h, & // \\ L & 0 & 2 & -3 & 1 & 1 & -1 \\ M & 0 & 0 & 1 & 0 & 0 & 1 \\ T & 1 & -1 & 0 & -1 & 0 & -1, \end{matrix}$$

respectively the solution:

$$\begin{matrix} L & c = 1. \\ M & f = 1; h = 1; \\ T & a = 1; b = 1; j = 1. \end{matrix}$$

Monomial type relation is: 
$$\tau = k_3 \cdot \frac{d \cdot \eta}{D_{1,2} \cdot \rho \cdot w}, \tag{12},$$

Which can be written as:

$$\frac{\tau \cdot D_{1,2}}{d^2} = k_3 \cdot \frac{\eta}{w \cdot \rho \cdot d}, \text{ or: } Fo_D = k_3 \cdot Re^{-1}, \text{ or: } Fo_D \cdot Re = k_3, \tag{13}.$$

The appearance of linear velocity at dominator translates into a reverse influence to the Reynolds number, indicating that turbulence itself is less important for the process, but also that the increase of turbulence is important for the entire assembly of the process within the fluid media.

This aspect is very important to demonstrate that the principal step of the process is molecular diffusion, but that, as part of the overall process, increasing of the velocity of the fluid increases the speed of global velocity mass transfer.

For the entire generalization of momentum, heat and mass transfer of properties, an observation can be made that simultaneously with an increase in the velocity of the fluid all the coefficients for the transfer of properties increase as well.

The product between  $Fo_D \cdot Re$  becomes constant, this fact represents the reduced the time of process, but only trough convection, not for the molecular mechanism.

If the parameter **Earth gravity, g**, is introduced into the equation, the following equation is obtained:

$$\begin{array}{cccccc} // & \tau^a, & D_{1,2}^b, & g^j, & & d^c, // \\ L & 0 & 2 & 1 & & 1 \\ M & 0 & 0 & 0 & & 0 \\ T & 1 & -1 & -2 & & 0 \end{array}$$

and leads to the accepted solution:

$$\begin{array}{l} L \quad b = 1; \quad j = 1; \quad c = 3; \\ T \quad a = 3. \end{array}$$

The monomial type relation: 
$$\tau^3 = k_5 \cdot \frac{d^3}{D_{1,2} \cdot g}, \quad (14),$$

is homogenous dimensionally,  $[s^3] = [s^3]$ , and can be written:

$$\frac{\tau \cdot D_{1,2}}{d^2} = k_6 \cdot \frac{d}{\tau} \cdot \frac{1}{\tau \cdot g} = k_6 \cdot \frac{w}{\tau \cdot g} = k_6 \cdot \frac{w}{\tau \cdot g} \cdot \frac{d}{\tau} \cdot \frac{1}{d} = k_6 \cdot \frac{w^2}{g \cdot d},$$

or: 
$$Fo_D = k_6 \cdot Fr, \quad Fo_D \cdot Fr^{-1} = k_6, \quad (15).$$

There are several conclusions that can be drawn from the above relations. Firstly, the new introduced parameter, Earth gravity, g, is an important one for the solid-liquid extraction. Secondly, the new non-dimensional rapport, Froude, appears, which describes the expected influence of action of external forces (gravity, centrifugal, magnetically, electrically, ultrasonic, microwave, etc.) upon the system. Thirdly, the possibility of solid-liquid extraction to be influenced by natural convection or of different external forces is highlighted. The overriding conclusion is that an increase of the external forces coupled with a decrease in the time of the process results in the intensification of the transport and transfer phenomena.

The introduction into the matrix line simultaneously of **dynamic viscosity, η, solvent density, ρ, and earth gravity, g**, results in:

$$\begin{array}{cccccc} // & \tau^a, & D_{1,2}^b, & \rho^f, & g^j, & & d^c, \eta^h, // \\ L & 0 & 2 & -3 & 1 & & 1 & -1 \\ M & 0 & 0 & 1 & 0 & & 0 & 1 \\ T & 1 & -1 & 0 & -2 & & 0 & -1. \end{array}$$

The non determinate system of variable exponents leads to these three possible solutions:

- \* a = 1; b = 1; j = 1/2;
- \*\* a = 1; b = 0; j = 1;
- \*\*\* a = 0; b = 1; j = 1.

All of these results are not accepted under GDAM. This fact shows that external forces influence only convection and not the molecular mechanism and the rate determinant step of the operation is internal diffusion or molecular transport into the boundary layer. External forces are therefore secondary parameters for solid - liquid extraction.

The introduction into the matrix line simultaneously of **solvent density,  $\rho$ , dynamic viscosity,  $\eta$ , linear velocity,  $w$  and earth gravity,  $g$** , results in:

$$\begin{array}{ccccccc} // \tau^a, & D_{1,2}^b, & \rho^f, & g^h, & w^m, & d^c, & \eta^e, // \\ L & 0 & 2 & -3 & 1 & 1 & 1 & -1 \\ M & 0 & 0 & 1 & 0 & 0 & 0 & 1 \\ T & 1 & -1 & 0 & -2 & -1 & 0 & -1 \end{array}$$

The non determinate system of variables exponents leads to these solutions:

- M f = 1; e = 1;
- T a - b - 2 h - m = -1, with possible options:
- \* a = 1; b = 1; m = 1; h = 0; non accepted;
- \*\* a = 1; b = 1; h = 1; m = -1; non accepted;
- \*\*\* a = 1; b = -1; h = 1; m = 1; non accepted;
- \*\*\*\* a = 3; b = 1; h = 1; m = 1; accepted;
- L 2 b - 3 f + h + m = c - e, c = 2.

Only one of the above four solutions is accepted in accordance with GDAT, indicating that the new variable, Earth gravity,  $g$ , is of secondary importance to the solid-liquid extraction process.

The monomial type relation is:  $\tau^3 = k_7 \cdot \frac{d^2 \cdot \eta}{D_{1,2} \cdot g \cdot w \cdot \rho}$ , (16),

is homogenous dimensionally,  $[s^3] = [s^3]$ , and can be expressed:

$$\frac{\tau \cdot D_{1,2}}{d^2} = k_7 \cdot \frac{\eta}{w \cdot \rho \cdot d} \cdot \frac{d}{\tau} \cdot \frac{d}{\tau \cdot g \cdot d} = k_7 \cdot \frac{\eta}{w \cdot \rho \cdot d} \cdot \frac{w^2}{g \cdot d},$$

or:  $Fo_D = k_7 \cdot Re^{-1} \cdot Fr$ ,  $Fo_D \cdot Re \cdot Fr^{-1} = k_6$ , (17).

The appearance of  $Fr$  criteria at reverse power indicates clearly the secondary importance of Earth's gravity.

The introduction into the matrix line of **dispersed power,  $P$** ,

$$\begin{array}{r} // \tau^a, D_{1,2}^b, P^n, d^c, // \\ L \quad 0 \quad 2 \quad 2 \quad 1 \\ M \quad 0 \quad 0 \quad 1 \quad 0 \\ T \quad 1 \quad -1 \quad -3 \quad 0. \end{array}$$

The indeterminate system of variables exponents leads to this solution:

$$\begin{array}{l} L \quad b = 1; \quad c = 2; \\ M \quad n = 0; \\ T \quad a = 3, \end{array}$$

a solution that is not accepted under GDAT. The result of calculus leads to the conclusion that the newly introduced variable, dispersed power, is of secondary importance or not important for solid-liquid extraction.

By formation a new matrix line, including the **dissipated power, P, the density, ρ, and the dynamic viscosity, η**:

$$\begin{array}{r} // \tau^a, D_{1,2}^b, \rho^f, P^n, d^c, \eta^e, // \\ L \quad 0 \quad 2 \quad -3 \quad 2 \quad 1 \quad -1 \\ M \quad 0 \quad 0 \quad 1 \quad 1 \quad 0 \quad 1 \\ T \quad 1 \quad -1 \quad 0 \quad -3 \quad 0 \quad -1, \end{array}$$

the generated solutions are:

$$\begin{array}{l} M \quad f = 1; \quad n = 1; \quad e = 2; \\ T \quad * \quad a = 1; \quad b = 1; \quad e = 2/3; \\ \quad \quad ** \quad a = 1; \quad b = 0; \quad n = 1; \\ \quad \quad *** \quad a = 2; \quad b = 1; \quad n = 1; \\ L \quad \quad \quad c = 3. \end{array}$$

A single solution is accepted under GDAM, a fact which shows that the newly introduced variable, dissipated power, P, has less importance for the process.

The monomial type relation, generate from this accepted solution is:

$$\tau^2 = k_4 \cdot \frac{d^3 \cdot \eta^2}{D_{1,2} \cdot \rho \cdot P}, \quad (18),$$

and after rearrangement becomes:

$$\left( \frac{\tau \cdot D_{1,2}}{d^2} \right)^2 = k_4 \cdot \frac{\eta}{w \cdot d \cdot \rho} \cdot \frac{w \cdot D_{1,2} \cdot \eta}{P},$$

or:

$$Fo_D^2 = k_4 \operatorname{Re}^{-1} \cdot K_{ND}^{-1}, \quad Fo_D^2 \cdot \operatorname{Re} \cdot K_{ND} = k_4, \quad (19).$$

We must remark upon the appearance of a new non dimensional group of similitude, analogous with the Power criteria for mixing. The presence of a Reynolds and Power criteria at reverse power indicates the lower importance of dispersed power and of linear velocity of fluid media.

It is possible to analyze trough the same method the influence of the interfacial tension upon solid-liquid extraction. The minimum matrix line become:

$$\begin{array}{r} // \tau^a, D_{1,2}^b, d^c, \sigma^o // \\ L \quad 0 \quad 2 \quad 1 \quad 0 \\ M \quad 0 \quad 0 \quad 0 \quad 1 \\ T \quad 1 \quad -1 \quad 0 \quad -2, \end{array}$$

which doesn't have an accepted solution for GDAM:

$$\begin{array}{l} L \quad c = 2; \\ M \quad 0 = o; \\ T \quad a = 1; \quad b = 1. \end{array}$$

The result of calculus leads to the conclusion that the newly introduced variable, interfacial tension, is of less importance or non important for the solid-liquid extraction.

By formation of a a new matrix line, including **the interfacial tension,  $\sigma$ , the density,  $\rho$ , and the dynamic viscosity,  $\eta$** :

$$\begin{array}{r} // \tau^a, D_{1,2}^b, \rho^f, d^c, \eta^e, \sigma^o // \\ L \quad 0 \quad 2 \quad -3 \quad 1 \quad -1 \quad 0 \\ M \quad 0 \quad 0 \quad 1 \quad 0 \quad 1 \quad 1 \\ T \quad 1 \quad -1 \quad 0 \quad 0 \quad -1 \quad -2 \end{array}$$

The generated solutions are:

$$\begin{array}{l} L \quad c = 3; \\ M \quad f = 2; \quad e = 1; \quad o = 1; \\ T \quad * \quad a = 1; \quad b = 4; \\ \quad \quad ** \quad a = -2; \quad b = 1. \end{array}$$

A single solution is accepted from GDAM, a fact which shows that the newly introduced variable, interfacial tension,  $\sigma$ , has less importance for the process, (one solution accepted of two), but there is an increased influence of dissipated power, (one accepted solution of three), linear velocity, (one accepted solution of four) and earth gravity, (no accepted solution).

The monomial type relation, generated from this accepted solution is:

$$\tau = k_8 \cdot \frac{d^3 \cdot \eta \cdot \sigma}{D^4 \cdot \rho^2}, \quad (20),$$

and after rearrangement becomes:

$$\frac{\tau \cdot D_{1,2}}{d^2} = k_8 \cdot \frac{\eta}{D_{1,2} \cdot \rho} \cdot \frac{\sigma}{w^2 \cdot \rho \cdot d} \cdot \frac{d^2 \cdot w^2}{D_{1,2}^2},$$

or:

$$Fo_D = k_8 \cdot Sc \cdot We^{-1} \cdot Pe_D^2, \quad Fo_D = k_8 \cdot Sc^3 \cdot Re^2 \cdot We^{-1}, \quad (21).$$

The appearance of the Weber criteria at reverse power shows the secondary importance of interfacial tension.

By introduction of **all variables** which were presented initially, the matrix line becomes:

//	$\tau^a$ ,	$D_{1,2}^b$ ,	$\rho^e$ ,	$P^i$ ,	$g^j$ ,	$w^o$ ,	$d^c$ ,	$\eta^j$ ,	$\sigma^o$ ,	//
L	0	2	-3	2	1	1	1	-1	0	
M	0	0	1	1	0	0	0	1	1	
T	1	-1	0	-3	-2	-1	0	-1	-2	

and has the solution accepted from GDAT:

L	$b = 1;$	$j = 1;$	$o = 1;$	$c = 4;$
M	$e = 1;$	$i = 1;$	$f = 1;$	$h = 1;$
T	$a = 4.$			

This solution leads to the monomial type relation:

$$\tau^4 = k_9 \cdot \frac{d^4 \cdot \eta \cdot \sigma}{D \cdot \rho \cdot P \cdot g \cdot w}, \quad (22),$$

which can be written:

$$\frac{\tau \cdot D}{d^2} = k_9 \cdot \frac{D \cdot \rho}{\eta} \cdot \frac{\eta}{w \cdot d \cdot \rho} \cdot \frac{\sigma}{w^2 \cdot \rho \cdot d} \cdot \frac{w^2}{d \cdot g} \cdot \frac{w \cdot D \cdot \eta}{P},$$

or:

$$Fo_D = k_9 \cdot Sc \cdot Re^{-1} \cdot Fr \cdot We^{-1} \cdot K_{ND}, \quad (23).$$

The same influence of the parameters, and the formation of a criteria equation similar to the general expression, (1) is then observed.

## CONCLUSIONS

GDAM method can offer the possibility to study a phenomenon from both an experimental and theoretically point of view, starting with the parameters that most likely can influence it.

The fundamental parameters for the process were highlighted during the formation of the minimum matrix line. These fundamental parameters then uncovered internal diffusion as the principal stage of the process.

GDAM can discriminate between the principal, secondary and non-important variables. These variables are selected based on a hierarchy resulting from the number of GDAM - not accepted solutions. For this purpose, interfacial tension,  $\sigma$ , has lower importance in the process, (one solution accepted of two), but there is a higher influence from the dissipated power, (one accepted solution of three), linear velocity, (one accepted solution of four) and Earth's gravity, (no accepted solution). This hierarchy concludes that convection is a secondary mechanism for mass transport.

GDAM can generate a new criteria of similitude, for example: Power criteria at non steady-state mass diffusion into solid-liquid extraction,

$K_{ND} = \frac{w \cdot D_{1,2} \cdot \eta}{P}$ , and shows a direct relation for non steady-state operation

with time of the process via the Homocronie, (Strouhal), criteria.

The GDAM shows that the initial concentration of raw material is not an important parameter.

By introduction of all parameters the complete criteria expression is obtained, similar to relation (10).

The GDAM facilitates the experimental study of a process by making it necessary to determine a single parameter, the numerical constant k. This value is the proof for correctness of the relation.

## REFERENCES

1. Literat L.; *Transfer Phenomena*, (in Romanian), Ed. UBB, Cluj-Napoca, **1985**, p. 51 - 54.
2. Bratu E.A.; *Unit Operations in Chemical Engineering*, (in Romanian), Ed. Tehnica, Bucuresti, **1985**.
3. Staicu C.I.; *General Dimensional Analysis*, (in Romanian), Ed. Tehnica, Bucuresti, **1975**.
4. Coulson J.M., Richardson J.F., Buckhurst J.R., Harker J.H.; *Chemical Engineering*; vol I, 6<sup>th</sup>, Ed., Pergamon Press, Oxford, New-York, Toronto, Sidney, Paris, Frankfurt, **1996**.
5. Wankat P.C.; *Separations in Chemical Engineering*, Ed. Elsevier, New-York, Amsterdam, **1988**.
6. Vasilescu Al. A.; *Dimensional analysis and similitude theory*, (in Romanian), Ed. Academiei RSR, Bucuresti, **1969**.
7. Misca B.R.H.; *Solid-liquid extraction*, PhD. thesis, Cluj-Napoca, **1998**.
8. Manciuila D.I.; *The study of isolation and synthesis of a one phytochemical products whit pharmacological importance*, PhD thesis, Cluj-Napoca, **2013**.